ANTIFERROMAGNETIC SPINOR CONDENSATES IN MICROWAVE DRESSING FIELDS AND OPTICAL LATTICES

By

LICHAO ZHAO

Bachelor of Science in Physics
University of Science and Technology of China
Hefei, Anhui, China
2006

Submitted to the Faculty of the
Graduate College of the
Oklahoma State University
in partial fulfillment of
the requirements for
the Degree of
DOCTOR OF PHILOSOPHY
December, 2015

ANTIFERROMAGNETIC SPINOR CONDENSATES
IN MICROWAVE DRESSING FIELDS
AND OPTICAL LATTICES

Dissertation Approved:

Dr. Yingmei Liu
Dissertation Adviser

Dr. John Mintmire

Dr. Gil Summy

Dr. Weili Zhang

ACKNOWLEDGEMENTS

First and foremost, I would like to thank my advisor, Dr. Yingmei Liu. Dr. Liu motivated me through the process of becoming a Ph.D. of Physics. It has been great to work under her supervision. She led me to find my strength while complementing my weakness so that I can become a better researcher. From classrooms to research sites, from academic studies to conferences networks, she was always available for discussions and prioritizes the needs of students, which I am highly appreciative of.

I would like to express my gratitude to my committee members, who have given me great help during my research process. Dr. John Mintmire and Dr. Gil Summy have been helping me not only in classrooms, but also in atomic physics research. Their thoughtful questions and comments improved my understanding of underlying physics, and their support can never be forgotten. Dr. Weili Zhang also provided a unique point of view on my study, which I am thankful for.

I also would like to thank Dr. Xincheng Xie for his support at the beginning of my OSU studies. Throughout my doctoral studies, I also benefited a lot from learning and discussions with other professors, both inside and outside classrooms. Specifically, I would like to thank Dr. Girish Agarwal, Dr. Kaladi Babu, Dr. Mario Borunda, Dr. Eduardo Yukihara and Dr. Donghua Zhou. In addition, I also would like to thank Dr. Robert Hauenstein and Dr. Albert Rosenberger for guiding me through the general rules of the Ph.D. program.

I am also grateful to Jie Jiang for his great contribution of both our experimental system constructing and our experimental data taking. I also would like to thank all the current group members Tao Tang, Zihe Chen, Micah Webb, all the former group members Jackson Stubblefield, Jared Austin, Zongkai Tian, Alex Behlen, and all the visiting students Liyuan Qiu, Haoxiang Yang, Nan Jiang and Yunfei Pu for their contributions to our group. I am also thankful to Shengtao Wang for some useful theoretic discussions.

Lastly, I would like to thank my family, who supported me the past seven years. Their love accompanied me all the way through this special time of my life.

Name: LICHAO ZHAO

Date of Degree: DECEMBER, 2015

Title of Study: ANTIFERROMAGNETIC SPINOR CONDENSATES IN
MICROWAVE DRESSING FIELDS AND OPTICAL LATTICES

Magor Field: PHYSICS

Abstract: In this thesis, I present the design and construction of several experimental parts, e.g., a spin-flip Zeeman slower, a fast feedback circuit, and some magnetic field driving circuits. An efficient method of optimizing the slower with our simulation program is explained. I also demonstrate how the efficiency of a slower strongly depends on a few of its intrinsic parameters, such as the intensity of the slowing laser beam and the length of each section in the slower. These findings lead to a simple three-step procedure of designing an optimal Zeeman slower for neutral atoms, especially for those atomic species with high initial velocities, for example lithium atoms.

In addition, we experimentally study spin dynamics of a sodium antiferromagnetic spinor condensate as a result of spin-dependent interactions c and microwave dressing field interactions characterized by the net quadratic Zeeman effect q_{net}. In contrast to magnetic fields, microwave dressing fields enable us to access both negative and positive values of q_{net}. We find an experimental signature to determine the sign of q_{net}, and observe harmonic spin population oscillations at every q_{net} except near each separatrix in phase space where spin oscillation period diverges. No spin domains and spatial modes are observed in our system. Our data in the negative q_{net} region exactly resembles what is predicted to occur in a ferromagnetic spinor condensate in the positive q_{net} region. This observation agrees with an important prediction derived from the mean-field theory: spin dynamics in spin-1 condensates substantially depends on the sign of q_{net}/c. This work may be the first to use only one atomic species to reveal mean-field spin dynamics, especially the remarkably different relationship between each separatrix and the magnetization, of spin-1 antiferromagnetic and ferromagnetic spinor condensates.

Furthermore, we experimentally demonstrate that spin dynamics and the phase diagram of spinor condensates can be conveniently tuned by a two-dimensional optical lattice. Spin population oscillations and a lattice-tuned separatrix in phase space are observed in every lattice where a substantial superfluid fraction exists. In a sufficiently deep lattice, we observe a phase transition from a longitudinal polar phase to a broken-axisymmetry phase in steady states of lattice-confined spinor condensates. The steady states are found to depend sigmoidally on the lattice depth and exponentially on the magnetic field. we also introduce a phenomenological model that semi-quantitatively describes our data without adjustable parameters.

In addition, I will discuss immediate applications of spinor BECs in quantum information science.

TABLE OF CONTENTS

List of Figures

List of Tables

CHAPTER I

INTRODUCTION

1.1 Bose-Einstein condensate

Atomic Bose-Einstein condensates (BECs) are gases which are so cold that all the atoms have a single collective wavefunction for their spatial degrees of freedom (Einstein, 1925). The first theoretical model of a BEC state was introduced by Satyendra Nath Bose and Albert Einstein in 1925 when they discussed the quantum statistics of photons. They extended the similar idea to matters and proposed that identical bosonic particles or atoms would fall into their lowest energy quantum state and form a new state of matter. In other words, when the atom temperature is below a critical temperature, atoms may undergo a phase transition from a thermal gas to a BEC, in which large fraction of bosons occupy the lowest energy state. However, it took almost seven decades for the scientific community to overcome numerous experimental challenges associated with bringing atoms to an ultracold temperature. In 1995, a Colorado group led by Eric Cornell and Carl Wieman and another group led by Wolfgang Ketterle at MIT successfully produced scalar BECs with neutral alkali metal atoms (Anderson *et al.*, 1995; Davis *et al.*, 1995; Bradley *et al.*, 1995). This experimental breakthrough was awarded a Nobel prize in physics six years later, because it provides a revolutionary method to observe microscopic quantum phenomena in a macroscopic scale.

In the last twenty years, BECs have been realized in many different atomic species including alkali metal atoms and alkali earth atoms, e.g., ^{87}Rb (Anderson *et al.*, 1995), ^{23}Na (Davis *et al.*, 1995), ^{7}Li (Bradley *et al.*, 1995), ^{1}H (Fried *et al.*, 1998), ^{85}Rb (Cornish *et al.*, 2000), ^{41}K (Modugno *et al.*, 2001), ^{133}Cs (Weber *et al.*, 2003), ^{174}Yb (Takasu *et al.*, 2003), ^{52}Cr (Griesmaier *et al.*, 2005), ^{39}K (Roati *et al.*, 2007), ^{170}Yb (Fukuhara *et al.*, 2007), ^{40}Ca (Kraft *et al.*, 2009), ^{84}Sr (Stellmer *et al.*, 2009; de Escobar *et al.*, 2009), ^{86}Sr (Stellmer *et al.*, 2010), ^{164}Dy (Lu *et al.*, 2011), and ^{168}Er (Aikawa *et al.*, 2012). Multi-component BECs have also been achieved and studied (Modugno *et al.*, 2002; Thalhammer *et al.*, 2008; Lercher *et al.*, 2011; McCarron *et al.*, 2011). Different methods were invented to bring atoms to an ultra-cold temperature of tens of nanoKelvin. Several widely used techniques are laser cooling, polarization gradient cooling, sympathetic cooling, and evaporative cooling in either an optical dipole trap or magnetic traps (Jiang *et al.*, 2013). BEC research has grown rapidly with BEC systems being applied to a wide range of research areas, such as condensed matter physics, quantum state engineering, atomic collision physics, and precision measurements.

1.2 Spinor Bose-Einstein condensates

The first BEC was realized and trapped in a magnetic field (Anderson *et al.*, 1995; Davis *et al.*, 1995; Bradley *et al.*, 1995) with the spin of the atoms being aligned along the local magnetic field. This kind of BECs are called scalar BECs, in which the spin degree of freedom of the atoms is frozen. An important improvement was made in 1998 by Wolfgang Ketterle's group at MIT via confining cold atoms in an optical dipole trap (ODT) (Stamper-Kurn *et al.*, 1998). ODTs can form almost identical trapping potentials for all spin states, so the spin degree of freedom of atoms is released. This new trapping method has opened a door for investigating interesting properties of spinor condensates, which have multiple spin components and possess a vector order parameter.

Compared to scalar BECs, the key benefit of spinor BECs is thus the additional spin degree of freedom. Together with Feshbach resonances and optical lattices which tune the interatomic interactions, spinor BECs constitute a fascinating collective quantum system offering an unprecedented degree of control over such parameters as spin, temperature, and the dimensionality of the system (Stamper-Kurn and Ueda, 2013; Kawaguchi and Ueda, 2012). Spinor BECs in optical lattices have been considered as a highly controllable playground for studying many-body physics, simulating mesoscopic magnetism, and generating massive entanglement and spin-squeezing.

Numerous theoretical and experimental studies have been carried out in spinor condensates of both ^{87}Rb (Matthews *et al.*, 1998; Hall *et al.*, 1998a,b) and ^{23}Na (Stenger *et al.*, 1998; Ho, 1998; Ohmi and Machida, 1998) atoms. F=1 spinor BECs have been applied to study antiferromagnetic interactions with ^{23}Na atoms and ferromagnetic interactions with ^{87}Rb atoms. Due to the interplay of the spin-dependent interaction and the quadratic Zeeman energy, coherent interconversions (among two $|F=1, m_F=0\rangle$ atoms, one $|F=1, m_F=+1\rangle$ atom, and one $|F=1, m_F=-1\rangle$ atom) lead to spin mixing dynamics or spin population oscillations. These spin population oscillations are harmonic except near a separatrix in phase space where the oscillation period diverges. The separatrix sets a boundary between the interaction-dominated region and the Zeeman-energy-dominated region (Stamper-Kurn and Ueda, 2013; Zhao *et al.*, 2014b). These were observed experimentally in both ^{23}Na (Liu *et al.*, 2009b,a; Black *et al.*, 2007; Jiang *et al.*, 2013) and ^{87}Rb (Chang *et al.*, 2005a; Kuwamoto *et al.*, 2004; Kronjäger *et al.*, 2006; Schmaljohann *et al.*, 2004) spinor BEC systems. Quantum phase transitions have also been observed in the ground states of $F=1$ spinor condensates of both ^{23}Na (Stenger *et al.*, 1998; Miesner *et al.*, 1999; Bookjans *et al.*, 2011; Jacob *et al.*, 2012; Jiang *et al.*, 2014) and ^{87}Rb (Chang *et al.*, 2005b; Guzman *et al.*, 2011) atoms. Theoretical predictions of ground-states of spinor condensates have also been made (Zhang *et al.*, 2003). Other interesting phenomena observed in spinor BECs include spin textures which shows spatial variations in the spin of atoms, spontaneous symmetry breaking, topological excitations and defects as a consequence of the symmetry breaking (Sadler *et al.*, 2006; Choi *et al.*, 2012; Leslie *et al.*, 2009a; yoon Choi *et al.*, 2012).

It is worth noting that spinor BECs provide opportunities to entangle a large collection of atoms at once, e.g., spin-squeezing more than 10^3 atoms have been realized (Hamley *et al.*, 2012; Gerving *et al.*, 2012; Riedel *et al.*, 2010; Gross *et al.*, 2011; Chen *et al.*, 2011; Takano *et al.*, 2009). In contrast, only a few particles have been entangled using ion trapping (Meyer *et al.*, 2001; Monz *et al.*, 2011). A coherent spin-state is an unentangled state with all spins aligned in the same direction, while the spin degrees of freedom of atoms become entangled in spin-squeezed states. Spin-squeezing has attracted much attention for its potential to enhance the performance of quantum computation, the security of quantum communication, and the precision of quantum measurements. Another advantage of our Na system is the negligible two-body losses which may lead to larger spin-squeezing than that in the Rb system. Theoretical work also shows that it is possible to manipulate the phase-space topology and dynamics of the Na system in ways not possible in the Rb system. While the Rb system is becoming well studied in a number of research groups, the Na system remains less explored and only a handful of groups worldwide are even capable of performing experimental studies on it.

1.3 Optical lattices

Naturally, in crystals, electrons move within periodical potentials formed by atom arrays. A pair of counter-propagating laser beams can also form a periodical potential, which may simulate potentials in crystals. This artificial lattice is called an optical lattice. The optical lattice is a versatile technique to enhance interatomic interactions and control the mobility of atoms (Markus Greiner and Bloch, 2002; Jaksch *et al.*, 1998; Fisher *et al.*, 1989). Atoms held in shallow lattices can tunnel freely among lattice sites and form a superfluid (SF) phase. The tunneling rate is suppressed while the on-site atom-atom interaction increases in deeper lattices. This may result in a transition from a SF phase to a Mott-insulator (MI) phase at a critical lattice depth, which has been confirmed in various scalar BEC systems (Markus Greiner and Bloch, 2002; Jaksch *et al.*, 1998; Fisher *et al.*, 1989; Xu *et al.*, 2006).

In contrast to scalar BECs, spinor BECs have unique advantages due to an additional spin degree of freedom. For example, because of the existence of the spin dependent interactions, the predicted SF-MI phase transition points should be shifted in lattice-trapped antiferromagnetic spinor BECs, and the order of some SF-MI transitions may also change. One of the important predictions is that the SF-MI transition may be first or second order around the tip of each Mott lobe for an even or odd occupation number, respectively (Stamper-Kurn and Ueda, 2013; Batrouni *et al.*, 2009). In addition, richer spin dynamics are predicted in lattice-trapped ferromagnetic ^{87}Rb spinor BECs (Becker *et al.*, 2010; Widera *et al.*, 2005; Pedersen *et al.*, 2014; Widera *et al.*, 2006) and antiferromagnetic ^{23}Na spinor BECs (Zhao *et al.*, 2015). Spinor BECs in optical lattices thus allow us to systematically study, verify, and optimize condensed matter models (Stamper-Kurn and Ueda, 2013; Kawaguchi and Ueda, 2012; Mahmud and Tiesinga, 2013). These may lead to many immediate applications, such as constructing a novel quantum-phase-revival spectroscopy driven by a competition between spin-dependent interaction and spin-independent interaction, understanding quantum magnetism system and mesoscopic magnetism, and realizing massive entanglement (Stamper-Kurn and Ueda, 2013; Mahmud and Tiesinga, 2013).

1.4 Outline

When I joined our group in the fall of 2011, we just finished the construction of a sodium Magneto-Optical Trap (MOT). My early time in our lab was working on optimizing our MOT and realizing our first BEC. I was in charge of the design and construction of the spin-flip Zeeman slower, fast feedback circuits, and some other circuits.

In Chapter II of this thesis, I will first briefly describe our spinor BEC apparatus and the BEC production procedures. Then I will give a detailed explanation on a project led by me, the design and optimization of the Zeeman slower and its control circuits.

Chapter III will discuss the spin dynamics of spinor BECs. I'll start from the Hamiltonian of spinor BECs in Section 3.1. Sections 3.2 to 3.4 will discuss the magnetic field induced Zeeman energy, the microwave dressing field induced Zeeman energy, spin-dependent interaction energy, and spin independent interaction energy, respectively. Section 3.5 will review the single spatial mode approximation (SMA) and solve the Hamiltonian by using this approximation. The spin dynamics and ground states predicted by SMA will also be discussed in this section. Our experimental setup and procedures will be discussed in Sections 3.6 and 3.7, respectively. Our recent experimental studies on the spin-mixing dynamics of a F=1 sodium spinor condensate tuned by a microwave dressing field will be discussed in the last section of this chapter.

Chapter IV will discuss spinor condensates in a two-dimensional optical lattice. It will start from the basic theory of the optical lattice potential in Section 4.1. The band structure will be discussed under an approximation, by ignoring interatomic interactions in Section 4.2. We will review the Bose-Hubbard model in Section 4.3. Section 4.4 will explain our experimental procedures for constructing our 2d optical lattices and how to adiabatically load spinor condensate into the optical lattice. In the last two sections, our experimental results on spin-mixing dynamics and steady states of lattice-confined antiferromagnetic spinor BECs will be discussed, respectively.

In the last chapter, Chapter V, I will discuss immediate applications of spinor BECs in quantum information science. For example, implement the first ultra-precise magnetometer of micron spatial resolution and femto-tesla field sensitivity with spin-squeezed sodium BECs. Precise magnetometers have made it possible to image vortex dynamics in two-dimensional superconducting films, map geomagnetic anomalies, and sense the magnetic field of the brain. Our idea is to apply the proven optical measurement methods of atomic magnetometry (Liu *et al.*, 2009b; Budker and Romalis, 2007), but replace the hot atomic vapor at 500 Kelvin with ultracold BECs at 100 nanoKelvin. Thermal diffusions that limit the sensitivity of hot-vapor magnetometers are frozen out at BEC temperatures. Spin noise in conventional magnetometers will be suppressed by spin-squeezing. This would improve the field sensitivity of the spinor-BEC-based magnetometer beyond the shot-noise limit. This spinor-BEC-based magnetometer would also be upgraded to a precise magnetic scanning microscope via spatially scanning optical traps.

Some parts of this thesis have been published. Chapter II is based on Refs. (Zhao *et al.*, 2014a) and (Jiang *et al.*, 2013). Chapter III is based on Refs. (Zhao *et al.*, 2014b) and (Jiang *et al.*, 2014). Chapter IV is based on Ref. (Zhao *et al.*, 2015). Reprints of these published papers are included in the appendixes.

CHAPTER II

CONSTRUCT AND OPTIMIZE THE BEC APPARATUS

This chapter describes our sodium spinor BEC apparatus, and our procedures to construct and optimize our spin-flip Zeeman slower and its fast servo circuits. Two papers related to these topics were published:

- L. Zhao, J. Jiang, Y. Liu, *Optimizing a spin-flip Zeeman slower*, arXiv:1401.7181. Included in Appendix A.
- J. Jiang, L. Zhao, M. Webb, N. Jiang, H. Yang, and Y. Liu, *Simple and efficient all-optical production of spinor condensates*, Phys. Rev. A **88**, 033620 (2013). Included in Appendix E.

Our experimental sodium BEC apparatus consists of numerous optical, vacuum, magnetic, and electronic parts. It took nine undergraduate and graduate students three years to construct the entire apparatus. I was in charge of several parts: a spin-flip Zeeman slower, a fast feedback circuit with which even a cheap power supply can be applied to rapidly and simply control various magnetic coils in a BEC apparatus. In addition, I also designed and constructed control circuits for varies magnetic field coils and some signal buffer circuits. In this chapter, I will present the design and construction of these parts. An efficient method of optimizing the slower with our simulation program and by monitoring the number of atoms trapped in a magneto-optical trap (MOT) is also explained. In addition, I will demonstrate how the efficiency of a slower strongly depends on a few of its intrinsic parameters, such as the intensity of the slowing laser beam and the length of each section in the slower. These findings lead to a simple three-step procedure of designing an optimal Zeeman slower for neutral atoms, especially for those atomic species with high initial velocities, for example lithium atoms.

Before I introduce these constructions and optimizations, in the first section of this chapter, I'll give an overview of our sodium BEC system.

2.1 Our sodium spinor BEC apparatus

The vacuum apparatus of our sodium spinor BEC system is divided into three vacuum chambers, i.e., an atomic oven chamber, an intermediate chamber, and a main chamber, as shown in Fig. 2.1. A differential pumping tube and a gate valve is placed between each two adjoined chambers. This two-step differential pumping bring us a $\sim 10^{-12}$ torr ultra-high vacuum, which leads long BEC life time and high stability due to low background collisions or less heating. Another advantage of this three-chamber design is that it allows us refill sodium metals and get the vacuum pressures back to the $\sim 10^{-12}$ torr range within 24 hours.

Our Zeeman slower is located between the intermediate chamber and the main chamber. Hot atoms from the sodium oven are slowed down by the slower and then enter the main

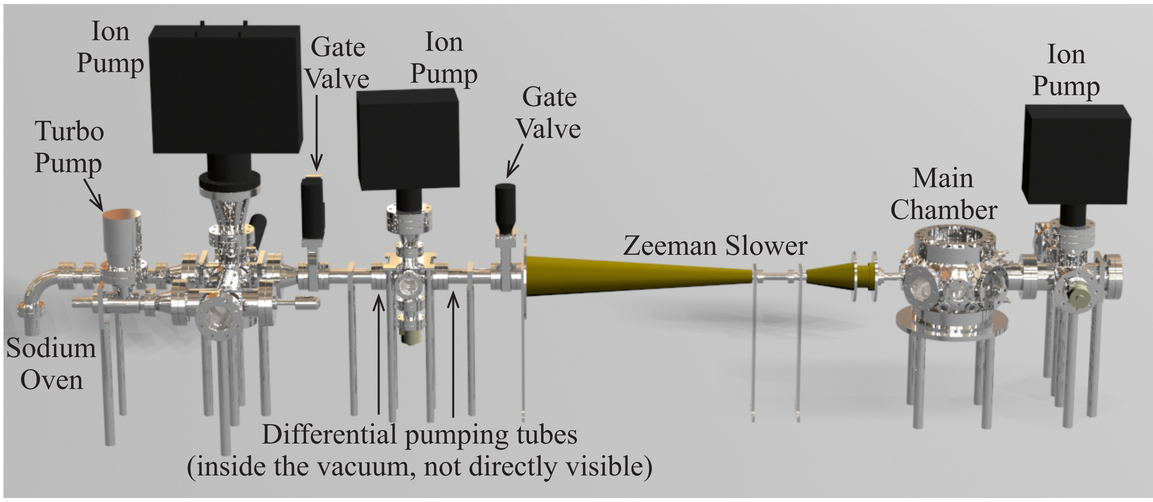

Figure 2.1: Schematic of our sodium spinor BEC apparatus.

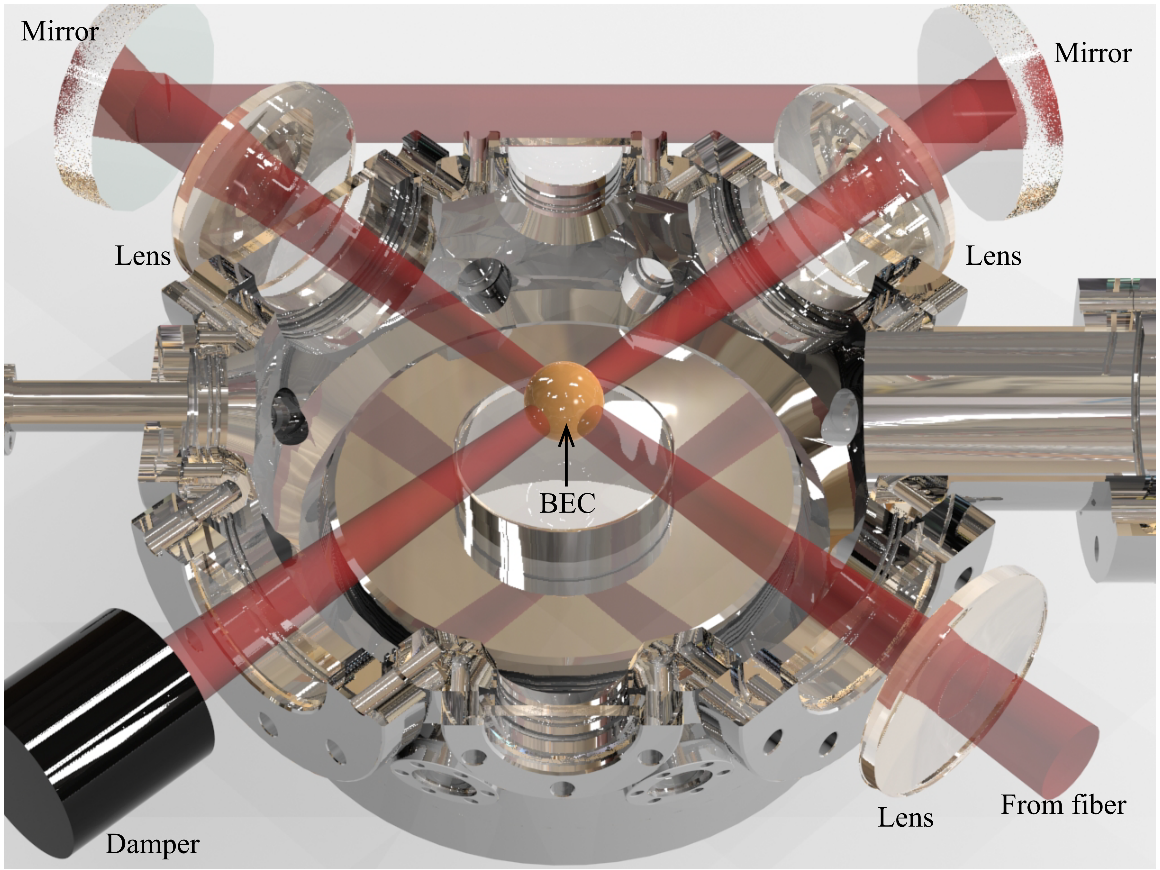

Figure 2.2: Schematic of the crossed ODT setup around the main chamber.

chamber. The design of our Zeeman slower will be introduced in the next section. The slowed atoms are then be captured by a magneto-optical trap (MOT) located in the main chamber. The MOT is constructed with six cooling beams and a pair of 24-turn water chilled anti-Helmholtz coils. Each MOT cooling beam is detuned by $\delta_{\text{cooling}} = -20$ MHz from the cycling transition, has a power of 6 mW, and combines with one 3.5 mW MOT repumping beam in a single-mode fiber. Every MOT repumping beam is detuned by $\delta_{\text{repump}} = -5$ MHz from the $|\text{F} = 1\rangle$ to $|\text{F}' = 2\rangle$ transition. The MOT's maximum capture velocity v_{c} is thus ~ 50 m/s. After 8.5 s of MOT loading, we use polarization gradient cooling process to cool 3×10^8 atoms to 40 μK efficiently. The atoms are then depump to $F = 1$ hyperfine states by extinguish repumping beams shortly before cooling beams.

The final cooling from MOT to BEC is using an all optical design in our system. During the MOT loading and polarization gradient cooling processes, a crossed optical dipole trap

(ODT) is kept at a moderate power. This power is chosen to balance two competing ODT-induced effects (Jiang *et al.*, 2013). First, high ODT power improves MOT to ODT transfer efficiency if the ODT beams do not interact with the MOT. However, non-negligible ac Stark shifts due to the ODT beams impair the MOT cooling capability. For the detail analyses of this scheme, please refer to Ref. (Jiang *et al.*, 2013). The ODT is constructed by two far-detuned linear polarized high-power inferred beams at 1064 nm. Our two ODT beams are near orthogonal in the horizontal plane as shown in Fig. 2.2. The beam waists at their intersection point is 33 μm. The ODT beams are delivered through a single-mode polarization-maintaining fiber to polish the beam mode and minimize pointing fluctuations. This design brings a long lifetime of 8 s and a large collision rate after atoms are transferred from the MOT into the tightly focused crossed ODT. These are essential for all-optical BEC approaches.

After an optimized 6 s forced evaporative cooling process, a pure F=1 BEC of 1.0×10^5 sodium atoms is created. The spin healing length and the Thomas-Fermi radii of a typical condensate studied in this thesis are 13 μm and (6.1, 6.1, 4.3) μm, respectively. Atoms in the F=1 BEC can be fully polarized to the $|F = 1, m_F = -1\rangle$ state by applying a weak magnetic field gradient during the first half of the forced evaporation. By this method, a BEC purified in $|F = 1, m_F = -1\rangle$ state is prepared. Procedures for each experiment after this preparation stage will be respectively introduced in the related chapter.

2.2 An optimized spin-flip Zeeman slower

Laser cooling and trapping neutral atoms with a magneto-optical trap (MOT) has become an important step in a successful production of ultracold quantum gases (Metcalf and van der Straten, 1999). To improve the capture efficiency of a MOT, a number of slowers were invented to slow hot atoms before they overlap with the MOT (Ketterle *et al.*, 1993; Metcalf and van der Straten, 1999; Durfee, 1999; Phillips and Metcalf, 1982; Naik, 2006; Gibble *et al.*, 1992). Atoms and a resonant laser beam counter propagate in a slower. The longitudinal velocity and corresponding Doppler shift of these atoms decrease after

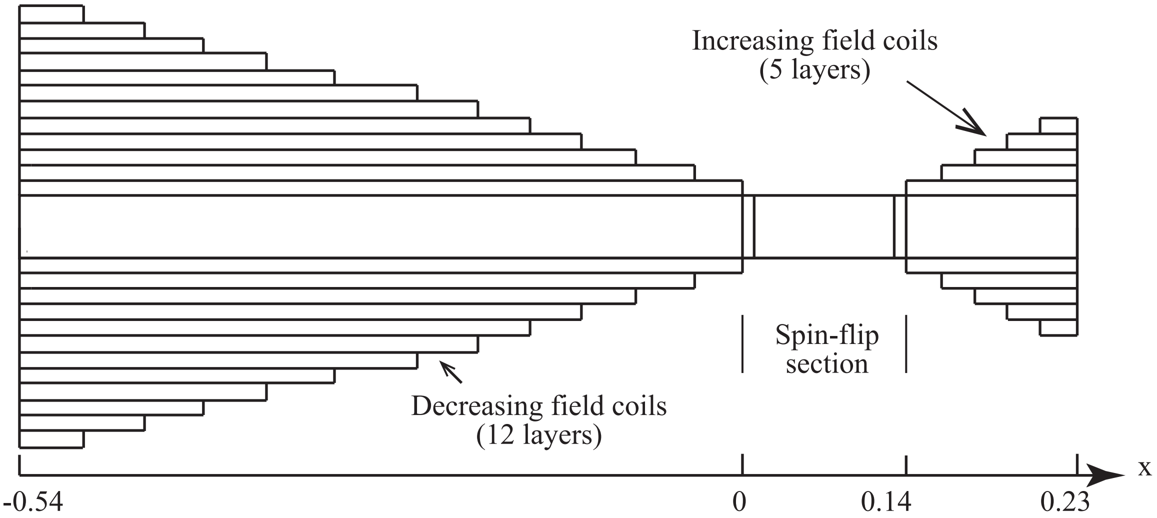

Figure 2.3: Schematic of our spin-flip Zeeman slower. The first layer of the decreasing field coils has 188 turns and its length is 0.54 m. The second layer is 0.51 m long and wrapped on the surface of the first layer. Similarly, the following layers are wrapped on the surface of its corresponding previous layer. The increasing field section has five layers and is constructed in a similar way. All axes are not to scale.

they absorb resonant photons. After a few such absorptions, these slowed atoms are no longer resonant with the laser beam and thus cannot be further slowed down. In order to continuously slow atoms along the laser beam path, one can vary the laser frequency accordingly as with the frequency chirp method (Wallis and Ertmer, 1988) or by using broadband lasers (Zhu *et al.*, 1991). Another widely-used method is to compensate differences in the Doppler shift with a spatially varying magnetic field generated by a Zeeman slower while keeping the laser frequency unchanged (Metcalf and van der Straten, 1999; Durfee, 1999; Phillips and Metcalf, 1982; Marti *et al.*, 2010; Cheiney *et al.*, 2011; Bell *et al.*, 2010; Naik, 2006; Dedman *et al.*, 2004; Lison *et al.*, 1999). Our BEC system is using the Zeeman slower design.

2.2.1 The design of our spin-flip Zeeman slower

Our multi-layer slower has three different sections along the x axis (i.e., a decreasing field section, a spin-flip section, and an increasing field section), as shown in Fig. 2.3. Compared with the single-layer Zeeman slower with variable pitch coils (Bell *et al.*, 2010), this multi-layer design provides us enormous flexibilities in creating large enough magnetic field strength B for slowing atoms with high initial velocities (e.g., sodium and lithium atoms). The first section of our Zeeman slower produces a magnetic field with decreasing magnetic field strength B. We choose $B \sim 650$ Gauss at the entrance of the slower, so the slowing beam only needs to be red-detuned by δ of a few hundred MHz from the D2 line of ^{23}Na atoms. This frequency detuning is easily achieved with an acousto-optic modulator, but is still large enough to avoid perturbing the MOT. The spin-flip section is simply a bellow to maintain $B = 0$ for atoms to be fully re-polarized and also to damp out mechanical vibrations generated by vacuum pumps. The increasing field section creates a magnetic field with increasing B but in the opposite direction to that of the decreasing field section, which ensures the magnetic field quickly dies off outside the slower. This slower can thus be placed close to the MOT, which results in more atoms being captured.

Our multi-layer spin-flip Zeeman slower surrounds a stainless steel tube that measures 22.5 mm inner diameter and 25.5 mm outer diameter, which is similar to the design of Ref. (Naik, 2006). The first layer of our decreasing field coil has 188 turns, and the second layer is wrapped on the surface of the first layer. Similarly, the following layers are wrapped on the surface of its corresponding previous layer. The increasing field coil is constructed in a similar way with five layers. To precisely adjust magnetic field strength inside the slower, all layers are divided into four groups, and different layers in each group are connected in series and controlled by one DC power supply with our fast feedback circuit. The fast feedback circuit will be discussed in Section 2.3.

2.2.2 Optimizing a spin-flip Zeeman slower

When neutral atoms pass through the Zeeman slower, only those atoms with a longitudinal velocity $v(x) = -[2\pi\delta + \mu B(x)/\hbar]/k$ are resonant with the slowing beam and can be slowed. Here μ is the magnetic moment, $\hbar$ is the reduced Planck's constant, k and δ are the wavevector and frequency detuning of the laser beam, respectively. The actual deceleration

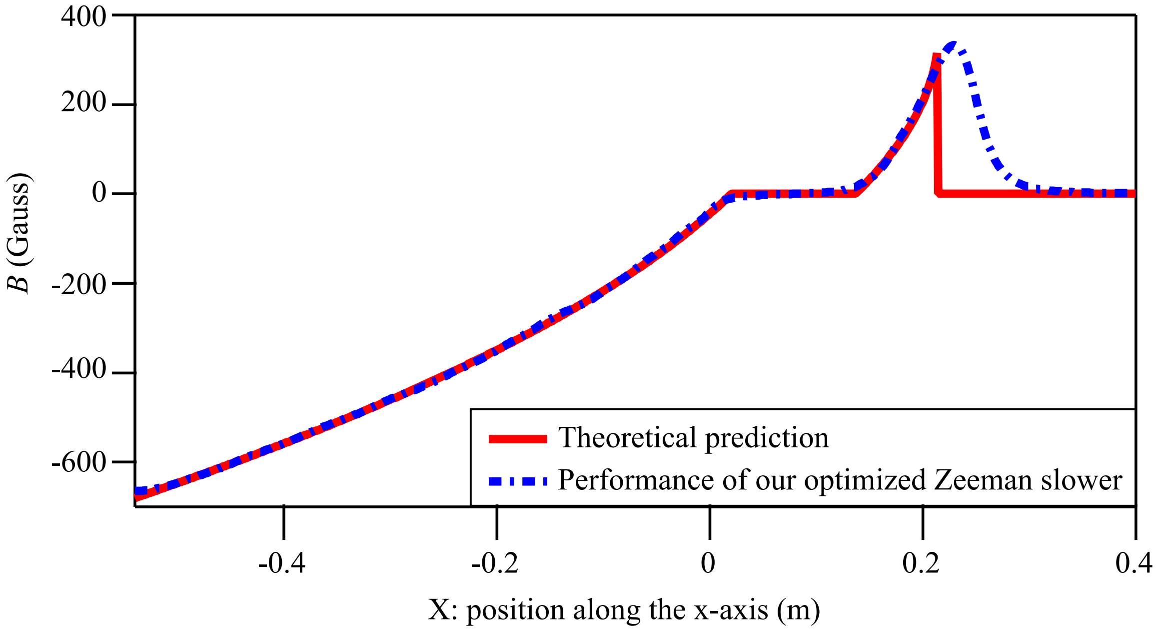

Figure 2.4: A comparison between a theoretical prediction (solid red line) and the performance of our optimized Zeeman slower (dash-dotted blue line), with $\delta = -512$ MHz and η in decreasing and increasing sections being set at 0.65. Atoms propagate along the positive x-axis direction. The MOT center locates at 0.45 m, where residual magnetic fields created by the slower are negligible.

$a_s = \eta a_{\max}$ in the slower is thus given by

$$\begin{aligned} \frac{dB(x)}{dx} &= -a_s \frac{\hbar k}{\mu v} \\ &= \eta a_{\max} \frac{\hbar k^2}{\mu[2\pi\delta + \mu B(x)/\hbar]} \ , \end{aligned} \tag{2.1}$$

where η is a safe factor to account for magnetic field imperfections in a given slower and the finite intensity of the slowing laser beam, and $a_{\max} = \hbar k \Gamma / 2M$ is the maximal achievable deceleration. M and Γ are the mass and the natural linewidth of the atoms, respectively.

Our largest MOT is achieved when we match $B(x)$ inside the slower as precisely as possible to a prediction derived from Eq. 2.1 with η being set at 0.65 in decreasing- and increasing-field sections and $v_f = 40$ m/s, as shown in Fig. 2.4. Here v_f is the velocity of atoms at the end of the slower. N, the number of atoms in a MOT, can also be boosted by a larger atomic flux with a hotter atomic oven. However, this is generally not a favorable method due to two reasons. First, a hotter oven generates atoms with higher initial average velocities, but a slower can only handle entering atoms of a certain maximum velocity. Second, alkali metals' consumption rates sharply increase with the oven temperature.

We find that convenient parameters to adjust are slowing beam's intensity I and frequency detuning δ, electric current i in each magnetic coil, and the length of each section of the slower. These parameters, however, cannot be optimized independently since there is a strong correlation among them. In order to efficiently optimize the slower, we developed a computer program to simulate $B(x)$ and compared the simulation results to the actual magnetic field strengths in the slower under many different conditions (e.g., at various values of i). The actual magnetic field strengths were measured with a precise Hall probe before the slower was connected to the vacuum apparatus. The agreements between the simulation results and the measurements are good, i.e., the discrepancies are < 5 %. This simulation program can thus mimic the actual performance of a Zeeman slower and provide a reasonable tuning range for each aforementioned parameter, which allows for efficiently optimizing the slower.

One common way to evaluate a slower's performance is from knowing the exact number of atoms whose velocities are smaller than v_c with a costly resonant laser. In the next four subsections, we show that a convenient detection method of optimizing a slower is to monitor the number of atoms captured in the MOT, i.e., more atoms trapped in a given MOT setup indicate a better performance of the slower.

Intensity of the slowing beam

Figure 2.5 shows that the MOT capture efficiency strongly depends on the slowing beam power P, i.e., N increases with P and then stays at its peak value N_max when P is higher than a critical value. This can be understood from the relationship between the safe factor η of a slower and the slowing beam intensity I. Based on Ref. (Lison *et al.*, 1999), the safe

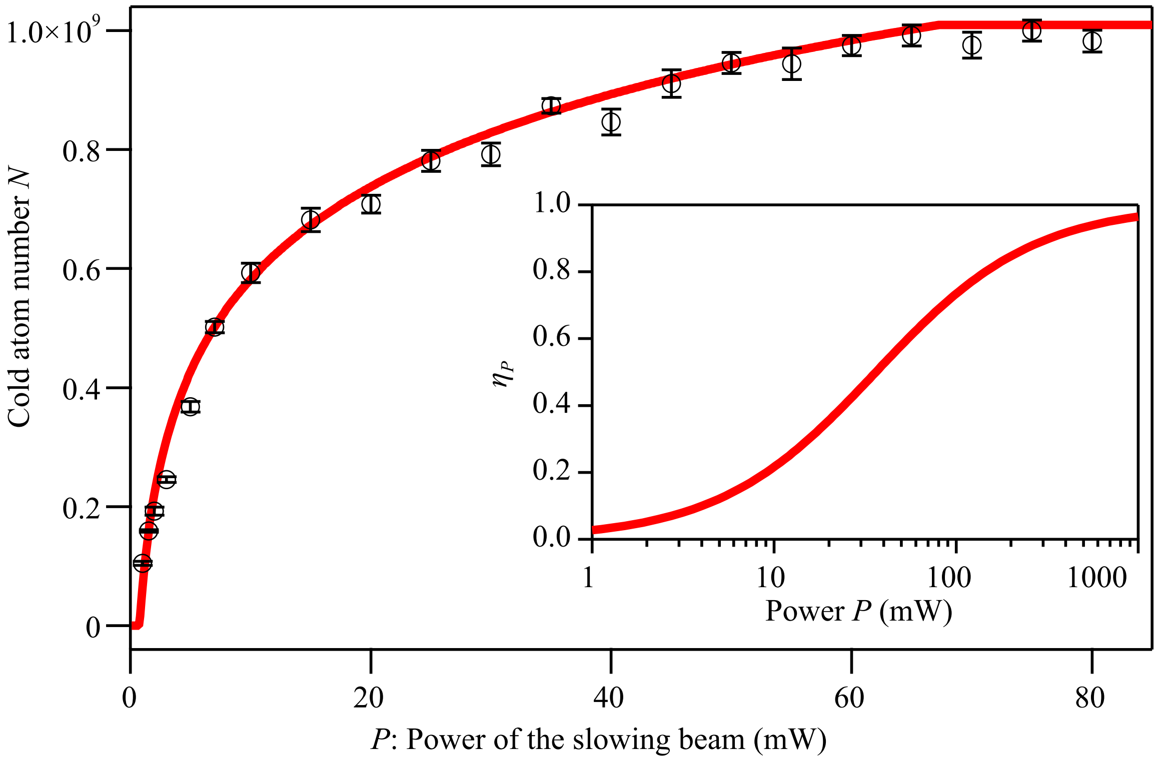

Figure 2.5: N as a function of the slowing beam power P with 1 mW corresponding to $I_0/I_s = 2.5$. Thesolid line is a fit based on Eq. 2.3 with η in decreasing- and increasing-field sections being set at 0.65. Inset: η_p as a function of P for our apparatus.

factor η_{laser} at a finite I can be expressed as,

$$\begin{aligned}\eta_{\text{laser}} &= \frac{I/I_s}{1 + I/I_s + [\frac{2\pi\delta + \mu B/\hbar + kv}{\Gamma/2}]^2} \\ &\leq \eta_{\text{laser}}^{\max} = \frac{I/I_s}{1 + I/I_s} \ , \end{aligned} \tag{2.2}$$

where I_s is the saturation intensity of neutral atoms, e.g., it is 6.26 mW/cm^2 for sodium atoms. Eq. 2.2 implies that the safe factor of any optimal Zeeman slower has an upper limit, $\eta_{\text{laser}}^{\max}$, as long as the slowing beam intensity is fixed. In other words, a bigger η in the decreasing- or increasing-field section does not always lead to a more efficient Zeeman slower if I is given.

For a Gaussian slowing beam with a width W, its intensity I can be expressed as $I(r) = I_0 \cdot e^{-\frac{2r^2}{W^2}}$. Here r is the distance away from the slowing beam center and $I_0 = 2P/(\pi W^2)$

is the beam intensity at $r = 0$. N can be given by,

$$\begin{aligned} N(P) &= \frac{N_{\max}}{\pi R_0^2}\int_0^{R_0} H\left[\eta_{\text{laser}}^{\max}(r) - \eta\right] 2\pi r dr \\ &= \frac{N_{\max}}{R_0^2/2}\int_0^{R_0} H\left[\frac{P\cdot\exp(-\frac{2r^2}{W^2})}{\frac{\pi}{2}W^2 I_s + P\cdot\exp(-\frac{2r^2}{W^2})} - \eta\right] r dr \ . \end{aligned} \tag{2.3}$$

Here $H[r]$ is a unit step function of r to account for the fact that atoms can be efficiently slowed only when $\eta \leq \eta_{\text{laser}}^{\max}(r)$, and R_0 is the radius of the atomic beam. Figure 2.5 shows that our data taken with $\eta = 0.65$ in decreasing- and increasing-field sections can be well fitted by Eq. 2.3 and N saturates at $P \geq 70$ mW. This indicates that 70 mW is the minimum power to achieve $\eta = 0.65$ for our apparatus. We can thus define a η_p, the preferred η in decreasing- and increasing-field sections at a given P, and derive its expression from Eq. 2.3 as follows,

$$\eta_p = P\cdot\exp(-\frac{2R_0^2}{W^2})/[\frac{\pi}{2}W^2 I_s + P\cdot\exp(-\frac{2R_0^2}{W^2})] \ . \tag{2.4}$$

The predicted η_p as a function of P for our apparatus is shown in the inset in Fig. 2.5, which implies P sharply increases with η_p and is infinitely large at $\eta_p = 1$. Therefore, the first step in designing an optimal Zeeman slower is to determine η_p from Eq. 2.4 based on the available slowing beam power.

The decreasing field section

To focus on the decreasing-field section, our data shown in this subsection are taken with η being set at 0.65 in the increasing-field section, a fixed distance between the atomic oven and the MOT center to maintain a fixed solid angle for an atomic beam, $\delta = -512$ MHz, and $P = 70$ mW which implies η_p is 0.65. Based on the discussions in Refs. (Durfee, 1999; Marti *et al.*, 2010), N can be expressed as

$$N = \int_0^{v_{\max}} N_0(v) f(v) dv \ , \tag{2.5}$$

where $N_0(v) \propto v^3 e^{-\frac{mv^2}{k_B T}}$ is the initial number of atoms created by the oven, k_B is the Boltzmann constant, and the oven temperature T is set at 530 K in this work. $f(v)$ is a correction factor to account for the transverse velocity distribution of slowed atoms after they absorb resonant photons in a Zeeman slower, which can be expressed as

$$f(v) = 1 - \exp\left[-\frac{r_{\mathrm{mot}}^2}{(v_r v/3)L^2/v_f^2}\right] . \tag{2.6}$$

Here r_{mot} is the radius of a MOT, L is the distance between the MOT center and the end of a Zeeman slower, v_r is the recoil velocity of an atom in a slowing process, and $\sqrt{v_r v/3}$ is the transverse velocity of slowed atoms (Marti *et al.*, 2010). In Eq. 2.5, v_{max} is the maximum velocity of entering atoms which can be handled by a slower. For a spin-flip Zeeman slower, v_{max} is given by

$$v_{\mathrm{max}} = \sqrt{v_{\mathrm{sf}}^2 + 2\eta_d \cdot a_{\mathrm{max}} \cdot L_d} \ , \tag{2.7}$$

where L_d and η_d are the length and the actual safe factor of the decreasing-field section, respectively. And $v_{\mathrm{sf}} = 2\pi\delta/k$ is the velocity of atoms which are resonant with the slowing beam at the spin-flip section, since B is zero in this section. For example, v_{sf} is 302 m/s at $\delta = -512$ MHz in our sodium BEC apparatus.

For a given δ, Eqs. 2.5-2.7 predict that N should monotonically increase with v_{max}, i.e., N increases with η_d at a fixed L_d (or N increases with L_d at a fixed η_d). However, our observations shown in Fig. 2.6(a) are drastically different from this prediction: at each L_d studied in this report, N appears to first increase with η_d, reach its peak N_{max} at a critical value of η_d, and then decrease with η_d. Based on Eq. 2.7, we can also plot these data points as a function of v_{max}, as shown in Fig. 2.6(b). At each value of L_d, the agreement between our data and a theoretical prediction derived from Eqs. 2.5-2.7 (dotted black line) can only be found when v_{max} is smaller than 800 m/s, which is approximately equal to the mean velocity ($\sqrt{9\pi k_B T/8m}$) of atoms entering our slower.

In addition, we plot $\Delta N/\Delta L_d$ as a function of η_d in Fig. 2.7, where $\Delta N/\Delta L_d$ represents the number of extra atoms in the MOT gained from elongating the decreasing-field section

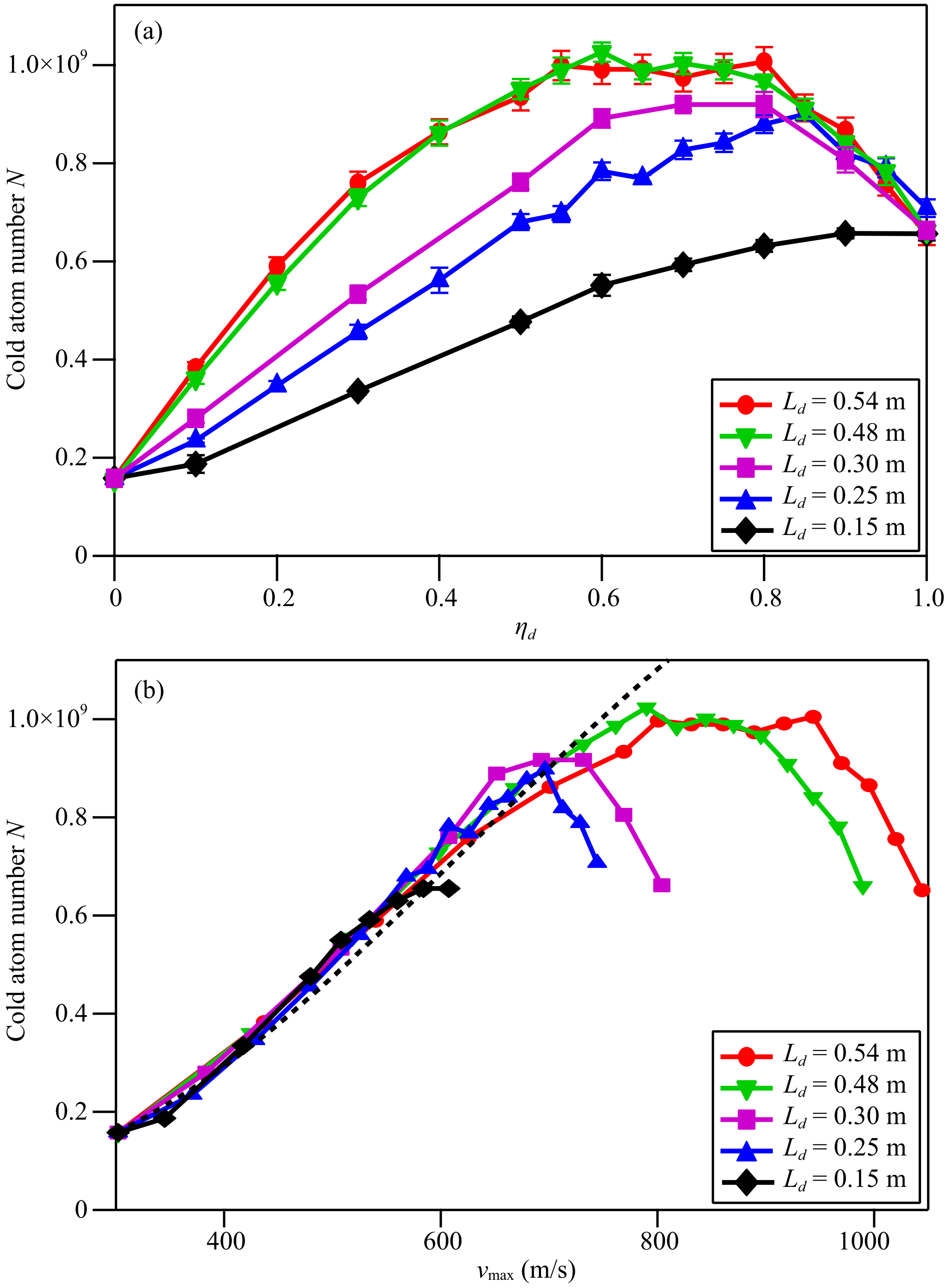

Figure 2.6: N as a function of η_d (a) and $v_{\max}$ (b) with η being set at 0.65 in the increasing-field section, $\delta = -512$ MHz, and $P = 70$ mW. Dotted black line in Panel (b) is a fit based on Eqs. 2.5-2.7.

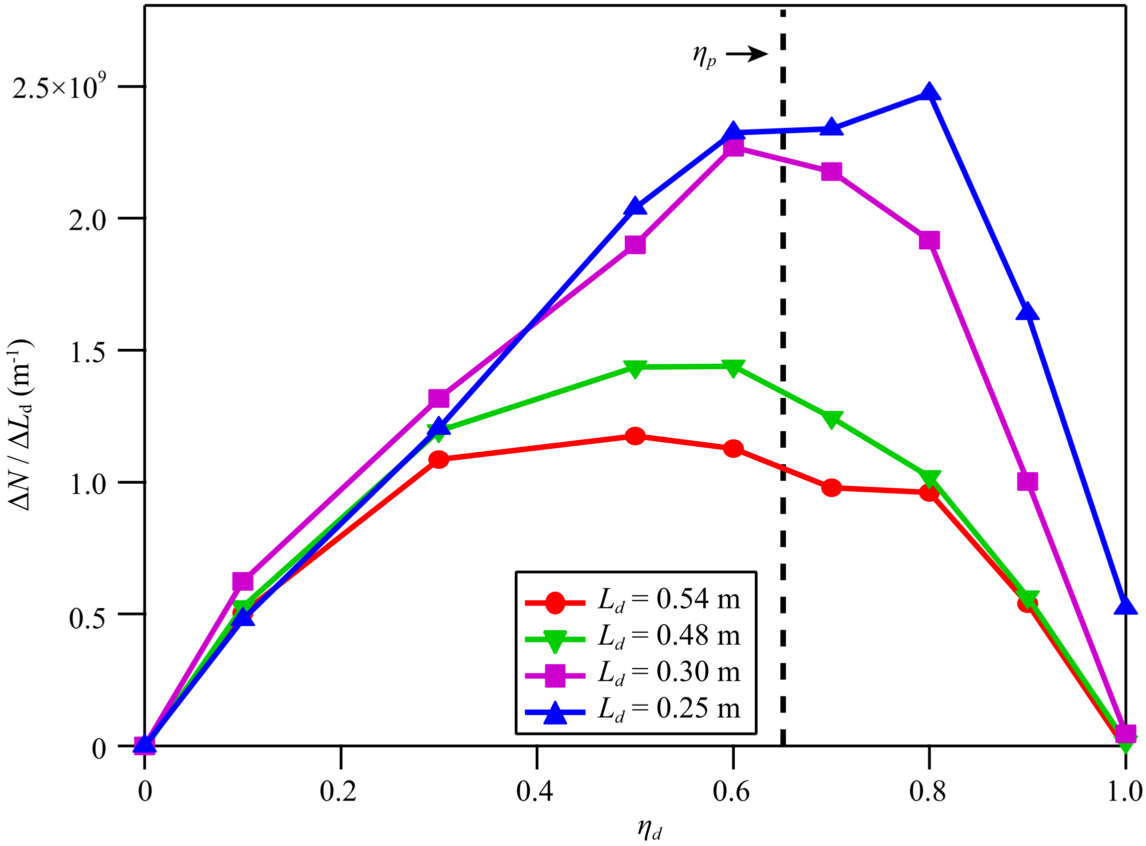

Figure 2.7: $\Delta N/\Delta L_d$ as a function of η_d. Here $\Delta L_d = L_d - 0.15$ m, and ΔN is the number of extra atoms being slowed when L_d is set at a value longer than 0.15 m. Black dashed line marks the position of η_p, which is determined by the slowing laser beam power.

by $\Delta L_d = L_d - 0.15$ m. Figure 2.7 shows that $\Delta N/\Delta L_d$ drops to a much smaller value when L_d is increased from 0.3 m to 0.48 m. This implies the ideal length of the decreasing-field section for our apparatus should be longer than 0.3 m and shorter than 0.48 m. It is worth noting that $\Delta N/\Delta L_d$ peaks at $\eta_d \sim 0.65$ for each value of L_d, as shown in Fig. 2.7. Interestingly, the predicted η_p from Eq. 2.4 is also 0.65 at $P = 70$ mW, and Fig. 2.6(a) shows $\eta_d \sim 0.65$ is also the position where the largest N occurs. This indicates that η of our optimized decreasing-field section is actually equal to η_p. Therefore, one important procedure in designing an optimal Zeeman slower is as follows:

1. find out η_p based on Eq. 2.4 from the available slowing beam intensity;

2. determine the length of the decreasing-field section from Eq. 2.7, i.e., $L_d = [9\pi k_B T/8m - (2\pi\delta/k)^2]/(2\eta_p a_{\max})$;

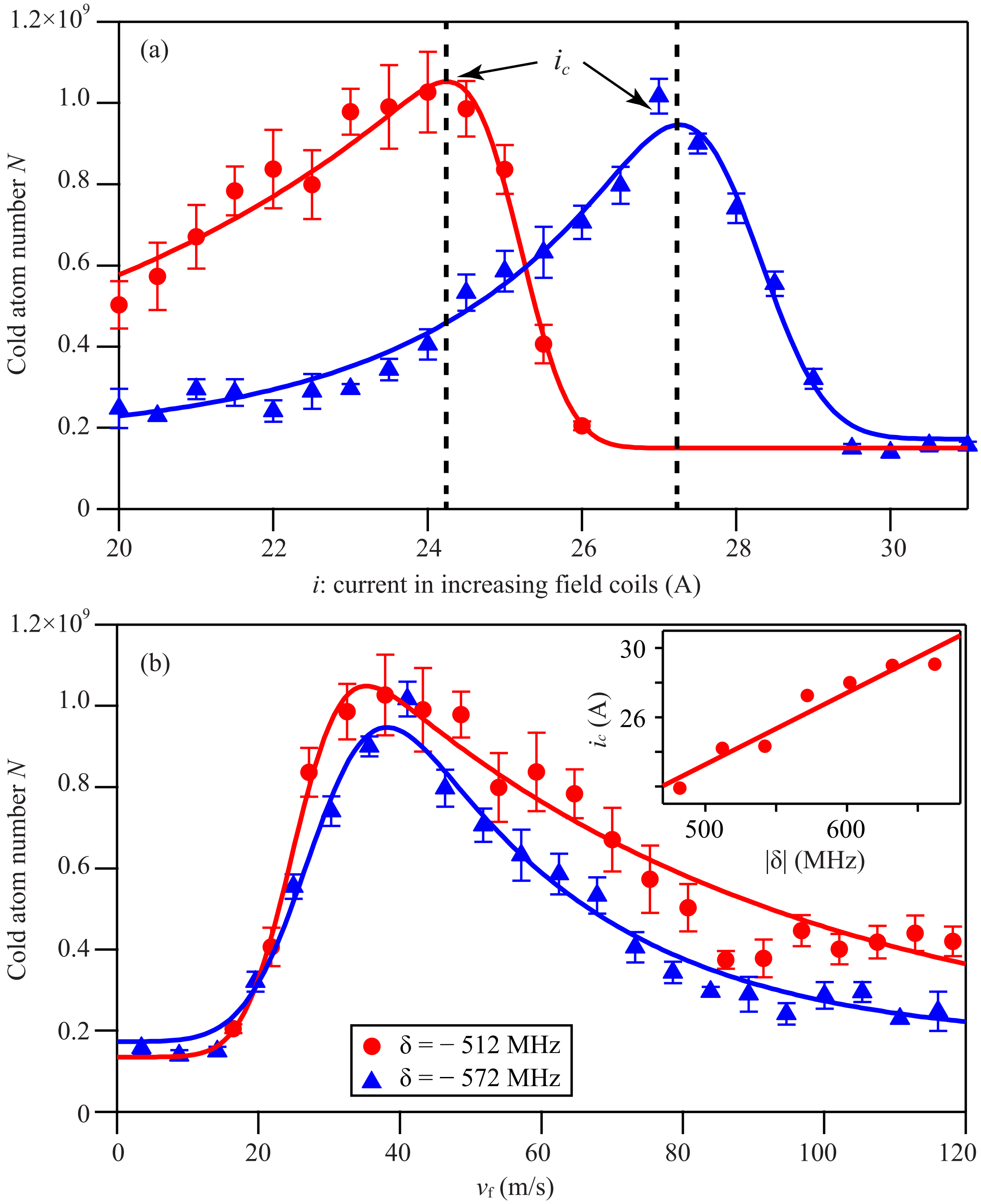

Figure 2.8: N as a function of i (a) and v_f (b) at $\delta = -512$ MHz (red circles) and $\delta = -572$ MHz (blue triangles). i_c at a given δ is defined as the electric current at which N peaks. Solid lines are fits to guide the eye. Inset: i_c extracted from Panel(a) as a function of $|\delta|$. The solid line is a linear fit.

3. find out electric currents i of decreasing-field coils with our simulation program by precisely matching the simulated B to a prediction derived from Eq. 2.1.

The increasing field section

The aforementioned discussion on the decreasing-field section applies to the increasing-field section as well. To only study the increasing-field section, data shown in this subsection are taken at $\eta_d = \eta_p = 0.65$, $L_d = 0.54$ m, and $P = 70$ mW.

Our data in Fig. 2.8(a) shows that N is not a monotonic function of i at a given δ. N first increases with i and reaches a peak at a critical value i_c, because a higher i leads to a larger deceleration which means more atoms can be slowed and captured in the MOT. When i is higher than i_c, we find that N sharply decreases with i due to atoms being over-slowed. Because $v_f = -(2\pi\delta + \mu B_{\mathrm{iMax}}/\hbar)/k$, the data points in Fig. 2.8(a) can be converted to reveal the relationship between N and v_f, as shown in Fig. 2.8(b). Here B_{iMax} is the maximum magnetic field strength created by the increasing-field section at a fixed i. We find four interesting results: N always peaks around $v_f = 40$ m/s $< v_c$ at any δ within the range of -450 MHz $\leq \delta \leq -650$ MHz; the minimal velocity of the atoms captured in the MOT appears to be $\sim$ 20 m/s; the maximum value of N does not depend on δ; and i_c linearly increases with δ, as shown in Fig. 2.8. Therefore, in addition to the procedures listed in Sections 2.1 and 2.2, another useful procedure in designing an optimal spin-flip Zeeman slower is as follows:

1. choose a convenient δ, for example, δ is around -500 MHz for sodium or lithium atoms;
2. find out the ideal length of the increasing-field section from the following equation, $L_i = (v_{\mathrm{sf}}^2 - v_c^2)/(2a_s) = [(2\pi\delta/k)^2 - v_c^2]/(2\eta_p a_{\max})$;
3. determine i_c from a figure similar to Fig. 2.8(a) and then set the current i at a value slightly smaller than i_c in the increasing-field coils.

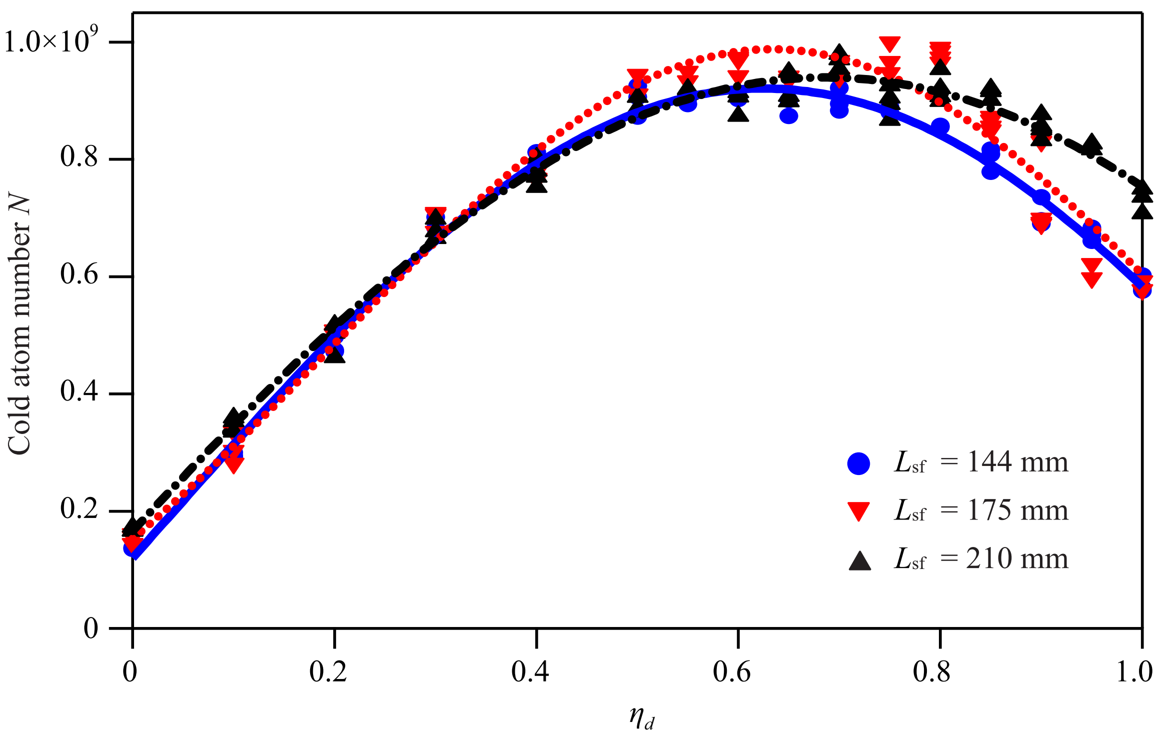

Figure 2.9: N as a function of η_d at three different L_{sf}, the length of the spin-flip section (see text). Lines are Gaussian fits to the data.

The spin-flip section

We have also studied the contribution of the spin-flip section, but have not found a strong correlation between the slower's efficiency and L_{sf}, the length of the spin-flip section. Figure 2.9 shows that N always peaks at $\eta_d \approx \eta_p = 0.65$ for three different values of L_{sf}, when L_d is kept at 0.54 m, η is set at 0.65 in the increasing-field section, δ is -512 MHz, and P is 70 mW. This figure also implies that a longer spin-flip section does not boost the number of atoms captured in the MOT, as long as its length L_{sf} is sufficient to fully re-polarize atoms. A very long L_{sf}, however, has a negative effect on the MOT capture efficiency, because it also unavoidably reduces the solid angle of the atomic beam when all other parameters of the system remain unchanged.

Simple 3-step procedure of designing an optimal Zeeman slower

Therefore, our data suggests that an optimal Zeeman slower may be designed with the following procedures:

1. determine η_p based on Eq. 2.4 from the available slowing beam intensity;
2. choose a convenient δ and find out the ideal lengths of the increasing- and decreasing-field sections from

   $$L_i = [(2\pi\delta/k)^2 - v_c^2]/(2\eta_p a_{\max}) \tag{2.8}$$

   and

   $$L_d = [9\pi k_B T/8m - (2\pi\delta/k)^2]/(2\eta_p a_{\max}), \tag{2.9}$$

   respectively;
3. set i at a value slightly smaller than i_c in the increasing-field coils and determine i of decreasing-field coils with our simulation program.

We have found that a longer spin-flip section does not boost the number of atoms captured in the MOT, as long as its length L_{sf} is sufficient to fully re-polarize atoms. These conclusions are very useful in designing an optimal Zeeman slower for other atomic species, especially those with high initial velocities, for example lithium atoms.

2.3 Electric coils and their control circuits

Good performance of a slower, a MOT, or a BEC requires highly controllable magnetic fields. In our sodium spinor system, besides the earth residual field, all additional magnetic fields are generated by electric coils. The coils for Zeeman slower is discussed in the previous section. In addition, we have a set of anti-Helmholtz MOT coils for MOT production and it can flip to Helmholtz coils for reaching Feshbach resonances. We also have three sets of Helmholtz coils to generate bias fields in three orthogonal directions, and one coil used as a RF field antenna. These coils have various control requirements and therefore have different control and driving circuits. In general, there are two type of requirements, i.e., switching control and linear control. Switching control only requires turning current on and off while linear control requires that the controlled current is proportional to the control signal. However, compare to linear control, switch control dissipates much less power, which allows a single chip to control a much higher current. In this section, I'll first discuss our feedback circuit used for linear control requirements. After that, I'll discuss each control and driving circuit.

2.3.1 The analog and digital fast feedback circuits

Time constants τ of our coils range from 3 ms to 9 ms, based on their resistances (4 $m\Omega \sim$ 220 $m\Omega$) and their inductances (15 μH $\sim$ 1500 μH). We can substantially reduce the settling time of each coil by increasing the maximum output voltage $V_{\rm ps}$ of the DC power supply. The required time t for raising electric current from 0 to i can be expressed as $t = -\tau \cdot \ln(1 - i/i_{\max})$, where $i_{\max}$ is the maximum electric current. Because a larger $V_{\rm ps}$ leads to a larger $i_{\max}$, a smaller rise time t is needed to reach the same value of i at a larger $V_{\rm ps}$. As a numerical example, t of our magnetic coils at 20A is reduced to $\sim$ 150 μs when $V_{\rm ps}$ is increased from 2 V to 20 V. This method, however, cannot stabilize current by itself. Figure 2.10 shows how we achieve the current stabilization with a cheap DC power supply and our feedback control circuits. This design enables us to rapidly and simply control various magnetic fields used for creating sodium BECs, as demonstrated in this Section. A standard ring-down circuit constructed from a resistor and a diode is connected in parallel with each coil for safely shutting off the inductive current in the coil. Note that without the feedback circuits, the cheap power supply has a very long settling time of $\sim$ 400 ms and produces a huge (>100%) current overshoot at 20 A.

An important chip in the design is STE250NS10, a high power MOSFET (Metal Oxide Semiconductor Field Effect Transistor) from STMicroelectronics Inc. The allowed current flowing through a MOSFET is limited by its gate voltage and its transconductance g_m. At a

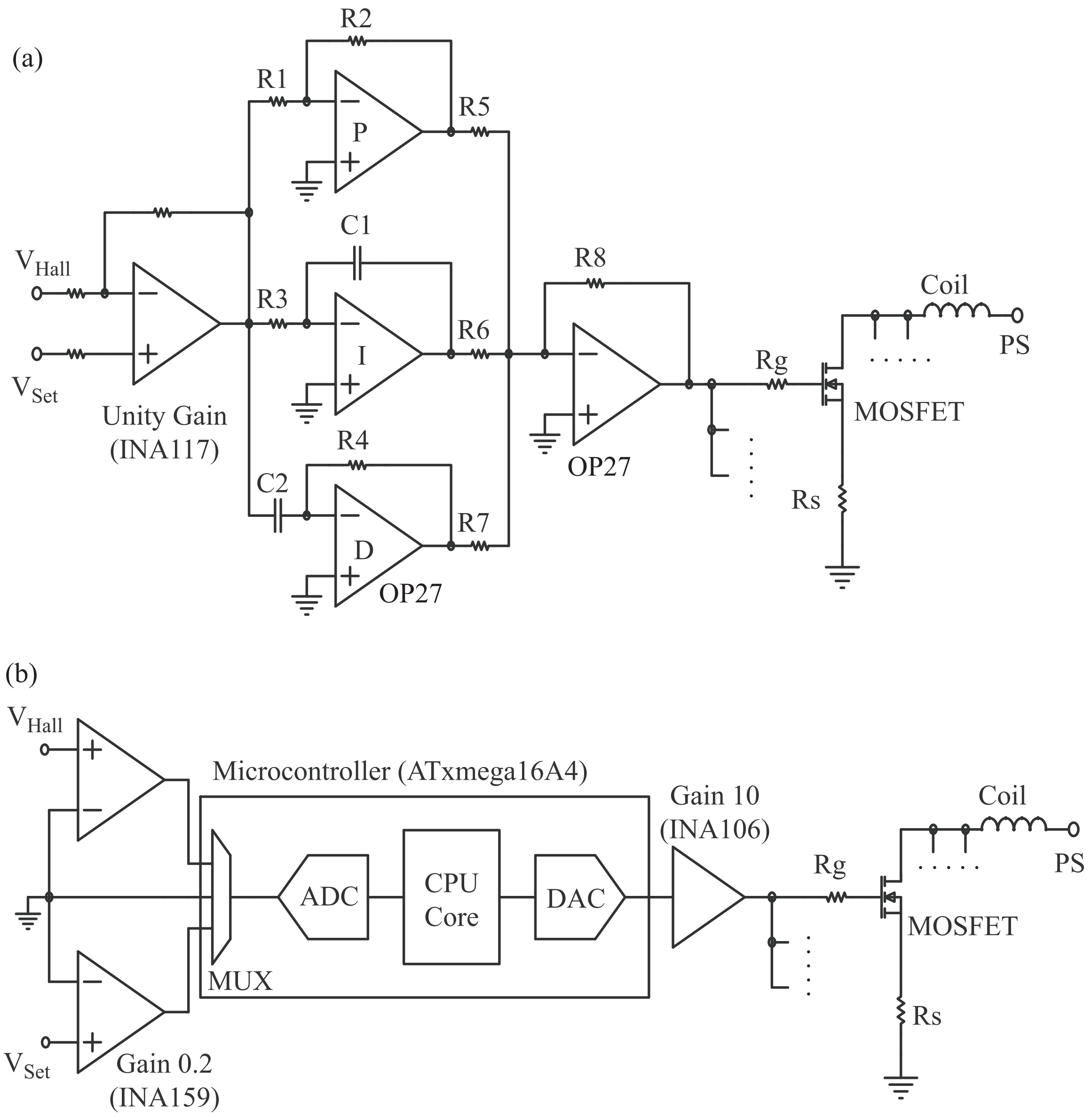

Figure 2.10: A simplified schematic of our (a) analog and (b) digital feedback circuits. The current flowing through a coil is measured with a Hall sensor. PS stands for a power supply. V_{Set} and V_{Hall} are the control voltage set by our computer program and the voltage measured by the Hall sensor, respectively. The analog circuit uses OP27 chips to construct its proportional (P), integral (I), and derivative(D) circuits. Various resistors (R_i) and capacitors (C_i) are listed, however, bypass capacitors and buffer chips as well as some internal resistors in INA amplifiers are not shown in the figure. A detailed schematic of printed circuit boards for the feedback circuits is available upon request.

given gate voltage, the current rises as the experiment progresses, because g_m can and does vary greatly even for the same MOSFET (Hayes and Horowitz, 1989). To precisely control the current, the MOSFETs are not operated in the switching mode and thus dissipate lots of power. For example, the dissipated power is ∼1400 W when V_{ps} is 20 V and i is 100 A. We use a number of MOSFETs connected in parallel and mount them on the top of a water-cooled cold plate to efficiently cool them. The dissipated power, however, is not divided evenly among MOSFETs because they have different values of g_m. There will be at least one MOSFET which dissipates more power than others do. The extra dissipated power brings a large positive temperature drift and thus a positive feedback to this MOSFET. As a result, this MOSFET starts to dissipate even more power. After a few such iterations, this MOSFET would be quickly burned out, which may even lead to burning magnetic coils. To avoid this problem, a carefully chosen resistor R_s is connected to each MOSFET's source terminal to encourage equal current division among the MOSFETs in parallel, as shown in Fig. 2.10. We find $\mathrm{R}_s = 50\ m\Omega$ works well for our design. The value of g_m varies from 0 Siemens to 60 Siemens for a wide range of the control signal $\mathrm{V}_{\mathrm{Set}}$ used in this report. Adding R_s limits g_m to a narrower range (i.e., 0 Siemens $\sim$ 20 Siemens), which allows us to apply a single set of gains in our feedback circuits for both low and high currents.

The current stabilization for MOSFET controlled magnetic coils is normally achieved with an extra feedback circuit, such as our analog and digital feedback circuits shown in Fig. 2.10. The current flowing through coils is measured with a Hall sensor. We use INA117 op-amps to isolate the grounds on both $\mathrm{V}_{\mathrm{Set}}$ and the signal from the Hall sensor $\mathrm{V}_{\mathrm{Hall}}$. In the analog circuit, we also use an INA117 as a unity gain differential amplifier to produce an error signal, $\mathrm{V}_{\mathrm{error}} = \mathrm{V}_{\mathrm{Set}} - \mathrm{V}_{\mathrm{Hall}}$. Figure 2.10(a) shows that $\mathrm{V}_{\mathrm{error}}$ is split into proportional (P), integral (I), and derivative (D) circuits. The gains of these three circuits are K_P, K_I, and K_D, respectively. The outputs from the P, I, and D circuits are combined to one signal by an inverting summing amplifier. This signal is sent to a buffer chip to boost the maximum amount of current that the circuit can output to 250 mA, and then is transmitted to the MOSFET's gate terminal. The analog feedback circuit is carefully tuned by manually adjusting the values of K_P, K_I, and K_D.

The digital control circuit has a completely different design, as shown in Fig. 2.10(b). One standard micro-controller (ATxmega16A4) is sufficient to implement the P, I, and D controls. In the micro-controller, an analog to digital converter (ADC) collects the two signals $\mathrm{V_{Set}}$ and $\mathrm{V_{Hall}}$. The ADC has a sample rate of 2 MHz and a propagation delay time of 3 μs. The main CPU needs 4 μs to process the signals, and the conversion time of a DAC (digital to analog converter) is 1 μs. Our digital feedback circuit can thus be operated at a sample rate of 250 kHz with a propagation delay time of 8 μs. The processed signal is amplified by an INA106 chip, and then is sent to the MOSFET's gate terminal. The digital feedback circuit is automatically tuned via our simple program.

Magnetic coils controlled only by MOSFETs can generate an adjustable magnetic field. The current that flows through the coils, however, quickly rises with time due to the MOSFET's temperature drift, as shown by solid (red) lines in Fig. 2.11. The inset of Fig. 2.11 also implies that there are other serious problems with this control method, such as long response time, huge current overshoot, and large oscillations due to the non-negligible capacitance between MOSFET's gate and source terminals. With an extra feedback circuit (e.g., our analog and digital designs), the magnetic field stabilization can be achieved via stabilizing the current flowing through the coils. This is well confirmed by dotted (blue) lines and dashed (green) lines in Fig. 2.11.

Our analog circuit must be manually tuned. While tuning a PID controller, one must balance rise and settling time. A larger K_P or K_I means a shorter rise time, however, it also leads to larger current overshoot which results in a longer settling time. A large K_D can lessen overshoot but it also can cause a decrease in stability for steady signals. Excessive gains can even cause oscillations. When i is less than 300 A, we find that the coils are always controllable with $\mathrm{K}_P = 7.1$, $\mathrm{K}_I = 21.5\ \mathrm{s}^{-1}$, and $\mathrm{K}_D = 0$ s, as shown by the dotted (blue) lines in Fig. 2.11. With our MOT coils, the high current at 300 A is sufficient to generate a deep magnetic trap used for creating sodium BECs. The main advantage of our analog design is its faster settling time. However, the gains used are probably not optimal, because this design must be manually tuned. This design also has problems with integral wind-up if $\mathrm{V_{Set}}$ is allowed to pass outside the controllable range. This means the responding time becomes extremely long when $\mathrm{V_{Set}}$ goes below the zero current signal of the Hall sensor. Adding a voltage clamp to $\mathrm{V_{Set}}$ could help reduce this problem.

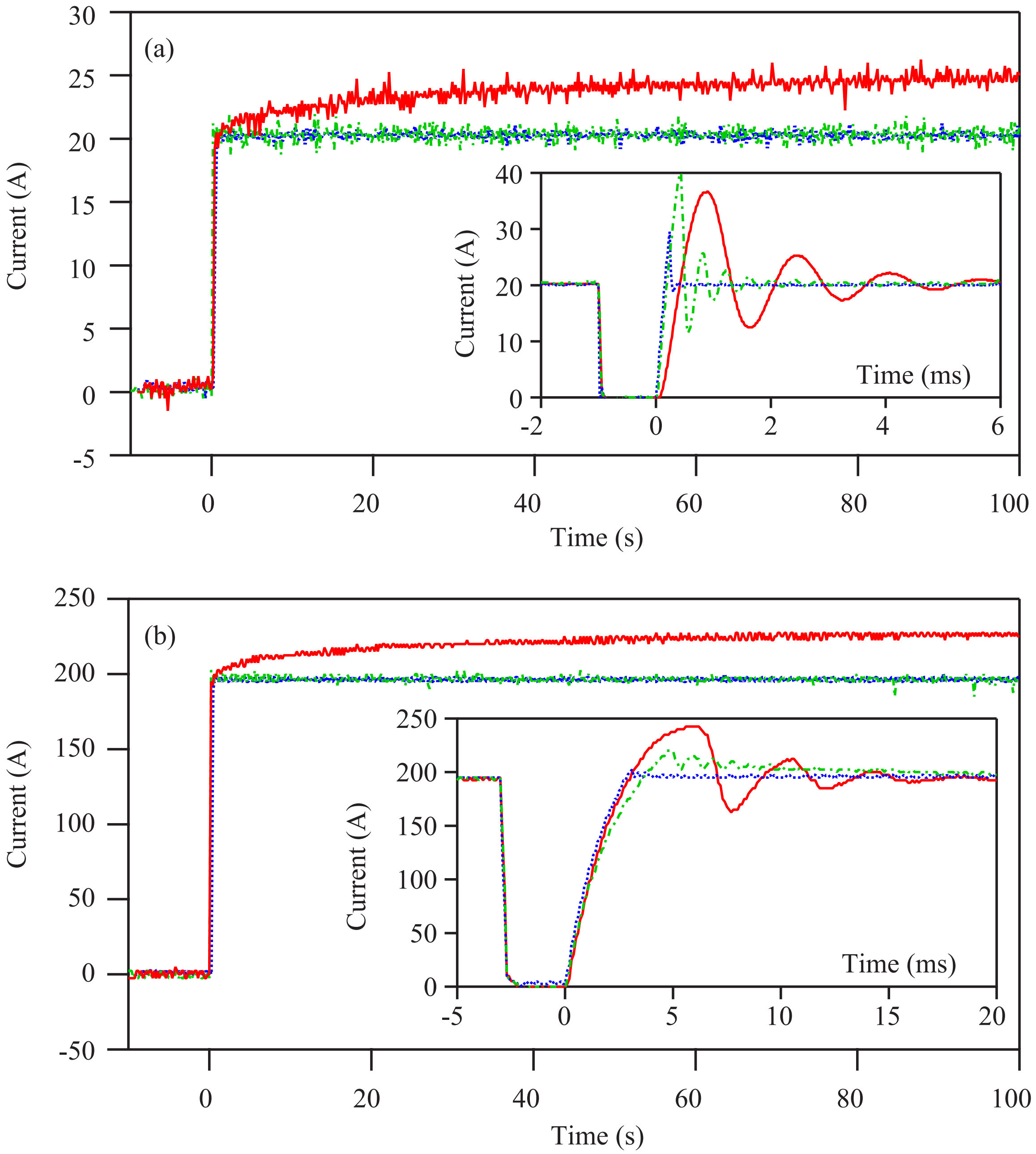

Figure 2.11: The electric current stability of our magnetic coils at (a) 20 A and (b) 190 A via three different control methods. These performances are typical for each control method at any current less than 300 A. Solid (red) lines, dotted (blue) lines, and dashed (green) lines represent the current flowing through the coils controlled only by MOSFETs, by MOSFETs and our analog feedback circuit, and by MOSFETs and our digital feedback circuit, respectively. The power supply is always set at 20 V. For this test, we used our MOT coils with a total resistance of 60.4 $m\Omega$ and a total inductance of 130 μH. Inset: A much shorter time scale (-5 ms $\sim$ 20 ms) showing both the rising and falling edges.

The digital design is automatically tunable and does not display any issues with integral wind-up, although it appears to have a longer settling time and bigger current overshoot than the analog design. The best performance of the digital design is shown in Fig. 2.11, where K_P is allowed to change between 1 and 4, $K_I = 0.49$ ms^{-1}, and $K_D = 16$ μs. A capacitor C_g can be added between the MOSFET's gate terminal and the ground to further reduce oscillations, but C_g will also increase the settling time. A faster processor and a better ADC can also improve the performance of the digital feedback circuit.

Compared to the control method with only MOSFETs, Fig. 2.11 shows that our analog and digital designs display improved response time and good current stability over 100 s. A coil controlled by our feedback circuits always settles at the same point for the same value of V_{Set}. In contrast, the same coil controlled only by MOSFETs has a large variance Δ in the amount of current initially allowed through the coil for the same V_{Set}. The value of Δ depends on many factors, for example how recently the coil has been used. Our feedback designs are thus much more reliable. A hybrid circuit combining the advantages of the two feedback designs may be a better solution.

2.3.2 MOT coil driving circuit

The MOT coils are constructed by a pair of 24 turns anti-Helmholtz coils. Magnetic coils are wounded from Kapton insulated 3.18 mm hollow square copper tubes. High pressure ($\sim$ 150 psi) chilled water flowing through the hollow tubes is sufficient to keep all coils at the room temperature. A standard ring-down circuit constructed from a resistor and a diode is connected in parallel with each coil for safely shutting off the inductive current in the coil as well. The MOT coils are controlled by a linear control circuit as shown in Fig. 2.12. The current stabilization circuit with feedback control is discussed in the previous subsection. This stabilization circuit is essential for keeps the current through the coil proportional to the control signal.

To switch the coils between a Helmholtz and an anti-Helmholtz setup, a Helmholtz/anti-Helmholtz switching circuit is connect to one of the coils. This circuit is constructed by four

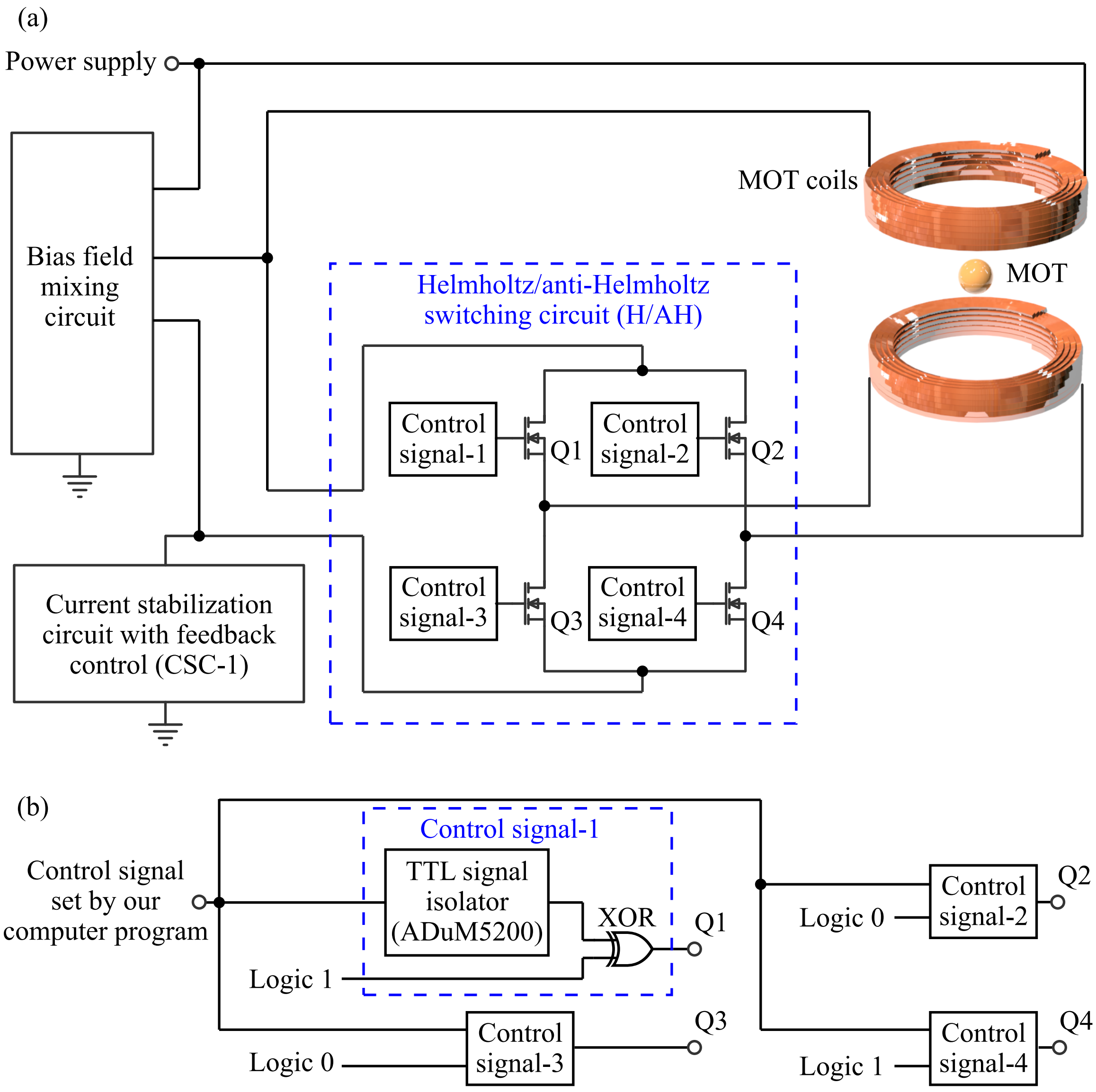

Figure 2.12: (a) A simplified schematic of our MOT coils control circuits. The schematic of the bias field mixing circuit is shown in Fig. 2.13. The schematic of the current stabilization circuit with feedback control is shown in Fig. 2.10. The blue dashed block shows the Helmholtz/anti-Helmholtz switching circuit. Q1-Q4 are MOSFETs. Detail schematics of control-signals are shown in panel (b). (b) A simplified schematic of the control-signals. The control signals are identical and only the first one is shown. Terminals Q1-Q4 are the gate pins of each MOSFET, respectively. XOR is a exclusive-OR logic gate. Logic 1 or 0 is set through a switch on the circuit board. Bypass capacitors and buffer chips as well as some protecting fuses and ring-down circuit of each coil are not shown in the figure. A detailed schematic of printed circuit boards for the MOT coils driving circuit is available upon request.

STE250NS10 MOSFETs Q1-Q4 and their corresponding driving circuits. These MOSFETs are operating in switching mode, and able to allow a very high current through them. The four driving circuits for MOSFETs are identical, and one of them is shown in Fig. 2.12(b). A TTL signal isolator is used to isolate the ground of each driving circuit from the common ground so this floating ground can be connected to the corresponding MOSFET's source pin which is not the common ground. A XOR logic gate SN74LVC2G86 is use for both adjust the logic and driving the MOSFET. The logic of one of its input pins is fix by a switch on the circuit board. The gate will act as a NOT logic gate when this input pin is fixed at logic 1, and act as a buffer when this input pin is fixed at logic 0. For the schematic shown in Fig. 2.12(b), when an anti-Helmholtz field is needed, the control signal set by our computer program is set to logic 0, MOSFETs Q1 and Q4 are switched on while Q2 and Q3 are switched off. Therefore, currents in two coils are in different directions. When the control signal set by our computer program is set to logic 1, the above discussion is vice versa and therefore, the magnetic field becomes a Helmholtz field. This switch design do not have any dead zone control, which means the MOSFETs may be simultaneously on or off for a very short period of time during the switching. This is due to unpredicted propagating time through the driving chips. However, since the circuit is in series with a current stabilization circuit and a coil with a high inductance, there should be no penetrating current even without dead zone control. Even though, as a precaution, we still lower down the current before switching this circuit at all times.

We also mix a small bias field into the magnetic field generated by the anti-Helmholtz coils by using the bias field mixing circuit. This small bias field pushes MOT slightly and makes it perfectly match the ODT center. This method helps us boost the ODT transfer efficiency without realigning ODT beams. Suppose we need currents I_{AH} and $-I_{AH}$ in the two MOT coils to generate a anti-Helmholtz magnetic field $\mathbf{B}_{AH}(\mathbf{x})$ and need current I_H in both two MOT coils to generate a Helmholtz magnetic field $\mathbf{B}_H(\mathbf{x})$. The mixed field $\mathbf{B}(\mathbf{x}) = \mathbf{B_H}(\mathbf{x}) + \mathbf{B_{AH}}(\mathbf{x})$ can be generated by currents $I_{AH}+I_H$ and $-I_{AH}+I_H$ respectively in each coil due to the superposition principle of magnetic fields. Since I_H is much smaller than I_{AH}, the Helmholtz/anti-Helmholtz switch is set to anti-Helmholtz and the controlled

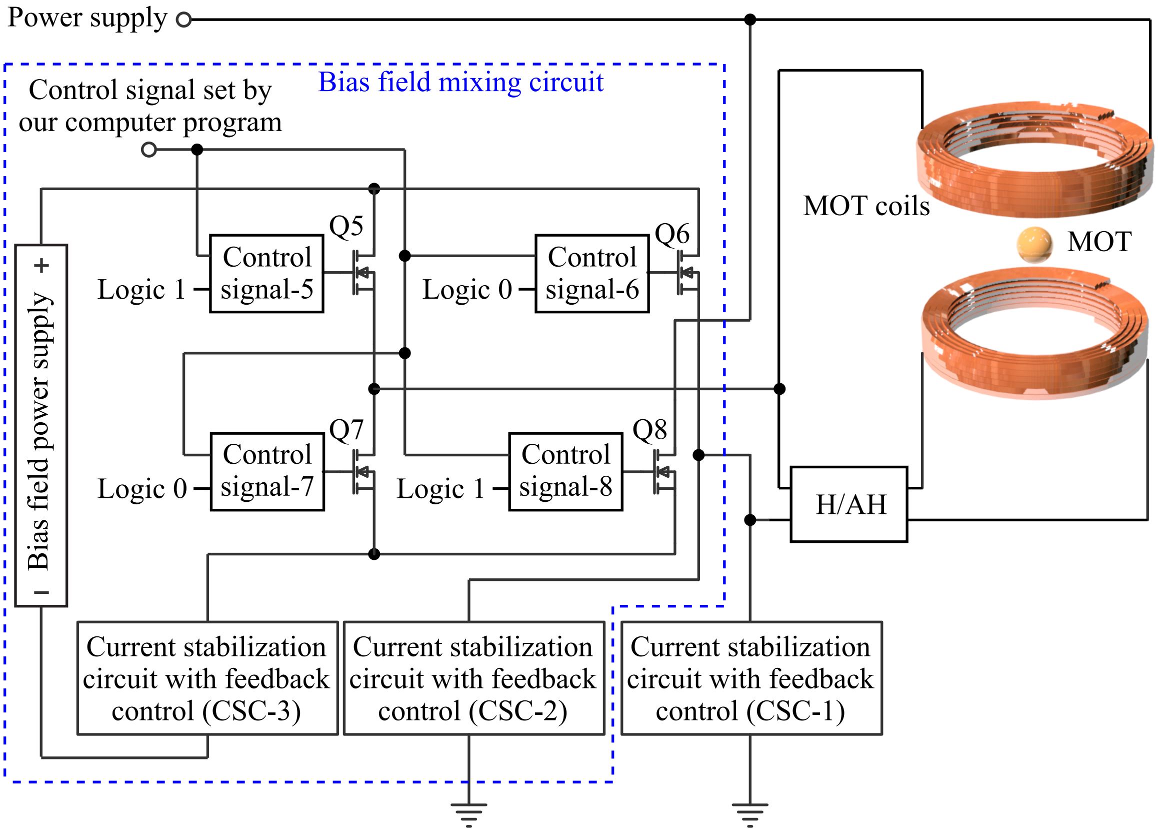

Figure 2.13: A simplified schematic of bias field mixing circuit, which is a part of our MOT coils control circuits. The H/AH is the the Helmholtz/anti-Helmholtz circuit and its schematic is shown in Fig. 2.12(a). The schematic of the current stabilization circuits with feedback control (CSC-1 to CSC-3) are shown in Fig. 2.10. The blue dashed block shows the bias field mixing circuit. Q1-Q4 are MOSFETs. Detail schematic of control-signals are shown in Fig. 2.12(b). Logic 1 or 0 is set through a switch on the circuit board. The bias field power supply is an isolated power supply without connect to the common ground. Bypass capacitors and buffer chips as well as some protecting fuses and the coil ring-down circuit are not shown in the figure. A detailed schematic of printed circuit boards for the MOT coils driving circuit is available upon request.

current of the main feedback control CSC-1 in Fig. 2.13 is set to I_{AH}. Then the feedback control CSC-2 is set to the current equaling to the magnitude of I_H. Therefore, currents of I_H are added to both two MOT coils with directions same as I_{AH} . Meanwhile, the current controlled by the feedback control CSC-3 is set to the magnitude of $2I_H$, and sent through a counter propagating direction from I_{AH} on only one of the MOT coils. Therefore, the overall current on the two MOT coils respectively are $I_{AH} \pm I_H$ and $-I_{AH} \pm I_H$. The plus or minus sign depends on which one of the MOT coils does CSC-3 connects. This selection is done by MOSFETs Q5-Q8. Since the current I_H is not large and for both space saving and budget saving, we choose four small MOSFETs, which are AOD4132 from Alpha & Omega Semiconductor Inc. These chips have ultra-low drain-source resistances at $\sim$ 6 mΩ even when using TTL driving signals, and therefore, they have small thermal dissipations. This allows them to run at $\sim$ 20 A currents even using copper layers on printed circuit boards as heat sinks. These MOSFETs are controlled by a control signal set by our computer program. When our computer program sends a logic 0, MOSFETs Q5 and Q8 are switched on and Q6 and Q7 are switched off. Under this condition, CSC-3 is connected to the top MOT coils, as shown in Fig. 2.13. When our computer program sends a logic 1, in contrast, CSC-3 is connected to the bottom MOT coil. By using this method, we add a small bias field on either direction to the anti-Helmholtz field.

2.3.3 Bias coil driving circuit

Our experiments on spinor BECs require high precise controls on bias magnetic fields. To generate a wide range of magnitudes of magnetic fields in an arbitrary direction, our bias field coils are constructed by three pairs of Helmholtz coils in three orthogonal directions. These coils are wounded from 16-gauge magnet wires on Delrin mounting rings. Four of these mounting rings are then mounted on the four 4.5” windows of the main chamber, and two are hanging on the top and bottom of the main chamber. These three pairs of coils are driven by three identical and interchangeable driving circuits.

Figure 2.14 shows a typical schematic of the circuit. An important chip in this design is OPA549, a high current op-amp from Texas Instruments Inc. It provides an output current up to 8 A in either directions. This design allows us easily ramp a current across zero without switching any MOSFETs. The 2Ω resistor R_f is used as a current sensor and by measure the voltage across it, we can detect a small current more accurately. This voltage is used as a feedback signal and send back to the feedback controller. The feedback controller is a well-adjusted PID controller controlled by a control signal set by our computer program. The ratio between the control signal and the output current is determined by R_f. When $R_f = 2\ \Omega$, 1 V control signal brings a 0.5 A output current. As a consequence, the

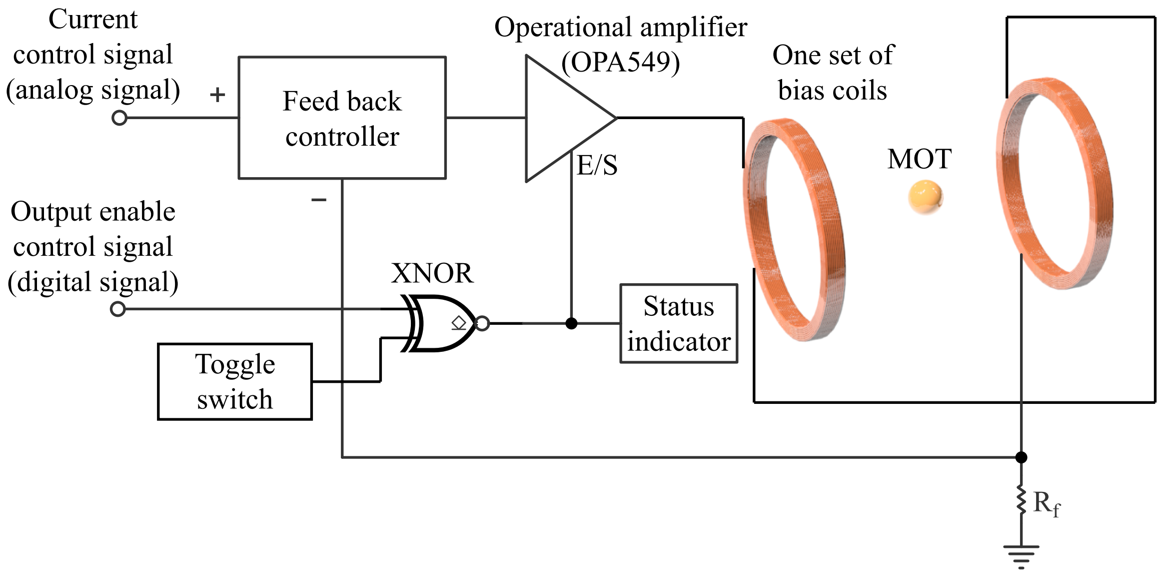

Figure 2.14: A simplified schematic of our bias coils driving circuits. The E/S pin is the Enable/Status pin use for both monitor the chip status and force shutdown the chip (see text). The XNOR is an exclusive-NOR logic gate circuit with an open collect output constructed by a SN74LVC1G86 chip and a SN74LVC2G06 chip. The two states of the manual controlled toggle switch are logic 0 and 1. The status indicator has a led and the led respectively turns green or red when input is logic 1 or 0. Bypass capacitors, buffer chips and optocouplers as well as some protecting fuses are not shown in the figure. A detailed schematic of printed circuit boards for the bias coils driving circuit is available upon request.

stability of R_f is essential for the stability of the output current in this circuit. To minimize the output current fluctuation, we use a low temperature drift, high accuracy, high power resistor mounted on a heat sink with forced air flow to minimize both the temperature and the resistance drift.

Another control signal set by our computer program, the output enable signal, is send to the E/S pin of the op-amp together with a manual toggle switch signal. The E/S pin provides two functions. It can disable the output and disconnect the coils by set it to logic 0. This setting can be done by either the manual toggle switch or the control signal. This pin is also monitored to determine if the op-amp is shut down by its protecting circuits and the status is indicated by an led.

By controlling three sets of these coils, we can generate an arbitrary magnetic bias field in a wide range. The field is further calibrated by using an rf-pulse. The calibration will be discuss in the next chapter.

2.4 Computer control and isolation circuits

The controlling computer equips three analog output cards and one digital output card. The analog output cards are NI PCI-6733 from National Instruments, Inc. Each card has eight analog output channels with up to 1 million samples per second per channel. Each channel is connected to an individual analog isolation circuit for both protecting damage from incorrect circuit hook up and providing a floating ground to minimize ground loop issues. Each isolation circuit is constructed by two chips, an INA117 for input isolation and a BUF634 for output driving. In addition, each circuit is complemented with an individual power module as well as some bypass capacitors to ensure the ground isolation.

The digital output card is PulseBlaster from SpinCore Technologies, Inc. This card has twenty-four independently controlled output channels with a time resolution up to 10 ns. Similar to the analog protection circuits, an individual isolation circuit is connected to each channel. In addition, the isolation circuits are also used as TTL/CMOS signal level converters since some of our equipment needs a CMOS control signal, e.g., the digital camera from Point Gray Research, Inc. Each digital isolation circuit is constructed by an optocoupler PS2501-1 and some resistors to adjust the output signal level.

These driving circuits essentially improve the reliability of our system and protect some of the crucial equipments.

CHAPTER III

DYNAMICS IN SPINOR BOSE-EINSTEIN CONDENSATES TUNED BY A MICROWAVE DRESSING FIELD

This chapter discusses our experimental studies on the spin-mixing dynamics and phase diagram of spinor condensates tuned by a microwave dressing field. Two papers related to these topics were published:

- L. Zhao, J. Jiang, T. Tang, M. Webb, and Y. Liu, *Dynamics in spinor condensates tuned by a microwave dressing field*, Phys. Rev. A **89**, 023608 (2014). Included in Appendix B.
- J. Jiang, L. Zhao, M. Webb, and Y. Liu, *Mapping the phase diagram of spinor condensates via adiabatic quantum phase transitions*, Phys. Rev. A **90**, 023610 (2014). Included in Appendix D.

After the three-year hard work, our group achieved the first sodium BEC in Oklahoma in 2012. A few research projects have been conducted with sodium BECs in our lab. In this chapter, I will discuss the project which I have been leading: study the spin-mixing dynamics of a F=1 sodium spinor condensate starting from a non-equilibrium initial state. The spin-mixing dynamics is driven by the net quadratic Zeeman energy $q_{\rm net}$ and antiferromagnetic spin-dependent interactions c. It is well known that $c > 0$ (or $c < 0$) in F=1 antiferromagnetic ^{23}Na (or ferromagnetic ^{87}Rb) spinor BECs. In contrast to a magnetic field, a microwave dressing field enables us to access both negative and positive values of $q_{\rm net}$. In both negative and positive $q_{\rm net}$ regions, we observe spin population oscillations resulted from coherent collisional interconversion among two $|F = 1, m_F = 0\rangle$ atoms, one $|F = 1, m_F = +1\rangle$ atom, and one $|F = 1, m_F = -1\rangle$ atom. In every spin oscillation studied in this report, our data shows that the population of the $m_F = 0$ state averaged over time is always larger (or smaller) than its initial value as long as $q_{\rm net} < 0$ (or $q_{\rm net} > 0$). This observation provides a clear experimental signature to determine the sign of $q_{\rm net}$. We also find a remarkably different relationship between the total magnetization m and a separatrix in phase space where spin oscillation period diverges: the position of the separatrix moves slightly with m in the positive $q_{\rm net}$ region, while the separatrix quickly disappears when m is away from zero in the negative $q_{\rm net}$ region. Our data agree with an important prediction derived by Ref. (Lamacraft, 2011): the spin-mixing dynamics in F=1 spinor condensates substantially depends on the sign of $R = q_{\rm net}/c$. This work may thus be the first to use only one atomic species to reveal mean-field spin dynamics, especially the relationship between each separatrix and the magnetization, which are predicted to appear differently in F=1 antiferromagnetic and ferromagnetic spinor condensates. In addition, a method to characterize microwave dressing fields and an approach to adiabatically sweep $q_{\rm net}$ from $-\infty$ to $+\infty$ will be explained in this section.

3.1 The Hamiltonian of spinor BECs

The Hamiltonian of spinor BECs in our system has four important terms as follows,

$$\hat{H} = \hat{H}_K + \hat{H}_V + \hat{H}_Z + \hat{H}_{int} \ , \tag{3.1}$$

where $\hat{H}_K$, $\hat{H}_V$, $\hat{H}_Z$ and $\hat{H}_{int}$ are kinetic, potential, Zeeman, and interaction energy parts of the Hamiltonian, respectively. The first two terms $\hat{H}_K$ and $\hat{H}_V$ are independent of spin, and the last two terms $\hat{H}_Z$ and $\hat{H}_{int}$ are spin-dependent terms. In the next three sections, $\hat{H}_Z$ and $\hat{H}_{int}$ will be discussed.

3.2 The Zeeman energy

For neutral alkali metal atoms like ^{23}Na and ^{87}Rb, the $F = 1$ hyperfine state have three Zeeman states, $|F = 1, m_F = +1\rangle$, $|F = 1, m_F = 0\rangle$ and $|F = 1, m_F = -1\rangle$ states, and their energies are E_{m_F}. We use $p_{\text{net}} = (E_{+1} - E_{-1})/2$ and $q_{\text{net}} = (E_{+1} + E_{-1} - 2E_0)/2$ to represent the linear Zeeman energy and the quadratic Zeeman energy, then $\hat{H}_Z$ may be expressed as,

$$\hat{H}_Z = \int d\mathbf{r}(p_{\text{net}}\hat{F}_z + q_{\text{net}}\hat{F}_z^2) \tag{3.2}$$

where $\hat{F}_\gamma = \sum_{i,j=-1}^{1} \hat{\phi}_i^\dagger(\mathbf{r})(f_\gamma)_{ij}\hat{\phi}_j(\mathbf{r})$ with $\gamma = x, y, z$ is the γ-component of $\hat{\mathbf{F}}$, $\hat{\phi}_{m_F}(\mathbf{r})$ is the field operator that annihilates an atom in m_F state at the location $\mathbf{r}$. f_γ are the spin-1 matrices which are expressed as,

$$f_x = \frac{1}{\sqrt{2}}\begin{pmatrix} 0 & 1 & 0 \\ 1 & 0 & 1 \\ 0 & 1 & 0 \end{pmatrix}, \; f_y = \frac{1}{\sqrt{2}}\begin{pmatrix} 0 & -i & 0 \\ i & 0 & -i \\ 0 & i & 0 \end{pmatrix}, \; f_z = \begin{pmatrix} 1 & 0 & 0 \\ 0 & 0 & 0 \\ 0 & 0 & -1 \end{pmatrix}, \tag{3.3}$$

and $(f_\gamma)ij$ is the corresponding (i, j) matrix element.

Since the only interesting coherent collision is the coherent interconversion among two $|F = 1, m_F = 0\rangle$ atoms, one $|F = 1, m_F = +1\rangle$ atom, and one $|F = 1, m_F = -1\rangle$ atom, the energy difference during the collision is only related to the quadratic Zeeman energy. The induced linear Zeeman shift remains the same and is thus ignored.

With no external magnetic fields, these three states are degenerate. However, when an external magnetic field exists, these three states split. According to the Breit-Rabi formula (Breit and Rabi, 1931), the energy of these states under a magnetic field $\mathbf{B} = B\hat{z}$ along the quantization axis may be expressed as,

$$\begin{aligned} E_\pm &= -\frac{E_{\text{HFS}}}{8} \pm g_I\mu_I B - \frac{1}{2}E_{\text{HFS}}\sqrt{1 \pm \alpha + \alpha^2}\;, \\ E_0 &= -\frac{E_{\text{HFS}}}{8} - \frac{1}{2}E_{\text{HFS}}\sqrt{1 + \alpha^2}\;, \end{aligned} \tag{3.4}$$

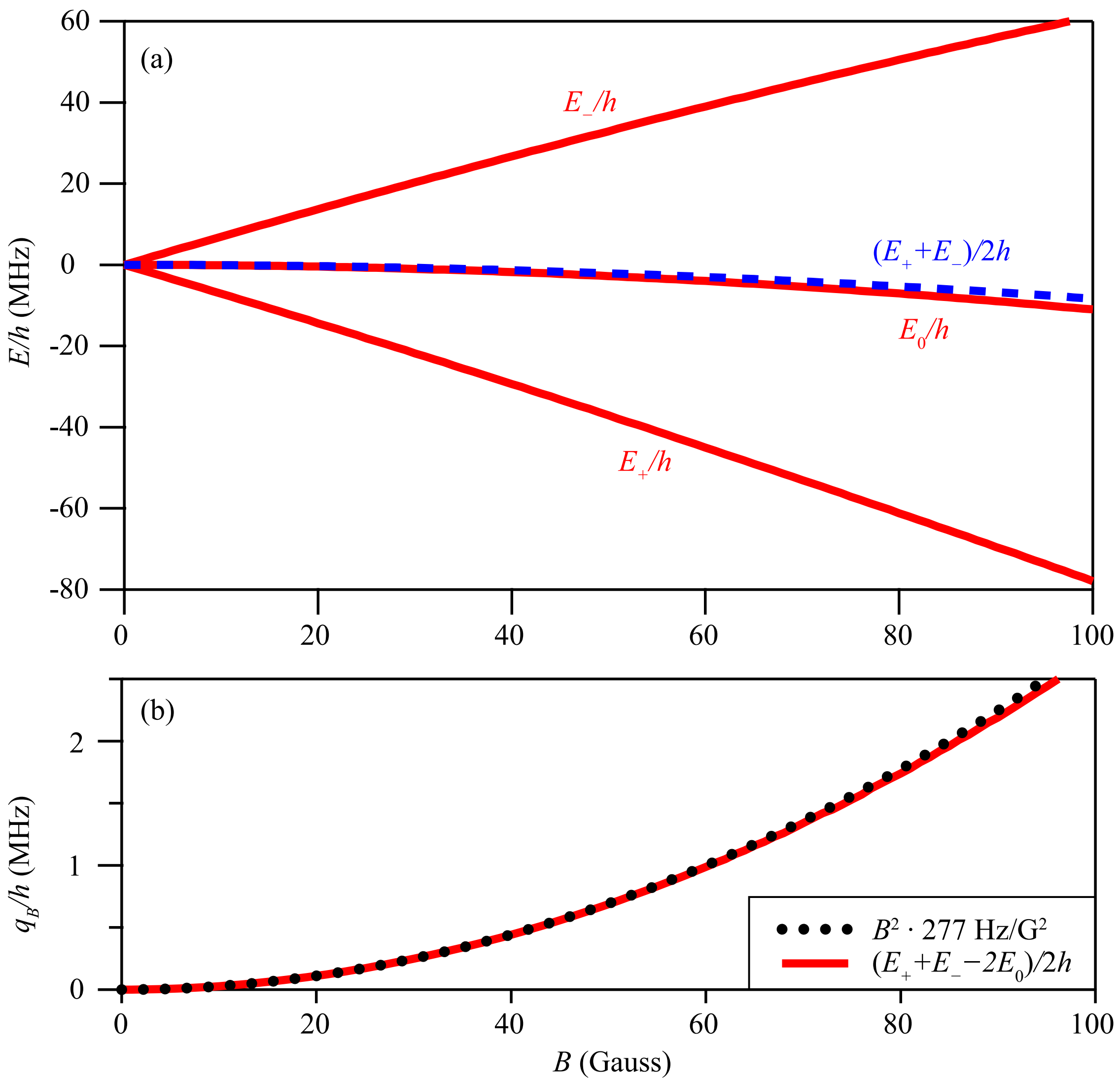

Figure 3.1: (a) Zeeman energy shifts for all three sublevels of $F = 1$ sodium atoms in an external magnetic field $\mathbf{B} = B\hat{z}$. The blue dashed line is the average energy of the $|F = 1, m_F = 1\rangle$ and $|F = 1, m_F = -1\rangle$ states. (b) Quadratic Zeeman shift for $F = 1$ sodium atoms under the external magnetic field $\mathbf{B} = B\hat{z}$. The red solid line is direct obtained from the Breit-Rabi formula and the black dotted line is using $q_B/h \approx B^2 \cdot 277$ Hz/G^2.

where E_{HFS} is the hyperfine splitting, $\alpha = (g_J\mu_B - g_I\mu_I)B/E_{\text{HFS}}$, g_I, g_J respectively represent the Lande g factor for an atom and for a valence electron, and μ_I, μ_B respectively represent the nuclear magneton and the Bohr magneton. These energy as a function of the magnetic field B is shown in Fig. 3.1(a). Figure 3.1(a) also shows that the average energy of $|F = 1, m_F = +1\rangle$ and $|F = 1, m_F = -1\rangle$ states (blue dashed line) are always larger than the energy of the $|F = 1, m_F = 0\rangle$ state. In other words, the magnetic field induced quadratic Zeeman energy q_B remains positive, which is shown in Fig. 3.1(b). By using Eq. 3.4 and ignoring the high order terms of α, we find

$$q_B = \frac{g_J\mu_B - g_I\mu_I}{16E_{\mathrm{HFS}}}B^2 \ , \tag{3.5}$$

i.e., $q_B \approx B^2 h{\cdot}277$ Hz/G^2 for ^{23}Na and $q_B \approx B^2 h{\cdot}71.9$ Hz/G^2 for ^{87}Rb. This approximation works well when $B < 100$ G for ^{23}Na and $B < 500$ G for ^{87}Rb as shown in Fig. 3.1(b).

3.3 Microwave dressing fields

The quadratic Zeeman energy q_{net} can also be obtained by other methods, e.g., a microwave dressing field (Gerbier *et al.*, 2006; Leslie *et al.*, 2009b; Stamper-Kurn and Ueda, 2013; Bookjans *et al.*, 2011; Leslie, 2008) or a linearly polarized off-resonant laser beam (Santos *et al.*, 2007) can both shift the quadratic Zeeman energy. Importantly, in contrast to the positive q_B generated by magnetic fields, these methods give us opportunities to reach both positive and negative region of q_{net}. In our experiment, we use the first method to reach a desired q_{net}.

Under a magnetic field, both $F = 1$ and $F = 2$ hyperfine states split as shown in Fig. 3.2. There are nine possible transitions between these two hyperfine states after taking the selection rule into account and only counting single photon transitions. In order to shift the energy of these states, we apply a microwave field at a frequency near the resonance of these transitions. To prevent atoms from populating $F = 2$ states, the microwave field is detuned from all these transitions. Therefore, we call it a microwave dressing field. The energy shift is due to the field induced AC Stark effect, which is a second-order process of the electric dipole interaction between an electric field and atoms. This AC Stark effect is similar to the one induced by ODTs but has two major differences. First, ODTs have strong spatial dependences while microwave dressing fields are spatially homogeneous fields within the size of a typical BEC. Second, the frequency detuning of an ODT is usually much larger than the energy difference between Zeeman states, which makes ODTs spin-independent

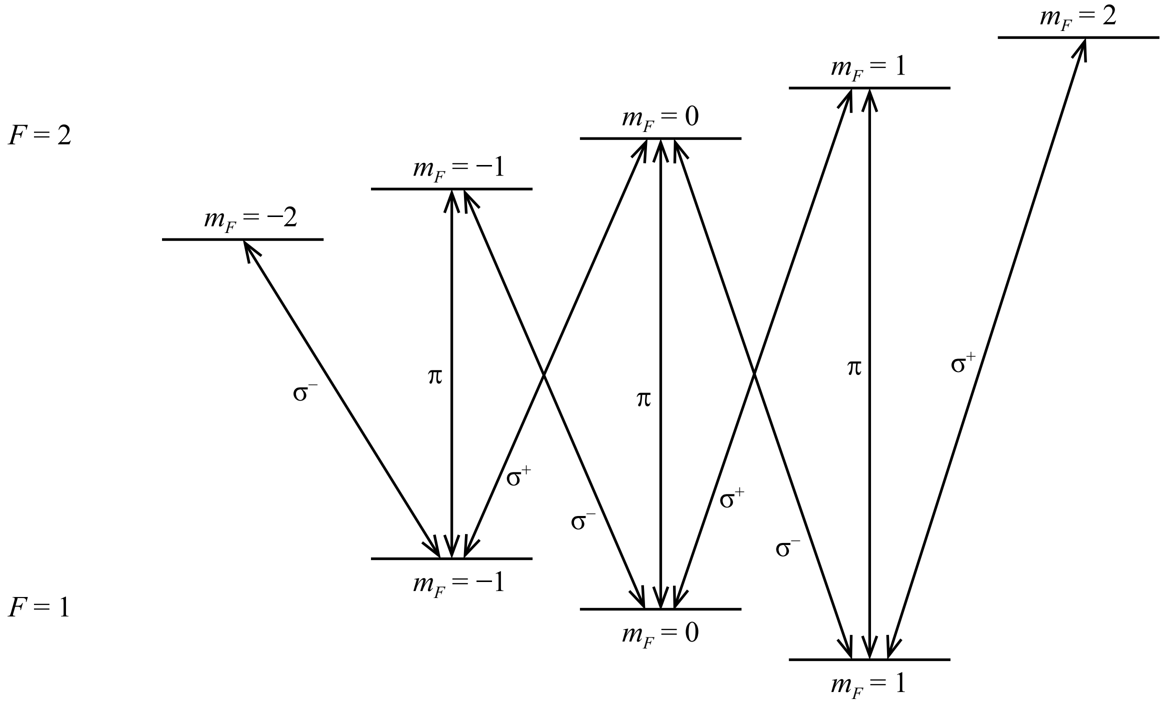

Figure 3.2: $F = 1$ and $F = 2$ hyperfine structures of $3^2\mathrm{S}_{1/2}$ level of ^{23}Na atoms under an external magnetic field. Allowed transitions are shown by arrows, and corresponding polarization of microwave fields are labelled. Energy levels are not to the scale.

traps. In contrast, we intentionally choose the frequency of our microwave pulses so that they are differently detuned with respect to each transition between $F = 1$ and $F = 2$ states. Therefore, spin-dependent energy shifts are expected from these microwave dressing fields.

We consider a two-level simple structure, which has only a ground state $|\mathrm{g}\rangle$ and an excited state $|\mathrm{e}\rangle$ and their energy difference is $h\omega_0$. The Hamiltonian may thus be expressed as,

$$H_0 = \frac{h}{2}\begin{pmatrix} -\omega_0 & 0 \\ 0 & \omega_0 \end{pmatrix} . \tag{3.6}$$

When a microwave dressing field with an electric field magnitude $\mathcal{E}$ and frequency ω is applied to the BEC system, the Rabi frequency Ω equals to $2\langle \mathrm{e}|\mathcal{E}\cdot\mathbf{d}|\mathrm{g}\rangle/h$, where $\mathbf{d}$ is the electric dipole moment of the atom. Note that the Rabi frequency is proportional to $\mathcal{E}$ and thus proportional to the square root of the microwave field intensity. This dipole interaction

Hamiltonian may be expressed as,

$$H_1 = \frac{h}{2}\begin{pmatrix} 0 & \Omega\cos(\omega t) \\ \Omega^*\cos(\omega t) & 0 \end{pmatrix} . \tag{3.7}$$

When the frequency detuning $\Delta = \omega - \omega_0$ is much larger than the linewidth of the transition line and H_1 is much less than H_0, the calculation can be done in a rotating frame. After applying the second-order perturbation theory, the energy shift is derived as,

$$\begin{aligned} \delta E &= \frac{|\langle \mathrm{e}|\mathcal{E}\cdot\mathbf{d}|\mathrm{g}\rangle|^2}{\Delta} \\ &= \frac{h}{4}\frac{\Omega^2}{\Delta} . \end{aligned} \tag{3.8}$$

For an allowed transition $|F=1, m_F\rangle \leftrightarrow |F=2, m_F+k\rangle$, the resonance frequency ω_0 may be expressed as,

$$\omega_0|_{m_F,m_F+k} = \omega_0|_{0,0} + [\frac{1}{2}(m_F+k) - (-\frac{1}{2}m_F)]\mu_B B , \tag{3.9}$$

where $\omega_0|_{0,0}$ is the resonance frequency of $|F=1, m_F=0\rangle \leftrightarrow |F=2, m_F=0\rangle$ transition, k is 0 or ± 1 for a π- or a $\sigma^{\pm}$-polarized microwave pulse, respectively. Here the contribution of the quadratic Zeeman shift is much less than the linear Zeeman shift and thus is ignored. For a microwave field with a frequency ω, the detuning from the transition $|F=1, m_F\rangle \leftrightarrow |F=2, m_F+k\rangle$ is derived as,

$$\begin{aligned} \Delta_{m_F,m_F+k} &= \omega - \{\omega_0|_{0,0} + [\frac{1}{2}(m_F+k) - (-\frac{1}{2}m_F)]\mu_B B\} \\ &= \Delta - [\frac{1}{2}(m_F+k) - (-\frac{1}{2}m_F)]\mu_B B , \end{aligned} \tag{3.10}$$

where Δ is the detuning from the $|F=1, m_F=0\rangle \leftrightarrow |F=2, m_F=0\rangle$ transition. Similar to Refs. (Gerbier *et al.*, 2006; Leslie, 2008), after substituting this into Eq. 3.8 and suming over the contribution from all possible transitions, the energy shift of $|F=1, m_F\rangle$ is derived as,

$$\begin{aligned}\delta E|_{m_F} &= \frac{h}{4}\sum_{k=0,\pm1}\frac{\Omega^2_{m_F,m_F+k}}{\Delta_{m_F,m_F+k}}\\ &= \frac{h}{4}\sum_{k=0,\pm1}\frac{\Omega^2_{m_F,m_F+k}}{\Delta-[(m_F+k)/2-(-m_F/2)]\mu_B B}\ ,\end{aligned}\tag{3.11}$$

where Ω_{m_F,m_F+k} is the on-resonance Rabi frequency and $\Omega_{m_F,m_F+k}\propto\sqrt{I_k}C_{m_F,m_F+k}$. Here C_{m_F,m_F+k} is the Clebsch-Gordan coefficient of the transition and I_k is the intensity of this purely polarized microwave pulse.

Thus the net quadratic Zeeman shift $q_{\rm net}$ is the sum of q_B and the microwave dressing field induced quadratic Zeeman shift q_M, and is derived as,

$$\begin{aligned}q_{\rm net} &= q_{\rm B}+q_{\rm M}\\ &= aB^2h+\frac{\delta E|_{m_F=1}+\delta E|_{m_F=-1}-2\delta E|_{m_F=0}}{2}\ ,\end{aligned}\tag{3.12}$$

where $a\approx 277$ Hz/G^2 or $a\approx 71.9$ Hz/G^2 for F=1 ^{23}Na or ^{87}Rb atoms, respectively.

3.4 The interaction energy

Interactions especially spin-dependent interactions among atoms in spinor BECs play an important role in the spin-mixing dynamics. For interactions in ^{23}Na or ^{87}Rb BECs, we only take into account the s-wave collisions between two atoms since the three-body loss rate observed in BECs are low. In addition, s-wave collisions with two identical $F=1$ bosonic atoms only give an even value of total spin $F_{\rm pair}$, e.g., $F_{\rm pair}=0$ or $F_{\rm pair}=2$. Therefore, the interaction energy of a pair of atoms located at $\mathbf{r}$ and $\mathbf{r}'$ may be expressed as (Ho, 1998; Ohmi and Machida, 1998),

$$V_{\rm pair}=\sum_{F_{\rm pair}=0,2}\frac{4\pi\hbar^2 a_{F_{\rm pair}}}{M}\delta(\mathbf{r}-\mathbf{r}')\hat{P}_{F_{\rm pair}}\ ,\tag{3.13}$$

where $a_{F_{\text{pair}}}$ is the s-wave collision length in the total spin F_{pair}, M is the mass of an atom, and $\hat{P}_{F_{\text{pair}}}$ is a projection operator which projects a pair of atoms into the spin F_{pair} state. By using the completeness of $\hat{P}_{F_{\text{pair}}}$, we have $\hat{P}_0 + \hat{P}_2 = \hat{I}$, where $\hat{I}$ is the identity operator of the pair of atoms. Similar to Ref. (Stamper-Kurn and Ueda, 2013), the composition law gives,

$$\begin{aligned} F_{\text{pair}}(F_{\text{pair}}+1) &= \hat{\mathbf{F}}^2_{\text{pair}} \\ &= \hat{\mathbf{F}}^2_{\text{atom1}} + \hat{\mathbf{F}}^2_{\text{atom2}} + 2\hat{\mathbf{F}}_{\text{atom1}} \cdot \hat{\mathbf{F}}_{\text{atom2}} \ , \end{aligned} \tag{3.14}$$

where $\hat{\mathbf{F}}_{\text{atom1}}$ and $\hat{\mathbf{F}}_{\text{atom2}}$ are the spin operators for the first and second atoms, respectively. Since $\hat{\mathbf{F}}^2_{\text{atom1}} = \hat{\mathbf{F}}^2_{\text{atom2}} = 2$ for $F = 1$ atoms, we derive,

$$\begin{aligned} \hat{\mathbf{F}}_{\text{atom1}} \cdot \hat{\mathbf{F}}_{\text{atom2}} &= -2\hat{I} + \frac{1}{2} \sum_{F_{\text{pair}}=0,2} F_{\text{pair}}(F_{\text{pair}}+1)\hat{P}_{F_{\text{pair}}} \\ &= -2\hat{I} + 3\hat{P}_2 \ , \end{aligned} \tag{3.15}$$

Together with $\hat{P}_0 + \hat{P}_2 = \hat{I}$, we find that

$$\hat{P}_0 = \frac{1}{3}(\hat{I} - \hat{\mathbf{F}}_{\text{atom1}} \cdot \hat{\mathbf{F}}_{\text{atom2}}) \ , \ \hat{P}_2 = \frac{1}{3}(2\hat{I} + \hat{\mathbf{F}}_{\text{atom1}} \cdot \hat{\mathbf{F}}_{\text{atom2}}) \ . \tag{3.16}$$

Substituting it into Eq. 3.13, we derive,

$$\begin{aligned} V_{\text{pair}} &= \frac{4\pi\hbar^2}{M}\delta(\mathbf{r}-\mathbf{r}')[\frac{a_0}{3}(\hat{I} - \hat{\mathbf{F}}_{\text{atom1}} \cdot \hat{\mathbf{F}}_{\text{atom2}}) + \frac{a_2}{3}(2\hat{I} + \hat{\mathbf{F}}_{\text{atom1}} \cdot \hat{\mathbf{F}}_{\text{atom2}})] \\ &= (c_0\hat{I} + c_2\hat{\mathbf{F}}_{\text{atom1}} \cdot \hat{\mathbf{F}}_{\text{atom2}})\delta(\mathbf{r}-\mathbf{r}') \ , \end{aligned} \tag{3.17}$$

where,

$$c_0 = \frac{4\pi\hbar^2}{M}\frac{a_0+2a_2}{3} \ , \ c_2 = \frac{4\pi\hbar^2}{M}\frac{a_2-a_0}{3} \ . \tag{3.18}$$

The above discussion is applied to a pair of atoms. We extend this discussion into all atoms in BECs, and rewrite Eq. 3.17 in the second-quantized form. The interaction Hamiltonian

Table 3.1: List of the scattering lengths a_0 and a_2 in the unit of Bohr radius a_B. Typical spin independent interaction $c_0 n$ and spin dependent interaction $c = c_2 n$ are also listed in units of h Hz or h kHz and assume a typical spinor gas density of $n = 10^{14}\text{cm}^{-3}$. Values are quoted from Refs. (Knoop *et al.*, 2011; van Kempen *et al.*, 2002; Falke *et al.*, 2008; Lysebo and Veseth, 2010).

Spinor gas	a_0/a_B	a_2/a_B	typical $c_0 n/h$ (see caption)	typical $c = c_2 n/h$ (see caption)
^{23}Na $F = 1$	48.91±0.40	54.54±0.20	1.54 kHz	55 Hz
^{87}Rb $F = 1$	101.8±0.2	100.4±0.1	779 Hz	-3.6 Hz
^{41}K $F = 1$	68.5±0.7	63.5±0.6	1.07 kHz	-27 Hz

may thus be expressed as,

$$\hat{H}_{int} = \frac{1}{2}\int d\mathbf{r}(c_0 : \hat{n}^2 : + c_2 : \hat{\mathbf{F}}^2 :) \ , \tag{3.19}$$

where :: denotes normal ordering indicating creation operators are placed to the left of annihilation operators.

In Eq. 3.19, there are two terms in $\hat{H}_{int}$: the first term is a spin-independent term characterized by c_0, and the second term is a spin-dependent term characterized by c_2. Note that c_2 is proportional to the scattering length difference between $F_{\text{pair}} = 0$ and $F_{\text{pair}} = 2$ atom pairs, and these scattering lengths are constants for each atomic species. Scattering lengths of some atomic species are listed in Table 3.1. Intuitively, when the scattering length is long or the interacting strength is large for one of the F_{pair} states, atoms tend to have a strong repulsion. Therefore, the atoms in the other F_{pair} state tend to have less energy. This result can be confirmed by Eq. 3.17. When $a_2 > a_0$ or $c_2 > 0$, V_{pair} is minimized when $\hat{\mathbf{F}}_{\text{atom1}} \cdot \hat{\mathbf{F}}_{\text{atom2}}$ is minimized. In this state, atoms counter-aligned with each other have less energy. We often denote this type of condensates as "anti-ferromagnetic". In the other case when $a_2 < a_0$, the state in which atoms aligned with each other have less energy. We denote it "ferromagnetic". Note that the word "anti-ferromagnetic" or "ferromagnetic" is different from the antiferromagnet or ferromagnet in solids. There is no lattice structure nor a neighbor.

3.5 The single spatial mode approximation

In BECs, coherent interconversions among atoms in different spin states lead to a macroscopic oscillations of spin state populations. These macroscopic oscillations can be treated by a simple model, the single spatial mode approximation (SMA) (Zhang *et al.*, 2005).

Here, I briefly describe the single spatial mode approximation introduced in Ref. (Zhang *et al.*, 2005). The Hamiltonian used in this approximation is Eqs. 3.1, 3.2 and 3.19. Then a mean field treatment is applied by considering $\Phi_{m_F}(\mathbf{r}) = \langle \hat{\phi}_{m_F}(\mathbf{r}) \rangle$. After that, the single spatial mode approximation (SMA), in which all spin states have the same spatial wavefunction is applied. This is due to the assumption that no spin domains and spatial modes in BECs, and it's consistent with our experimental observations. Therefore, this appears to be a proper theoretical model to understand our data. By applying this approximation, the wavefunction is expressed as,

$$\Phi_{m_F}(\mathbf{r}) = \Psi(\mathbf{r}) \psi_{m_F} \mathrm{e}^{-\frac{iE_{m_F} t}{\hbar}} \ , \tag{3.20}$$

where $\Psi(\mathbf{r})$ represents the spatial mode contribution of the wavefunction, $\int d\mathbf{r} |\Psi(\mathbf{r})|^2 = N$, ψ_{m_F} represents the spin domain contribution, $\sum_{m_F=-1}^{1} |\psi_{m_F}|^2 = 1$, and N is the total number of atoms. Following Ref. (Zhang *et al.*, 2005), we define $\rho_{m_F} = |\psi_{m_F}|^2$. Thus $\rho_{-1} + \rho_0 + \rho_{+1} = 1$ and ψ_{m_F} can be rewrite as $\psi_{m_F} = \sqrt{\rho_{m_F}} \exp(-i\theta_{m_F})$, and the fractional population $\rho_{\mathrm{m_F}}$ and the phase $\theta_{\mathrm{m_F}}$ of each m_F state are independent of position. By applying the wavefunction and Hamiltonian equations, e.g., Eqs. 3.1, 3.2, 3.19 and 3.20 to the Schrödinger equation, the BEC energy E and the time evolution of ρ_0 and θ may thus be expressed as (Stamper-Kurn and Ueda, 2013; Zhang *et al.*, 2005)

$$\begin{aligned} E = {} & q_{\mathrm{net}}(1 - \rho_0) \\ & + c\rho_0[(1 - \rho_0) + \sqrt{(1 - \rho_0)^2 - m^2} \cos\theta] \ , \end{aligned} \tag{3.21}$$

where $\theta = \theta_{+1} + \theta_{-1} - 2\theta_0$ is the relative phase among the three m_{F} spin states, $c = c_2 n$ is the spin-dependent interaction, n is the density of the condensate, and the total magnetization is $m = \rho_{+1} - \rho_{-1}$. Estimated values of c of some typical spinor gases by assume a typical spinor gas density are also listed in Table 3.1.

This energy equation only has two dynamic variables ρ_0 vs θ, thus spin-mixing dynamics in a F=1 spinor BEC may be described by a two-dimensional (ρ_0 vs θ) phase space. Plots of phase diagrams in a few conditions are shown in Fig. 3.3. In addition, if we take into account that the total energy E is conserved within a short time period, the system will thus follows a constant-energy contour line, and the equation of the motion will thus be expressed as,

$$\dot{\rho_0} = -(2/\hbar)\partial E/\partial\theta \ , \quad \dot{\theta} = (2/\hbar)\partial E/\partial\rho_0 \ . \tag{3.22}$$

In some plots of Fig. 3.3, contours are separated by a solid blue line. On one side of this line, contours are limited within $-\pi < \theta < \pi$ region. The system falls in this region should oscillate within a small θ region. This type of solutions are called oscillatory phase solutions. On the other side of this line, contours are not limited by θ, This type of solutions are called running phase solutions. Note that for $q_{\text{net}}/c = 0$ case where the Zeeman term in the Hamiltonian is eliminated, Fig. 3.3 shows only oscillatory phase solutions. For another case, when $q_{\text{net}}/c \leq -2$ or $q_{\text{net}}/c \geq 2$, Eq. 3.3 and Fig. 3.3 show that the contour plots only have running phase solutions resulted from the large contribution from the Zeeman term of Hamiltonian. Only when $-2 < q_{\text{net}}/c < 2$ and $q_{\text{net}}/c \neq 0$, two phases both show up due to the competitions between the Zeeman and interaction terms in Hamiltonian.

The energy contour plots for antiferromagnetic BECs shown in Panel (a) of Fig 3.3 and for ferromagnetic BECs shown in Panel (b) of the same q_{net}/c are exactly flipped. The ground states in antiferromagnetic cases become the highest energy states in ferromagnetic cases, and vise verse. Therefore, the theoretic prediction for the ground states of these two types

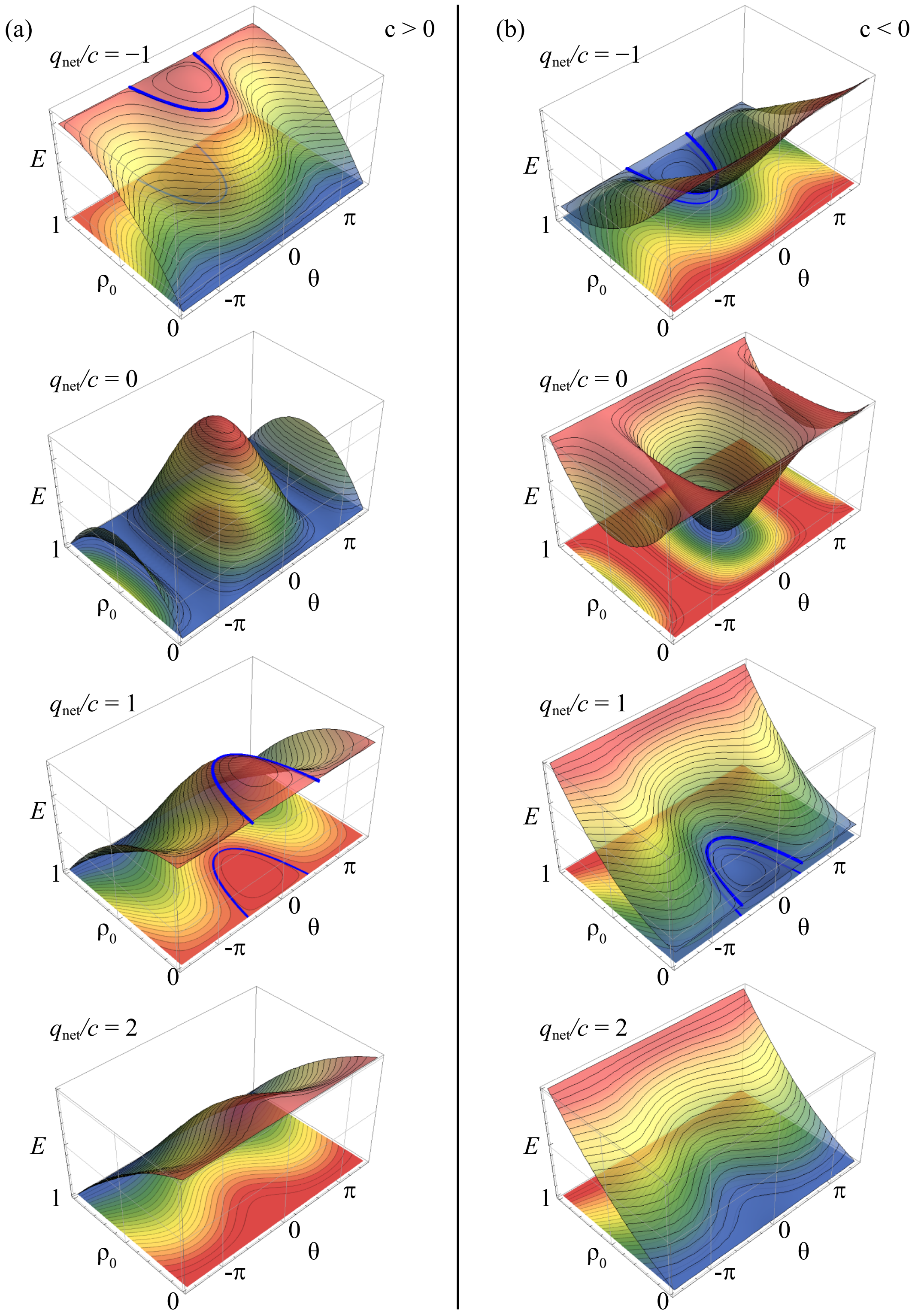

Figure 3.3: 3d plots of energy contours of $F = 1$ antiferromagnetic (a) and ferromagnetic (b) spinor condensates at $m = 0$ with corresponding energy contour plots attached at bottom. Solid blue lines represent the contour lines of the separatrix between the running and oscillatory phase solutions.

of condensates are different. By finding the minimum energy of Eq. 3.21, we derive,

$$\rho_0 = \begin{cases} 1 & m = 0 \textit{ and } q_{\text{net}} > -c(1 \pm 1) \ ; \\ 0 & q_{\text{net}} < c(1 \pm \sqrt{1 - m^2}) \ ; \\ \text{root of } c[1 - 2\rho_0 \pm \frac{(1-2\rho_0)(1-\rho_0)-m^2}{\sqrt{(1-\rho_0)-m^2}}] - q_{\text{net}} = 0 & \text{all other } q_{\text{net}} \text{ and } m, \end{cases} \tag{3.23}$$

where the + or − sign applies to ferromagnetic or antiferromagnetic spinor BECs, respectively. A detail prediction and our experimental results on the ground states are presented in Ref. (Jiang *et al.*, 2014). However, if we consider the energy conservation and only compare a single contour line starting from the same initial ρ_0 and θ, the curve in ρ_0 vs θ phase space are identical. Moreover, the dynamic solution of Eqs. 3.21 and 3.22 in these two cases are also identical. Therefore, theoretically, it brings us an opportunity to resemble the dynamics of one type of atoms by using the other one in a microwave dressing field.

3.6 Experimental setup of microwave dressing field

To create sufficiently large q_{net}, a microwave antenna designed for a frequency near the $|F = 1\rangle \leftrightarrow |F = 2\rangle$ transition is placed a few inches above the center of the optical dipole trap, and connected to a signal amplifier outputting a maximum power of 10 W. The actual power used in this section is ~ 8 W. The commercial antenna ensures low voltage standing wave ratio. As a result, we are able to use a simple design without any protections for power back-reflections. The electronic circuit for generating a microwave field is shown in Fig. 3.4(a). The microwave field signal generator is 8664A from Agilent, Inc. It provides us a very wide frequency range from 100 kHz to 3 GHz of sinusoidal signals. To amplify the signal, a microwave amplifier ZHL-10W-2G+ from Mini-circuits, Inc. is used. This amplifier works between 0.8 GHz to 2 GHz and allows the maximum output power of 10 W. In addition, there is no damage even if this amplifier is connected to an open or short output load under full continuous-wave output power. This feature allows us to not include some protection electric elements in the design. To control microwave dressing fields by

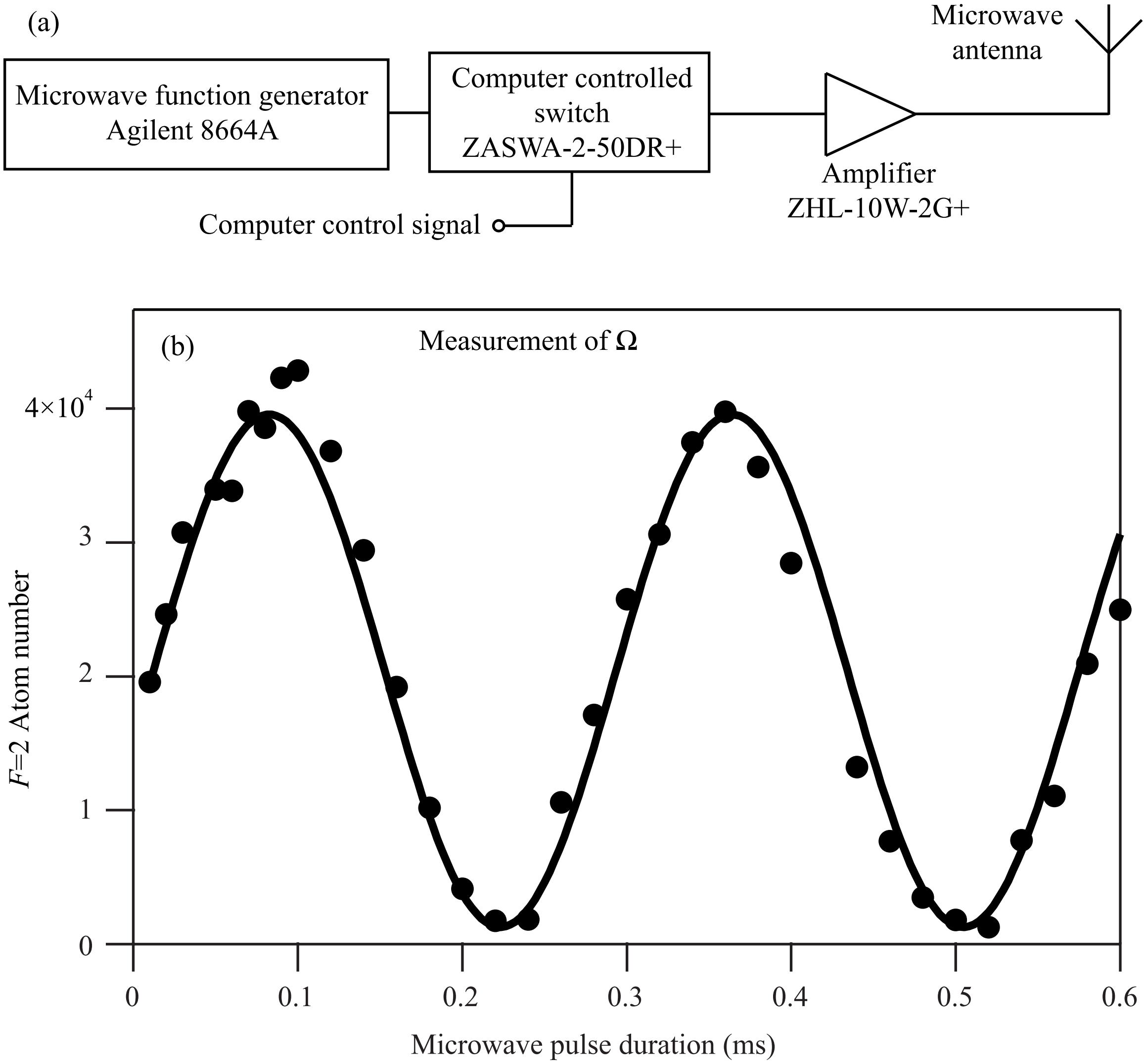

Figure 3.4: (a) Schematic of the circuit for generating microwave dressing fields. (b) The number of $F = 2$ atoms excited by a resonant microwave pulse as a function of the pulse duration. The solid line is a sinusoidal fit to extract the on-resonance Rabi frequency Ω of the pulse.

computer programs, an easy way is to use the build-in GPIB interface of the microwave function generator. However, it usually takes hundreds of milli-seconds to turn on/off through GPIB control signal. To quickly switch on/off the microwave field, there are some different designs, e.g., using amplitude modulation control, or adding a frequency mixers. However, high microwave field leakage is detected for these methods even after we shut them off. In our design, we use a high isolation switch ZASWA-2-50DR+ from Mini-circuits, Inc. controlled by our computer program, as shown in Fig. 3.4(a). When our function generator is set at its maximum output power, the leakage is less than 10^{-4} μW after the switch is shut off. Besides that, this switch turns on or shuts off within 20 ns which is much shorter than our microwave pulse duration and improve experimental resolution.

The exact value of q_{net} is carefully calibrated from a few experimental parameters, such as the polarization and frequency of a microwave pulse. To ensure an accurate calibration of q_{net} based on Eq. 3.12, we measure the nine on-resonance Rabi frequencies Ω daily through monitoring the number of atoms excited by a resonant microwave pulse to the F=2 state as a function of the pulse duration. A typical example of the Rabi frequency measurement is shown in Fig. 3.4(b). We find that uncertainties of Ω and q_{net} are $\sim 2\%$ and $\sim 5\%$, respectively.

A purely π-polarized microwave pulse has been a popular choice in some publications (Leslie *et al.*, 2009b; Stamper-Kurn and Ueda, 2013; Leslie, 2008). However, we apply microwave pulses of a specially-chosen polarization, in order to continuously scan q_{net} from large negative values to big positive values at a moderate microwave power. Figure 3.5 compares microwave dressing fields induced by a typical microwave pulse used in this report and a purely π-polarized microwave pulse. This comparison clearly shows that it is possible to continuously/adiabatically sweep q_{net} from $-\infty$ to $+\infty$ simply by continuously tuning Δ from -190 kHz to 190 kHz with our specially-chosen microwave pulses at a power of 8 W. Another advantage of choosing such microwave pulses is to conveniently place the microwave antenna on our apparatus without blocking optical components.

3.7 Experimental procedures

The process to obtain a pure $F = 1$ sodium BEC fully polarized to the $|F = 1, m_F = -1\rangle$ state is introduced in Chapter II and Ref. (Jiang *et al.*, 2013). After the BEC is prepared, we then ramp up a small magnetic bias field with its strength B being 271.5(4) mG, while turning off the field gradient. An rf-pulse resonant with the linear Zeeman splitting is applied to prepare an initial state with any desired combination of the three m_F states,

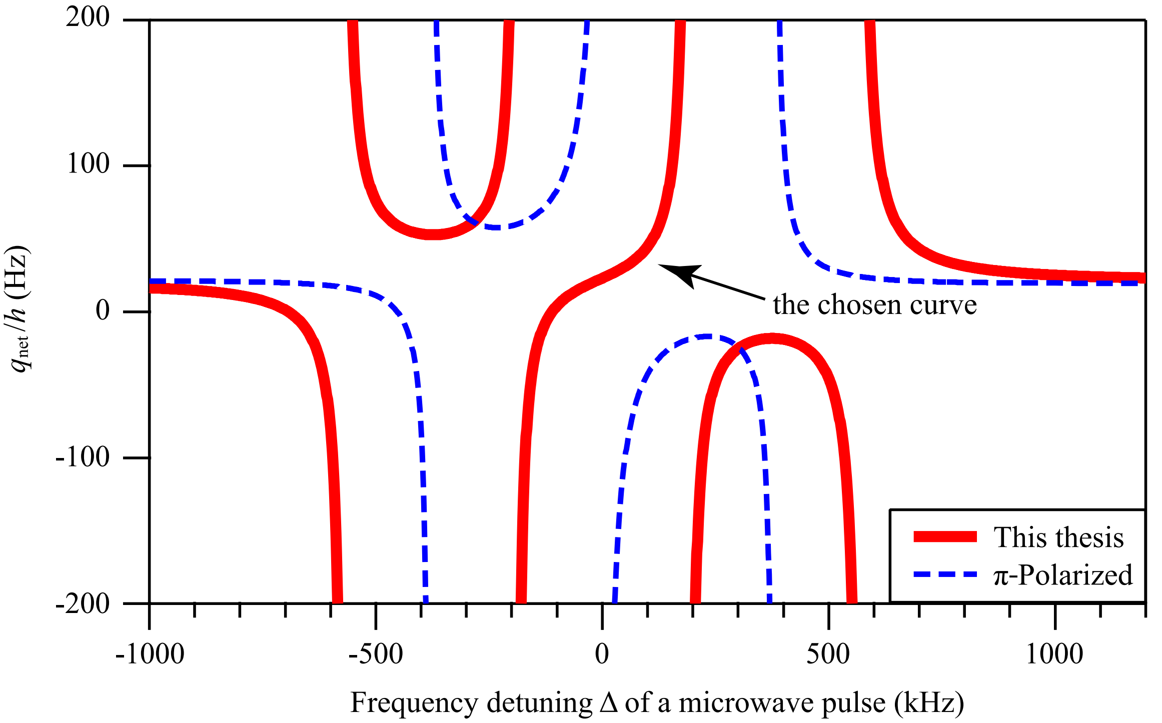

Figure 3.5: q_{net} as a function of Δ. The residual magnetic field is B=271.5(4) mG. Dashed blue lines represent the predictions derived from Eq. 3.12 when the microwave pulse is purely π-polarized and its corresponding on-resonance Rabi frequencies are $\Omega_{-1,-2} = \Omega_{0,-1} = \Omega_{1,0} = \Omega_{-1,0} = \Omega_{0,1} = \Omega_{1,2} = 0$, $\Omega_{-1,-1} = \Omega_{1,1} = 4.2$ kHz, and $\Omega_{0,0} = 4.9$ kHz. Solid red lines represent the predictions from Eq. 3.12 for a typical microwave pulse used in this report. The specially-chosen polarization of this pulse yields nine on-resonance Rabi frequencies: $\Omega_{-1,-2} = 5.1$ kHz, $\Omega_{0,-1} = 3.6$ kHz, and $\Omega_{1,0} = 2.1$ kHz are from the σ^--polarized component of the pulse; $\Omega_{-1,-1} = \Omega_{0,0} = \Omega_{1,1} = 0$ are from the π-polarized component of the pulse; and $\Omega_{-1,0} = 2.3$ kHz, $\Omega_{0,1} = 3.9$ kHz, and $\Omega_{1,2} = 5.5$ kHz are from the σ^+-polarized component of the pulse (see text). In this report, Δ is tuned within the range of -190 kHz to 190 kHz from the $|F = 1, m_F = 0\rangle \leftrightarrow |F = 2, m_F = 0\rangle$ transition.

which is followed by abruptly switching on an off-resonant microwave pulse to generate a proper microwave dressing field. After various hold time t in the optical dipole trap, the microwave dressing fields are quickly turned off. Populations of the multiple spin states are then measured via the standard absorption imaging preceded by a 3 ms Stern-Gerlach separation and a 7 ms time of flight.

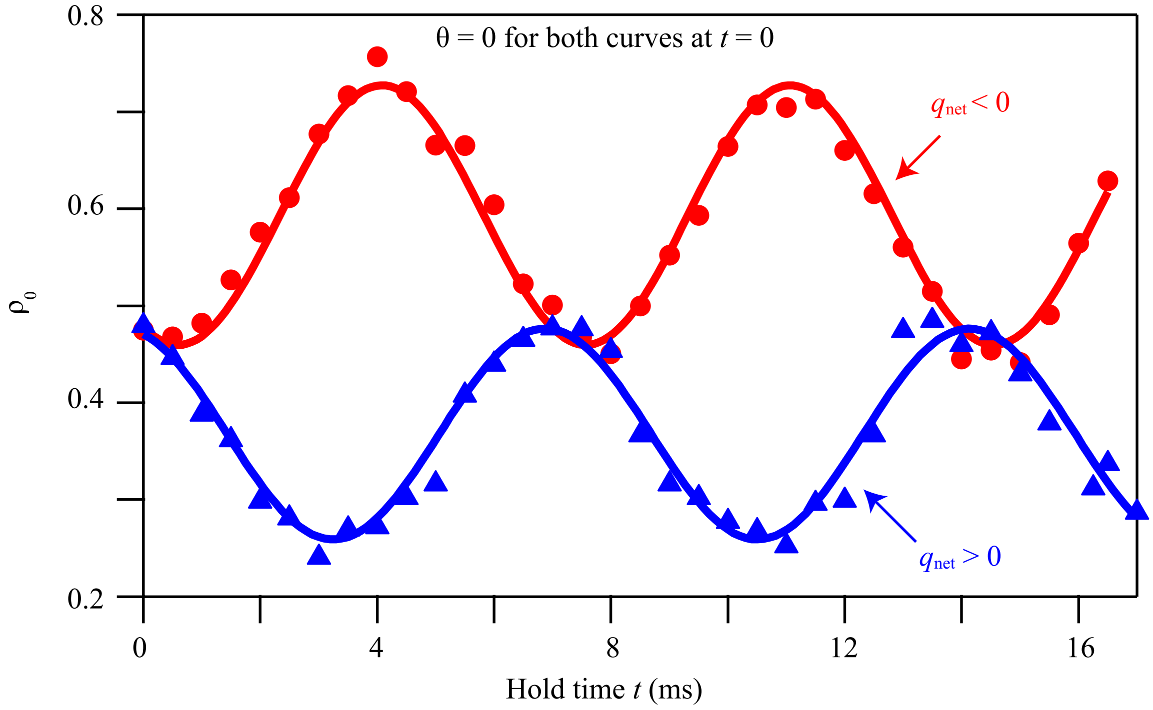

Figure 3.6: Time evolutions of ρ_0 at $q_{\text{net}}/h = +93$ Hz > 0 (solid blue triangles) and $q_{\text{net}}/h = -83$ Hz < 0 (solid red circles) with $m = 0$ and $c/h = 52(1)$ Hz. It is important to note that the two curves start from the same initial state with $\theta|_{t=0} = 0$. Solid lines are sinusoidal fits to the data.

3.8 Dynamics of spinor condensates in a microwave dressing field

We observe spin oscillations at every given value of q_{net} within a wide range, i.e., -240 Hz $\leq q_{\text{net}}/h \leq 240$ Hz. Typical time evolutions of ρ_0 starting with the same nonequilibrium initial state at a negative and a positive q_{net} are shown in Fig. 3.6. We find that these evolutions can be well fit by sinusoidal functions of the similar oscillation period T and amplitude A. Note that the hold time t is kept between zero and $2T < 100$ ms, in order to ensure accurate measurements of spin dynamics and avoid significant atom losses due to the presence of off-resonant microwave pulses. On the other hand, our data in Fig. 3.6 shows that the value of $\langle\rho_0\rangle$ is drastically different in the two spin oscillations: $\langle\rho_0\rangle > \rho_0|_{t=0}$ as long as $q_{\text{net}} < 0$, while $\langle\rho_0\rangle < \rho_0|_{t=0}$ if $q_{\text{net}} > 0$. Here $\langle\rho_0\rangle$ is the average value of ρ_0 over time in a spin oscillation and $\rho_0|_{t=0}$ is the initial value of ρ_0. This phenomenon is observed

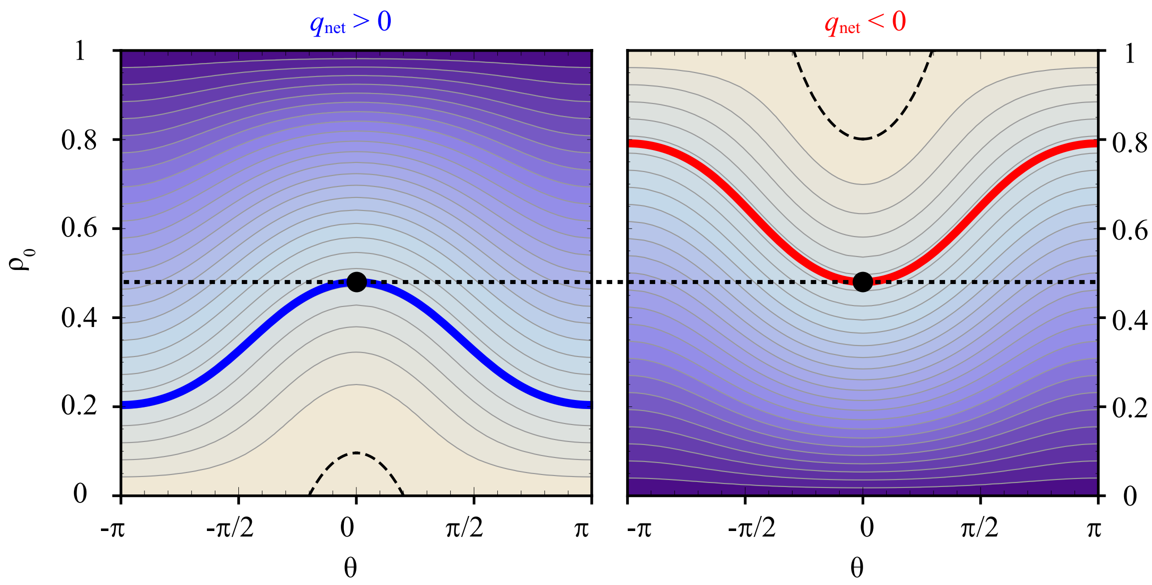

Figure 3.7: Equal-energy contour plots based on Eq. 3.21 for the two experimental conditions shown in Fig. 3.6, i.e., $q_{\mathrm{net}} > 0$ (left) and $q_{\mathrm{net}} < 0$ (right). The heavy solid blue and red lines represent the energy of the above two experimental conditions, respectively. The dotted black horizontal line is to emphasize the fact that the above two experiments start with the same initial state which is marked by the solid black circles. Dashed black lines represent the energy of the separatrix between the running and oscillatory phase solutions. Darker colors correspond to lower energies.

at every value of q_{net} when spin oscillations start with the same initial state, although the period T and amplitude A change with q_{net}. The above observations agree well with predictions from the mean-field SMA theory (i.e., Eq. 3.21) as shown by the heavy solid lines in Figs. 3.7 and 3.8: ρ_0 is limited between $(\rho_0|_{t=0} - 2A)$ and $\rho_0|_{t=0}$ at $q_{\mathrm{net}} > 0$, while it is restricted between $\rho_0|_{t=0}$ and $(\rho_0|_{t=0} + 2A)$ at $q_{\mathrm{net}} < 0$. We can thus use the phenomenon to conveniently determine the sign of q_{net}, i.e., by comparing the value of $\langle \rho_0 \rangle$ of a spin oscillation to the value of $\rho_0|_{t=0}$.

The value of T as a function of q_{net} is then plotted in Fig. 3.9 for $m = 0$ and $m = 0.2$, which demonstrates two interesting results. First, when $m = 0$, the spin oscillation is harmonic except near the critical values (i.e., $q_{\mathrm{net}}/h = \pm\, 52$ Hz) where the period diverges. This agrees with the predictions derived from Eq. 3.21, as shown by the dotted red line in Fig. 3.9. The energy contour E_{sep} where the oscillation becomes anharmonic is defined as a separatrix in phase space. A point on the separatrix satisfies the equation $\dot{\rho}_0 = \dot{\theta} = 0$ according to the

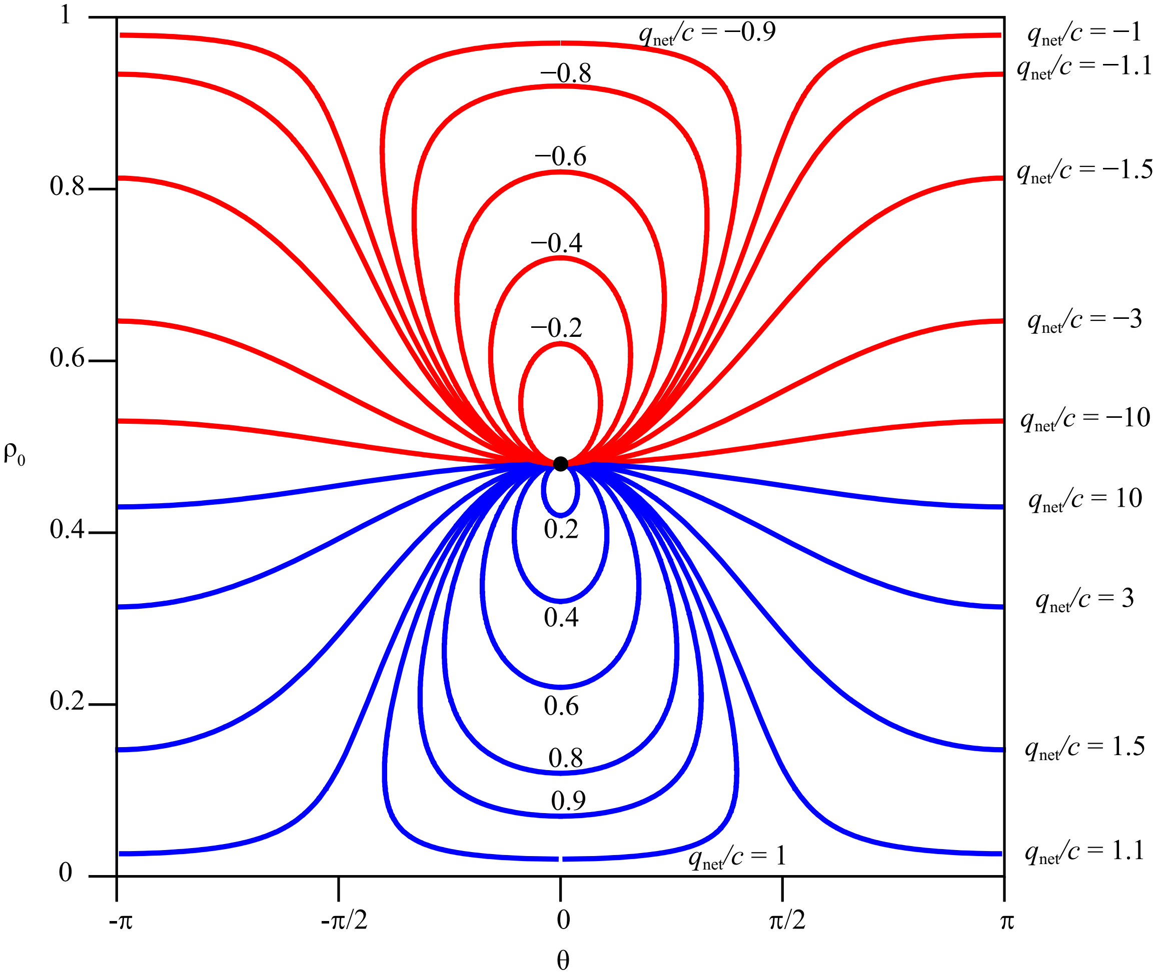

Figure 3.8: Equal-energy contour plots based on Eq. 3.21 starting from a same initial experimental condition. The black dot is the initial experimental condition, i.e., $\rho_0|_{t=0} = 0.48$, $\theta|_{t=0} = 0$. The solid blue and red lines represent equal-energy lines from the same starting point at several typical positive and negative $q_{\rm net}/c$, respectively. $q_{\rm net}/c$ value of each curve is marked on the figure.

mean-field SMA theory. In fact for our sodium system with $c > 0$, $E_{\rm sep} = q_{\rm net}$ for $q_{\rm net} > 0$, while $E_{\rm sep} = 0$ at $m = 0$ for $q_{\rm net} < 0$. Figure 3.9 shows that the T versus $q_{\rm net}$ curve is symmetric with respect to the $q_{\rm net} = 0$ axis at $m = 0$. The period T decreases rapidly with increasing $|q_{\rm net}|$ when $|q_{\rm net}|$ is large, which corresponds to the "Zeeman regime" with running phase solutions. In the opposite limit, the period only weakly depends on $|q_{\rm net}|$, which represents the "interaction regime" with oscillatory phase solutions. Here $|q_{\rm net}|$ is the absolute value of $q_{\rm net}$. The value of θ is (or is not) restricted in the regions with oscillatory (or running) phase solutions. Refs (Black *et al.*, 2007; Liu *et al.*, 2009b) reported

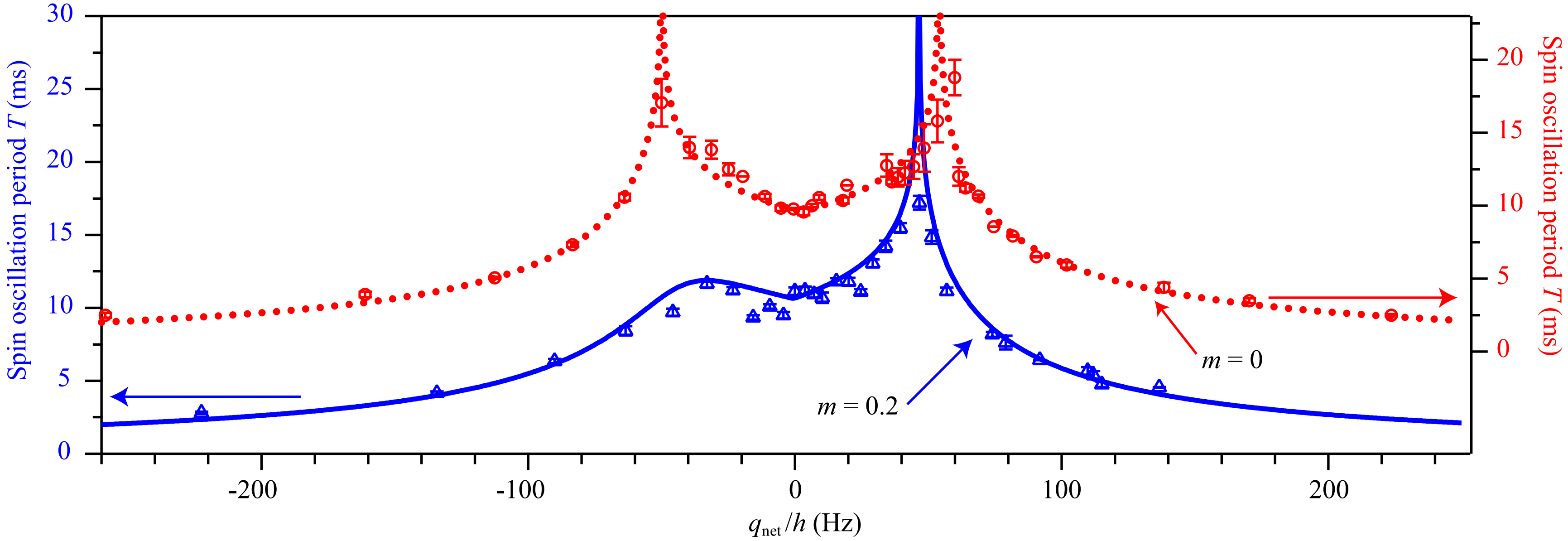

Figure 3.9: The spin oscillation period as a function of q_{net} for $m = 0$ (open red circles) and $m = 0.2$ (open blue triangles). The lines are fits based on Eq. 3.21, which yield the fit parameters: $\rho_0|_{t=0} = 0.48$, $\theta|_{t=0} = 0$, and $c/h = 52(1)$ Hz for $m = 0$; and $\rho_0|_{t=0} = 0.48$, $\theta|_{t=0} = 0$, and $c/h = 47(1)$ Hz for$m = 0.2$. The fit parameters are within the 5% uncertainty of our measurements. Note the different scales of the left and right vertical axes.

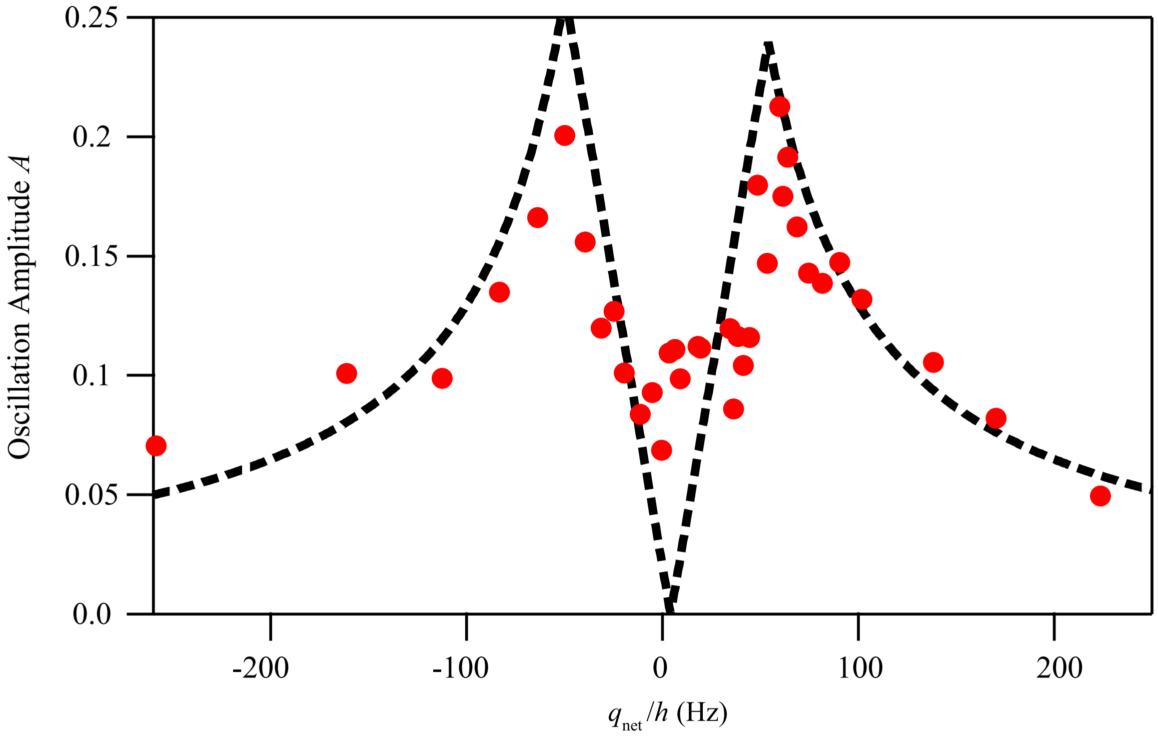

Figure 3.10: Amplitudes A of spin oscillations shown in Fig. 3.9 as a function of q_{net} at $m = 0$. The dashed black line is a fit based on Eq. 3.21 with the same set of fit parameters as that applied in Fig. 3.9.

observations of the similar phenomena for $q_{\text{net}} > 0$ with a F=1 antiferromagnetic spinor condensate, however, they did not access the negative q_{net} region.

Figure 3.9 also demonstrates a remarkably different relationship between the total magnetization m and the separatrix in phase space: the position of the separatrix moves slightly with m in the positive q_{net} region, while the separatrix quickly disappears when m is away from zero in the negative q_{net} region. Good agreements between our data and the mean-field SMA theory are shown in Figs. 3.9 and 3.10. Interestingly, we find that the spin dynamics which appear in our antiferromagnetic sodium system in the negative q_{net} region exactly resembles what is predicted to occur in a ferromagnetic spinor condensate in the positive q_{net} region (Lamacraft, 2011; Zhang *et al.*, 2005). Note that $R = q_{\text{net}}/c$ is negative in both of these two cases. This observation agrees with an important prediction made by Ref. (Lamacraft, 2011): the spin-mixing dynamics in F=1 spinor condensates substantially depends on the sign of R. As a matter of fact, our results in the negative q_{net} region are similar to those reported with a $F{=}1$ ferromagnetic ^{87}Rb spinor condensate in magnetic fields where $q_{\rm net} > 0$ (Chang *et al.*, 2005a; Stamper-Kurn and Ueda, 2013). It is worth noting that our data in Figs. 3.9 and 3.10 may also be extrapolated to understand the relationship between the separatrix and m in the ferromagnetic Rb system, although this relationship has not been experimentally explored yet. We may thus be the first to use only one atomic species to reveal mean-field spin dynamics, especially the different relationship between each separatrix and the magnetization, of $F{=}1$ antiferromagnetic and ferromagnetic spinor condensates.

In conclusion, we have experimentally studied spin dynamics of a sodium spinor condensate in a microwave dressing field. In both negative and positive $q_{\rm net}$ regions, we have observed harmonic spin oscillations and found that the sign of $q_{\rm net}$ can be determined by comparing $\langle\rho_0\rangle$ to $\rho_0|_{t=0}$. Our data also demonstrates that the position of the separatrix in phase space moves slightly with m in the positive $q_{\rm net}$ region, while the separatrix quickly disappears when m is away from zero in the negative $q_{\rm net}$ region. Our data can be well fit by the mean-field theory and agrees with one of its important predictions: the spin-mixing dynamics in $F{=}1$ spinor condensates substantially depends on the sign of $R = q_{\rm net}/c$. This work may be the first to use only one atomic species to reveal mean-field spin dynamics and the different dependence of each separatrix on m in $F{=}1$ antiferromagnetic and ferromagnetic spinor condensates. In addition, microwave pulses used in this report can be applied to cancel out stray magnetic fields and adiabatically sweep $q_{\rm net}$ from $-\infty$ to $+\infty$.

CHAPTER IV

ANTIFERROMAGNETIC SPINOR CONDENSATES IN A TWO-DIMENSIONAL OPTICAL LATTICE

This chapter discusses our experimental results on antiferromagnetic spinor condensates confined by a two-dimensional optical lattice. One paper related to this topic was published:

- L. Zhao, J. Jiang, T. Tang, M. Webb, and Y. Liu, *Antiferromagnetic spinor condensates in a two-dimensional optical lattice*, Phys. Rev. Lett. **114**, 225302 (2015). Included in Appendix C.

In this Chapter, we experimentally demonstrate that a two-dimensional (2d) optical lattice can conveniently tune spin dynamics of F=1 antiferromagnetic spinor BECs. We find that the properties of spinor BECs remain largely unchanged in the presence of a shallow lattice, while sufficiently deep lattices introduce some interesting changes. First, in every lattice depth u_L that supports a substantial superfluid fraction, we observe spin population oscillations after taking spinor BECs out of equilibrium at a fixed q_B. Second, we demonstrate a lattice-tuned separatrix in phase space, and explain it using lattice-enhanced spin-dependent interactions. Another remarkable result is our observation of a phase transition from a longitudinal polar (LP) phase to a broken-axisymmetry (BA) phase in steady states of spinor BECs confined by sufficiently deep lattices. We find the steady states depend exponentially on q_B and sigmoidally on u_L, which agrees with our phenomenological model.

I will first review some basic theories related to optical lattices and the Bose-Hubbard model for spinor BECs.

4.1 Optical lattice

An optical dipole trap (ODT) has been a useful technique in lots of experiments. Comparing to magnetic traps, ODTs allow us to simultaneously confine multiple spin components and study the properties of spinor BECs within a wide range of external magnetic fields. By interfering two or more ODT teams, optical standing waves or optical lattices can be formed. Similar to the derivation of the AC Stark shift induced by microwave dressing fields in Chapter III, we can write the potential created by a lattice beam having the intensity $I(\mathbf{r})$ as,

$$V(\mathbf{r}) = \frac{3\pi c^3 \hbar\Gamma}{2\omega_R^2 \Delta} I(\mathbf{r}) \ , \tag{4.1}$$

where Γ is the nature linewidth, δ is the frequency detuned from the resonance, and ω_R is the resonance frequency of the transition. There are several ways to form an optical lattice. The most easiest way is to retro-reflect one ODT beam. In this situation, we can assume the lattice beams are Gaussian beams at a wavelength of λ_L along the z-axis, and express the potential created by these beams as,

$$V_{lat}(r,z) = 4V_s \cos^2\left(\frac{2\pi z}{\lambda_L}\right)\left[1 - 2\left(\frac{r}{\omega_0}\right)^2 - \left(\frac{z}{z_R}\right)^2\right] \ , \tag{4.2}$$

where we define,

$$V_s = \frac{3\pi c^3 \hbar\Gamma}{2\omega_R^2 \Delta}\frac{2P}{\pi\omega_0^2} \ , \tag{4.3}$$

is the peak potential of a single lattice beam and the Gaussian beam profile is described as,

$$I(r,z) = \frac{2P}{\pi\omega_0^2}\left[1 - 2\left(\frac{r}{\omega_0}\right)^2 - \left(\frac{z}{z_R}\right)^2\right] + \mathcal{O}\left[\left(\frac{r}{\omega)_0}\right)^3\right] + \mathcal{O}\left[\left(\frac{z}{z_R}\right)^3\right] \ . \tag{4.4}$$

Here, P is the power of the lattice beam, ω_0 is the Gaussian beam waist at its focus point, and $z_R = \pi\omega_R^2/\lambda_L$ is the Rayleigh length. Equation 4.2 implies a periodic potential with a period of $\lambda_L/2$. By changing the angle between these two lattice beams, one can increase the lattice spacing. Therefore, I'll limit my discussion to the retro-reflect lattice beam setup, since all lattice beams in our system are retro-reflected.

A one-dimensional lattice is constructed by one pair of lattice beams. They create a 2D pancake structure with each lattice site being a quasi two-dimensional disk. A two-dimensional lattice can be constructed by two pairs of lattice beams, which results in a structure with quasi one-dimensional tubes. By using three pairs of beams, quasi zero-dimensional dots are constructed in each lattice site. Near the center of optical lattices, the potential may be approximated as a sum of a fast sinusoidal oscillating potential and a slow varying harmonic potential. Here, we will first consider the fast oscillating potential and express it as,

$$V_{lat}(\mathbf{x}) = u_L E_R \sum_{\alpha} \frac{1}{2}[1 + \cos(2k_L x_\alpha)] \ , \tag{4.5}$$

where $u_L = 4V_s/E_R$ is the dimensionless lattice depth, α sum over all dimensions with lattice beams, $E_R = \hbar^2 k_L^2/(2M)$ is the recoil energy, and $k_L = 2\pi/\lambda_L$. The lattice trap frequency at the bottom of each lattice site may thus be expressed as,

$$\begin{aligned} \omega_{lat} &= \sqrt{\frac{2\hbar^2 k_L^2}{M} u_L E_R} \\ &= 2E_R\sqrt{u_L} \ . \end{aligned} \tag{4.6}$$

4.2 Band structure

We apply the periodic potential into the Hamiltonian based on the Bloch theorem (Bloch, 1929). The solution of the Schrödinger equation should obey the form:

$$\Psi_{n\mathbf{k}}(\mathbf{r}) = \mathrm{e}^{i\mathbf{k}\cdot\mathbf{r}} u_{n\mathbf{k}}(\mathbf{r}) \ , \tag{4.7}$$

where $\mathbf{k}$ is the quasi momentum, n is the band index, and $u_{n\mathbf{k}}(\mathbf{r})$ is a periodic function with the same periodicity as V_{lat}. Here, since $u_{n\mathbf{k}}(\mathbf{r})$ is a periodic function of $\mathbf{k}$, $\mathbf{k}$ is thus only defined within one period. A conventional selection is to define $\mathbf{k}$ within the first Bouillon zone. Similar to Chapter III, we use the single spatial mode approximation, and then express the wave function as follows,

$$\Psi_{n\mathbf{k},m_F}(\mathbf{r}) = \mathrm{e}^{i\mathbf{k}\cdot\mathbf{r}} u_{n\mathbf{k}}(\mathbf{r})\psi_{m_F}\mathrm{e}^{-\frac{iE_{m_F}t}{\hbar}} \ , \tag{4.8}$$

where ψ_{m_F} represents the spin domain contribution similar to Chapter III.

There are lots of theories developed in solid state physics to approximately solve this type of wave functions and to find band structures of the crystal structures. Here, I only consider the wave function along one dimension and ignore all the interaction H_{int} terms, which highly simplify the problem. Under this consideration, we can express u_{nk} in a Fourier expansion,

$$u_{nk}(r) = \frac{1}{\sqrt{2\pi}} \sum_{j=-\infty}^{\infty} c_{j,nk}\mathrm{e}^{-ijk_L r} \ , \tag{4.9}$$

which allows us to rewrite the the Schrödinger equation as,

$$\sum_{j'=-\infty}^{\infty} H_{j,j'}c_{j',nk} = E_{nk}c_{j,nk} \tag{4.10}$$

where

$$H_{j,j'} = \begin{cases} [(2j + k/k_L)^2 + u_L/2]E_R + H_Z \ , & \text{if} j = j' \ ; \\ -u_L E_R/4 \ , & \text{if} |j - j'| = 1 \ ; \\ 0 \ , & \text{if} |j - j'| > 1 \ . \end{cases} \tag{4.11}$$

To numerically solve the Hamiltonian, the contributions of the higher bands may be ignored. A good solution can be found by only limit j and j' between -20 and 20, which means the calculation only use the lowest 20 plane waves. Note that H_Z is the Zeeman term and independent of r or k. Figure 4.1 shows band structures at $u_L = 5E_R$, $10E_R$ and $15E_R$. As u_L increases, energy bands, especially the lowest energy band in the band structure flattens out, and energy gaps among bands increase. The relation of energy and quasi-momentum in the lowest band is referred as the dissipation relation $T(\mathbf{k}, m_F)$. Figure 4.1 also shows that the $|F = 1, m_F = \pm 1\rangle$ curve lies slightly above the $|F = 1, m_F = 0\rangle$ curve at a large q_B due to the contribution of the quadratic Zeeman energy.

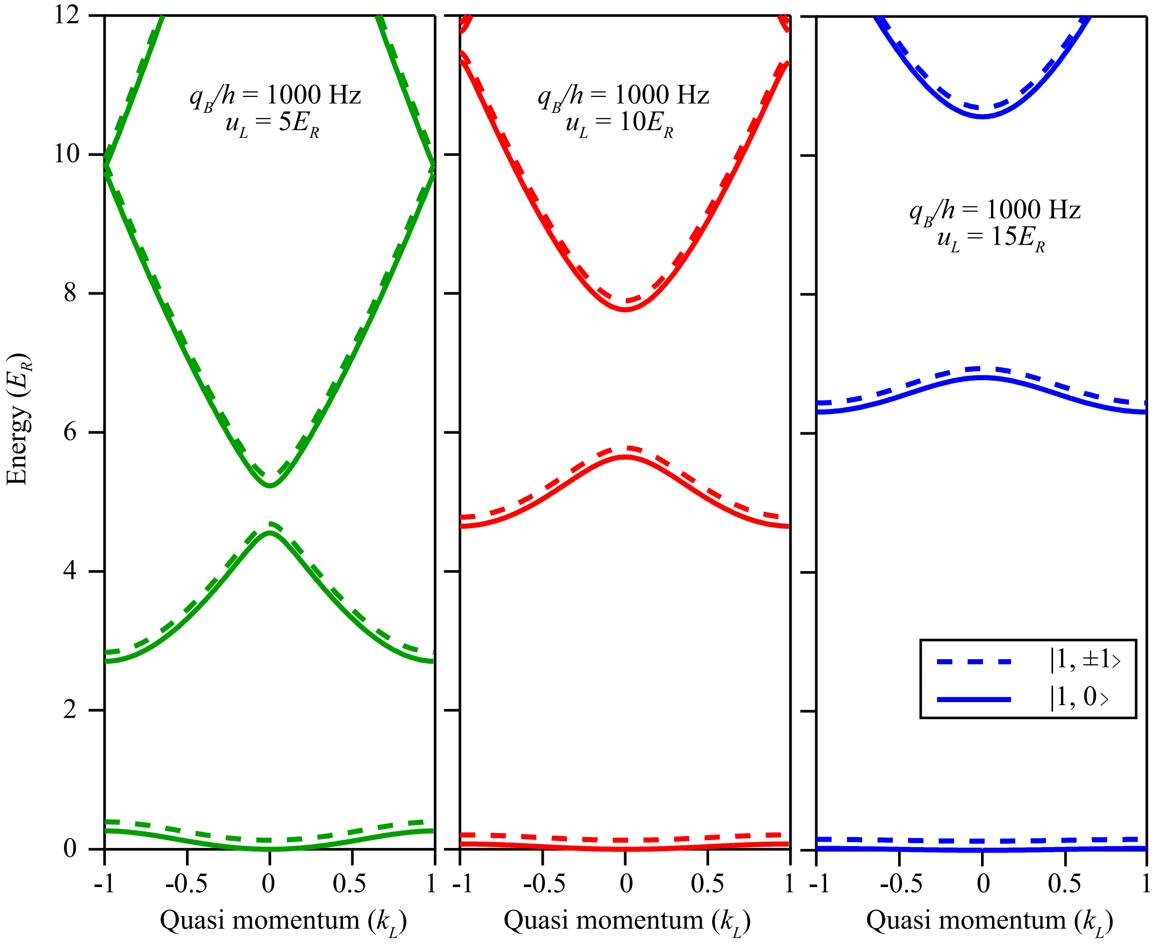

Figure 4.1: Band structures of ultracold atoms in a 1D optical lattice at $u_L = 5E_R$ (left panel), $u_L = 10E_R$ (middle panel), and $u_L = 15E_R$ (right panel). Solid and dashed lines represent the results of the $m_F = 0$ and $m_F = \pm 1$ states, respectively. q_B/h is assumed to be 1000 Hz.

In the above model, the interaction between atoms are completely ignored. Therefore, this approximation have some limitations. In the next section, a model including these interactions is briefly reviewed.

4.3 Bose-Hubbard model

The Bose-Hubbard model is closely related to the Hubbard model, which was introduced in solid state physics by John Hubbard in 1963 to solve the motion of electrons in crystalline solid (Hubbard, 1963). This model is then be generalized to bosons (Gersch and Knollman, 1963), and therefore, the generalized model is called Bose-Hubbard model. After a milestone experimental work on confining BECs in optical lattices in 2002, the Bose-Hubbard model has been widely used to understand bosonic gases in optical lattices (Markus Greiner and Bloch, 2002).

In contrast to the approximation used in Section 4.2, the Bose-Hubbard model takes inter-atomic interactions into account. It starts from the Hamiltonian given in Eqs. 3.1, 3.2 and 3.19. In a deep lattice, the tunneling rate among lattice sites becomes smaller and the wave function is localized near the lattice site. Under this expectation, the wave function may be expressed in terms of a set of Wannier functions,

$$u_{n\mathbf{k}}(\mathbf{r}) = \frac{1}{\sqrt{v_B}} \sum_{\mathbf{R}} w_n(\mathbf{r}-\mathbf{R}) \mathrm{e}^{i\mathbf{k}\cdot\mathbf{R}} \ , \tag{4.12}$$

where $\mathbf{R} = \sum_\alpha n_\alpha \mathbf{a}_\alpha$ is the position of each lattice site, and $\mathbf{a}_\alpha$ is the unit lattice vector in α-axis. Therefore, an inverse Fourier transform gives the Wannier function,

$$w_n(\mathbf{r}-\mathbf{R})(\mathbf{r}) = \frac{1}{\sqrt{v_B}} \int d\mathbf{k} u_{n\mathbf{k}}(\mathbf{r}) \mathrm{e}^{-i\mathbf{k}\cdot\mathbf{R}} \ , \tag{4.13}$$

where v_B is the volume of the first Brillouin zone. If we consider cold atom gases in deep lattices where atoms could remain in the lowest energy band, the field operator may be expressed as $\hat{\phi}_{m_F}(\mathbf{r}) = \sum_i \hat{a}_{im_F} w_0(\mathbf{r}-\mathbf{R}_i)$, where i denotes the ith lattice site, and $\mathbf{R}_i$ is the position of ith lattice site. After substituting this equation into Eqs. 3.1, 3.2 and 3.19, we derive the Hamiltonian of Bose-Hubbard model as follows,

$$\begin{aligned} \hat{H} = & - J \sum_{<i,j>,m_F} \hat{a}^\dagger_{im_F} \hat{a}_{jm_F} + \frac{U_0}{2} \sum_i \hat{n}_i(\hat{n}_i - 1) + \frac{U_2}{2} \sum_{i\gamma ll'nn'} \hat{a}^\dagger_{il} \hat{a}^\dagger_{in} (f_\gamma)_{n,n'} (f_\gamma)_{l,l'} \hat{a}_{in'} \hat{a}_{il'} \\ & + q_{\text{net}} \sum_{i,m_F} m_F^2 \hat{n}_{im_F} - \mu \sum_i \hat{n}_i - \mu_m \sum_{i,m_F} \hat{m}_F n_{i,m_F} \ , \end{aligned} \tag{4.14}$$

where $J = \int d\mathbf{r} w_0^*(\mathbf{r}-\mathbf{R}_i)[-\frac{\hbar^2}{2M}\nabla^2 + V_{lat}(\mathbf{r})] w_0(\mathbf{r}-\mathbf{R}_i)$ is the hopping energy with i and j are nearest neighbor sites, $U_0 = c_0 \int d\mathbf{r} |w_0(\mathbf{r})|^4$ is the spin-independent on-site interaction energy, $U_2 = c_2 \int d\mathbf{r} |w_0(\mathbf{r})|^4$ is the spin-dependent interaction energy, $\mu_m = p_{\text{net}}$ is the linear

Table 4.1: List of scattering lengths a_0 and a_2 in the unit of Bohr radius a_B and the ratio between spin-dependent and spin-independent interaction energy U_2/U_0. Values are cited from Refs. (Knoop *et al.*, 2011; van Kempen *et al.*, 2002; Falke *et al.*, 2008; Lysebo and Veseth, 2010).

Spinor gas	a_0/a_B	a_2/a_B	U_2/U_0
^{23}Na $F = 1$	48.91±0.40	54.54±0.20	0.036
^{87}Rb $F = 1$	101.8±0.2	100.4±0.1	-0.0046
^{41}K $F = 1$	68.5±0.7	63.5±0.6	-0.026

Zeeman energy, $\hat{n}_{i,m_F} = \hat{a}^{\dagger}_{im_F}\hat{a}_{im_F}$, and $\hat{n}_i = \sum_{m_F} \hat{n}_{i,m_F}$.

From the expression of U_0 and U_2, it's easy to notice that the ratio between them is fixed, i.e.,

$$\frac{U_2}{U_0} = \frac{c_2}{c_0} = \frac{a_2 - a_0}{a_0 + 2a_2} \ , \tag{4.15}$$

for each spinor gas. Table 4.1 lists this ratio for several typical spinor gases. In this thesis, I only keep one significant digit and use $U_2 = 0.04U_0$ for sodium atoms.

By ignoring interatomic interactions (U_0 and U_2 terms) and by limiting the calculation

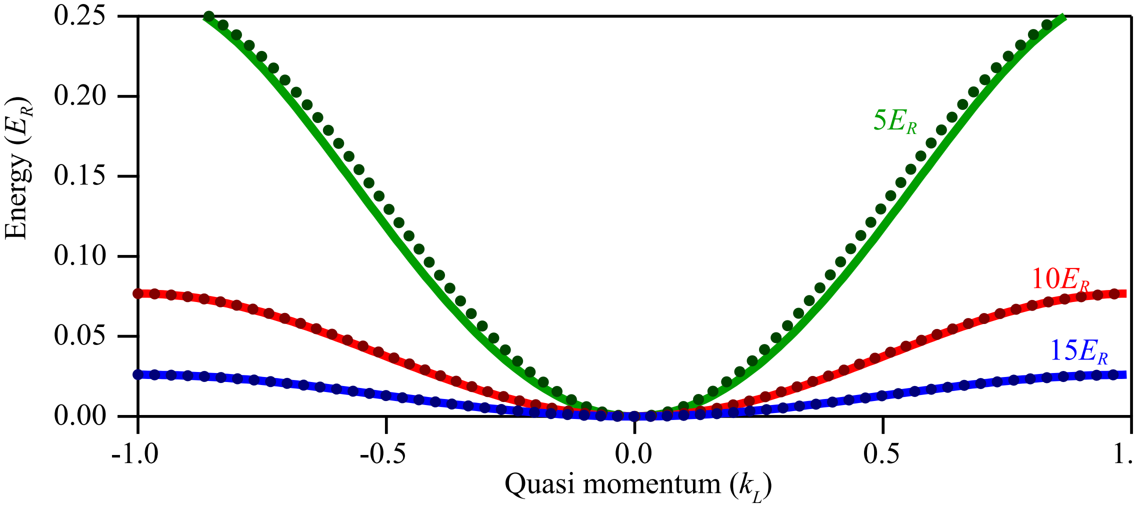

Figure 4.2: Dispersion relations of $m_F = 0$ atoms at $u_L = 5Er$ (green lines), $u_L = 10Er$ (red lines) and $u_L = 15Er$ (blue lines). Lighter solid lines are predicted by Bloch theorem (see Section 4.2). Darker dotted lines are predicted by the non-interacting Bose-Hubbard model (see Section 4.3).

inside a deep lattice, we may express $\hat{a}_{im_F}$ in a Fourier series as follows,

$$\hat{a}_{im_F} = \frac{1}{\sqrt{N_{site}}} \sum_{\mathbf{k}} \hat{b}_{\mathbf{k}m_F} \mathrm{e}^{i\mathbf{k}\cdot\mathbf{R}_i} \ , \tag{4.16}$$

where N_{site} is the total number of lattice sites. We then substitute this expression (Eq. 4.16) into $H_{\text{non-int}}$, the Hamiltonian without the interatomic interactions. Then, after a diagonalization, we can express $H_{\text{non-int}}$ as follows

$$\hat{H}_{\text{non-int}} = \sum_{\mathbf{k}} E_{\mathbf{k}m_F} \hat{b}^{\dagger}_{\mathbf{k}m_F} \hat{b}_{\mathbf{k}m_F} \ , \tag{4.17}$$

where

$$E_{\mathbf{k}m_F} = 4J \sum_{\alpha} \sin^2(\frac{1}{2}\mathbf{k}\cdot\mathbf{a}_{\alpha}) + q_{\text{net}} m_F^2 - \mu - \mu_m m_F \tag{4.18}$$

is the dispersion relation under this approximation.

Note that this dispersion relation derived from the Bose-Hubbard model, i.e., Eq. 4.18, only considers the hopping between nearest neighbors. It works well when next nearest neighbors or farther sites have a negligible hopping rate in deep lattices. A comparison between this approximation and the one derived from Bloch theorem reviewed in the last section is shown in Fig. 4.2. Agreements between these two approximations shown in this figure may be a justification of this model.

4.4 Experimental procedures

The procedure of BEC production and purification into the $|F = 1, m_F = -1\rangle$ state in a crossed optical trap was introduced in Chapter II and Ref. (Jiang *et al.*, 2013). To adiabatically load the BEC into a 2d lattice, we decompress the optical trap to a value which minimizes intra-band excitations and ensures approximately constant Thomas-Fermi radii while linearly ramping the lattice potential within $t_{\text{ramp}} > 40$ ms. We construct the 2d lattice in the $\hat{x}$-$\hat{y}$ horizontal plane using two linearly-polarized beams which originate from a single-mode laser at $\lambda_L = 1064$ nm, have a waist of $\sim$90 μm at the condensate, and are

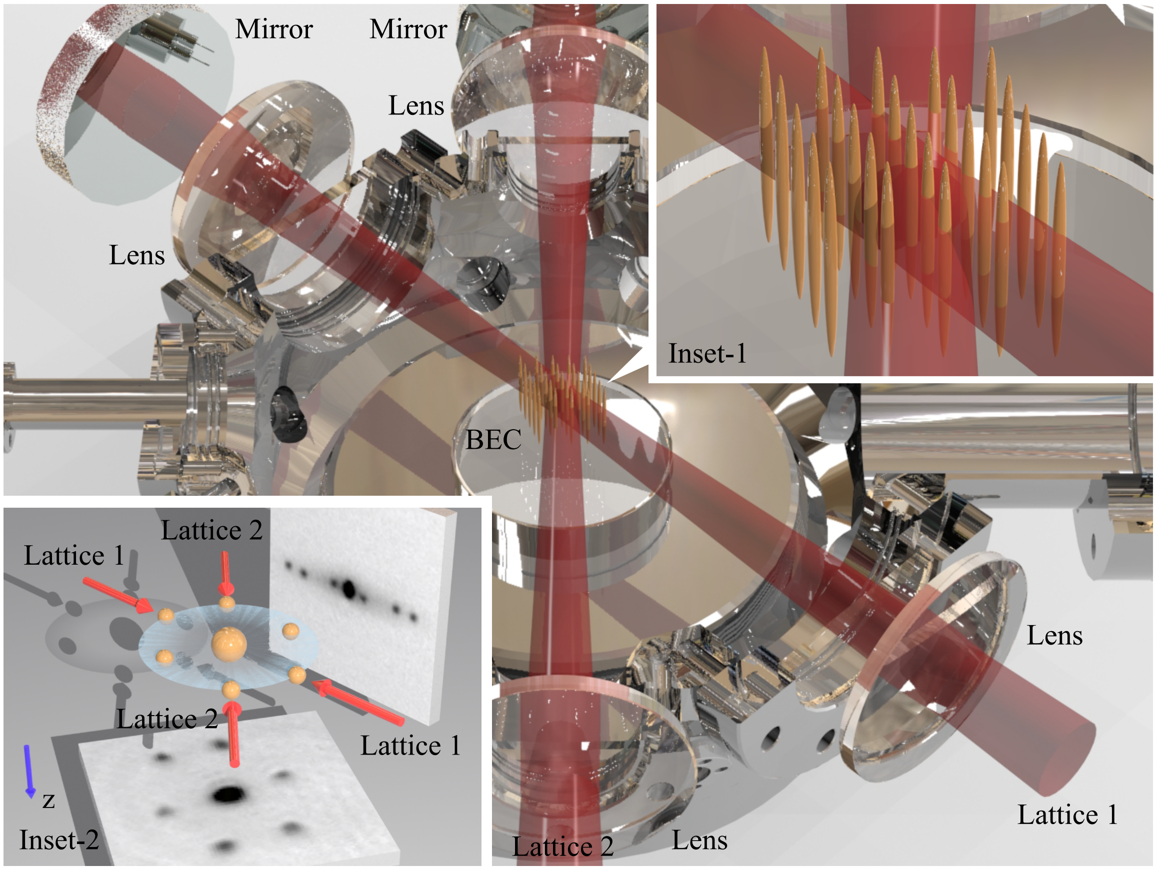

Figure 4.3: Schematic of our lattice setup. Both lattice beams are retro-reflected. Inset-1: A enlarged view of the center region of the main figure. Atoms in 2D lattices are shown in the center. Inset-2: Schematic of the reciprocal lattice. Absorption images taken from two different directions are also shown.

retro-reflected to form standing waves, as shown in Fig. 4.3. To eliminate cross interference between different beams, the two lattice beams are frequency-shifted by 20 MHz with respect to each other. u_L is calibrated using Kapitza-Dirac diffraction patterns. All lattice depths studied in this Chapter are kept below $15.0(5)E_R$ to avoid SF-MI phase transitions and thus maintain a sufficient superfluid fraction in our system. We apply a resonant rf-pulse of a proper amplitude and duration to lattice-trapped BECs for preparing an initial state with any desired combination of the three m_F states at $q_B/h = 42$ Hz, and then quench q_B to a desired value. After holding atoms for a variable time duration t_{hold}, we abruptly switch off all lattice and trapping potentials. The fractional population of each m_F state, ρ_{m_F}, is measured with Stern-Gerlach absorption imaging after a certain time of flight t_{TOF}. The initial ρ_0 is 0.46, the initial relative phase among the three spin states is zero, and t_{TOF}

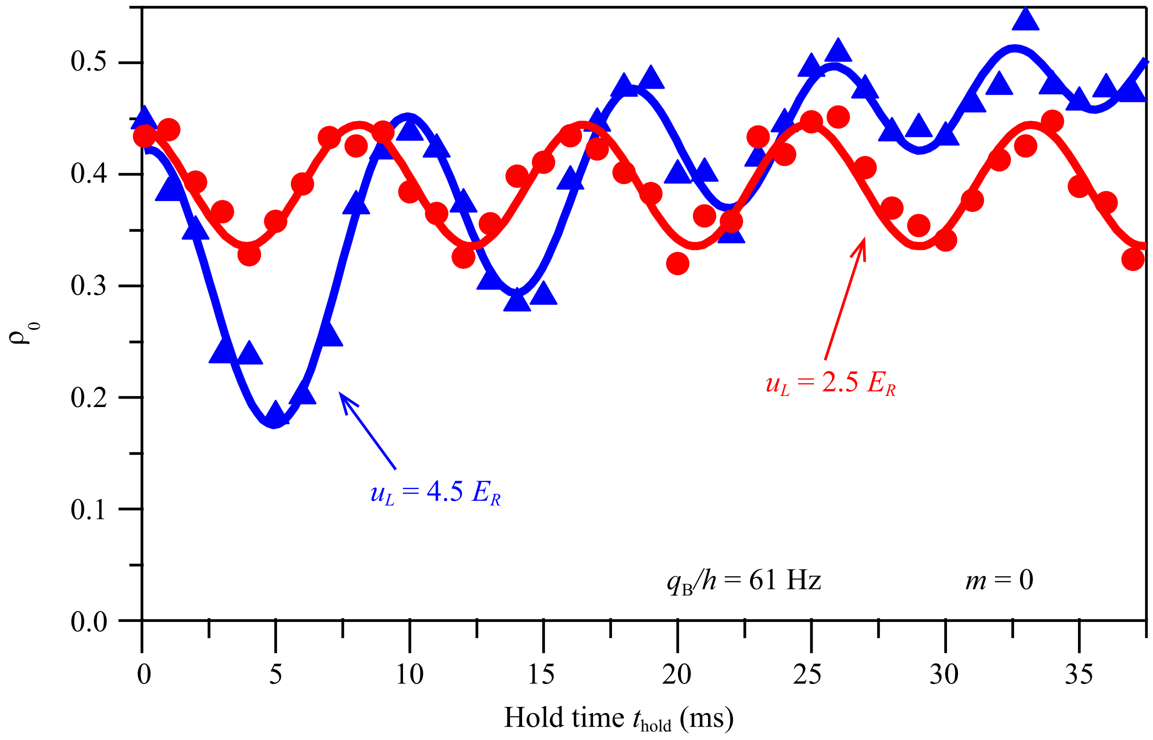

Figure 4.4: Time evolutions of ρ_0 when $u_L = 4.5E_R$ (triangles) and $2.5E_R$ (circles). Solid lines are sinusoidal fits to extract oscillation periods.

is 6 ms unless otherwise specified. The total magnetization $m = \rho_{+1} - \rho_{-1}$ appears to be conserved in every time evolution studied in this paper.

4.5 Spin dynamics in optical lattices

In the presence of a shallow lattice of $u_L < 5E_R$, we observe spin population oscillations similar to those occurring in free space, as shown in Fig. 4.4. Sharp interference peaks are observed after we release BECs from the shallow lattice (see Fig. 4.3 inset-2), which indicates coherence and superfluid behavior in the system.

As the lattice is made deeper, spin oscillations damp out more quickly (especially in the vicinity of each separatrix). These fast damped oscillations make it hard to extract oscillation periods and precisely locate each separatrix even at a moderate u_L (e.g., $4.5E_R$), as shown in Fig. 4.4. A typical anharmonic spin oscillation near a separatrix is shown in the

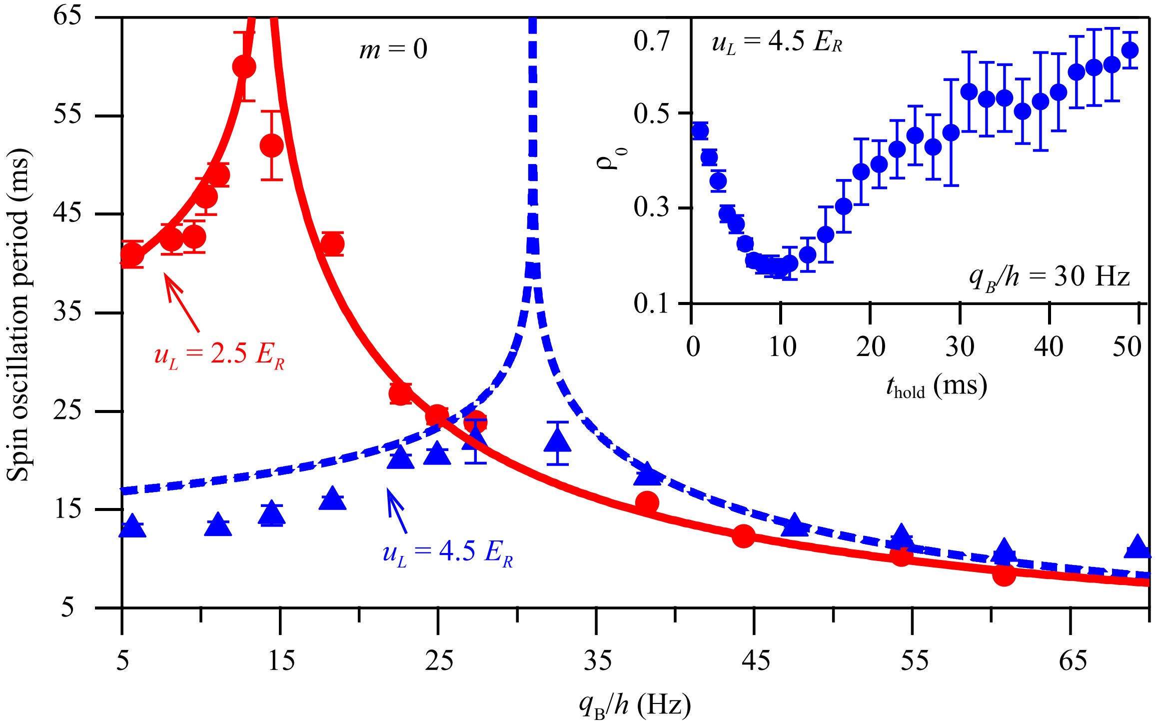

Figure 4.5: Oscillation period versus q_B. Lines are fits based on SMA. Inset: time evolution of ρ_0 near a separatrix. Uncertainties are extracted from 15-20 repeated Stern-Gerlach measurements. Large uncertainties of ρ_0 near the separatrix may result from shot-to-shot fluctuations, similar to Ref. (Liu *et al.*, 2009a).

inset in Fig. 4.5.

In addition, the separatrix position shifts to a much higher q_B when u_L increases, as shown in Fig. 4.5. We find our system can be understood by two models: the Bose-Hubbard model discussed in Ref. (Mahmud and Tiesinga, 2013) and Section 4.5 for $u_L > 5E_R$, and SMA defined in Ref. (Zhang *et al.*, 2005) and Section 3.5 for $u_L < 5E_R$. We can estimate U_2 by $U_2 \simeq q_B$ at each separatrix for the initial state studied in Figs. 4.4 and 4.5 (Zhao *et al.*, 2014b). Therefore, the observed lattice-tuned separatrix in phase space (i.e., the separatrix position shifts with u_L) is thus mainly due to the fact that U_2 greatly increases with u_L. Fig. 4.5 shows a good numerical example: U_2/h is increased from 14 Hz to 32 Hz by changing u_L from $2.5E_R$ to $4.5E_R$.

4.6 Steady states of spinor gases in lattices

‘

Spin oscillations completely damp out and spinor BECs reach their steady states when t_{hold} is long enough, as shown in Fig. 4.6(c). Sufficiently deep lattices are found to bring some interesting changes to the steady states. Figure 4.6(c) demonstrates one of such changes: once u_L is sufficiently large, the steady states undergo a phase transition from a LP phase (where $\rho_0 = 1$) to a BA phase (where $0 < \rho_0 < 1$) at $m = 0$. We repeat the same measurements with only one parameter changed, i.e., by blocking the retro-reflected path of each lattice beam to eliminate standing waves and construct a crossed optical dipole trap (ODT). Its resulting trap depth is u_{ODT}, as illustrated in Fig. 4.6(e). The power of every beam in Fig. 4.6(d-f) is four times of that in Fig. 4.6(a-c) to ensure $u_L = u_{\text{ODT}}$. Our data in Fig. 4.6(f) show that spinor BECs at $m = 0$ always reach the LP phase when there are no standing waves. The dramatically different results shown in Fig. 4.6 imply a necessity to understand this LP-BA transition with lattice-modified band structures.

We then study spin oscillations and steady states within a much wider range of u_L and m. Steady states appear to depend sigmoidally on u_L at a fixed q_B, as shown in Fig. 4.7. The inset in Fig. 4.7 demonstrates another surprising result: the observed relationship between ρ_0 and m in steady states at a sufficiently large u_L is well fit by $\rho_0 = (1 - |m|)/3$, which is drastically different from a well-known mean-field prediction (i.e., $\rho_0^{D\approx 0}$ as illustrated by the black dotted line) in Eq. 3.23. This mean-field prediction assumes quantum depletion D is negligible, where D represents the fraction of atoms situated in non-zero momentum states. Based on Bogoliubov theory, the $D \approx 0$ assumption is correct in free space and very shallow lattices for our system (Xu *et al.*, 2006). We extract D from TOF images with two fitting methods which render similar results, as shown in Fig. 4.8. We then confirm $D < 5\%$ at $u_L \leq 3E_R$. Note that the trapping frequency in each lattice site is much bigger than U_0/h (Xu *et al.*, 2006). Our TOF images thus reflect the momentum distribution at the instant of the lattice release and enable us to directly measure D.

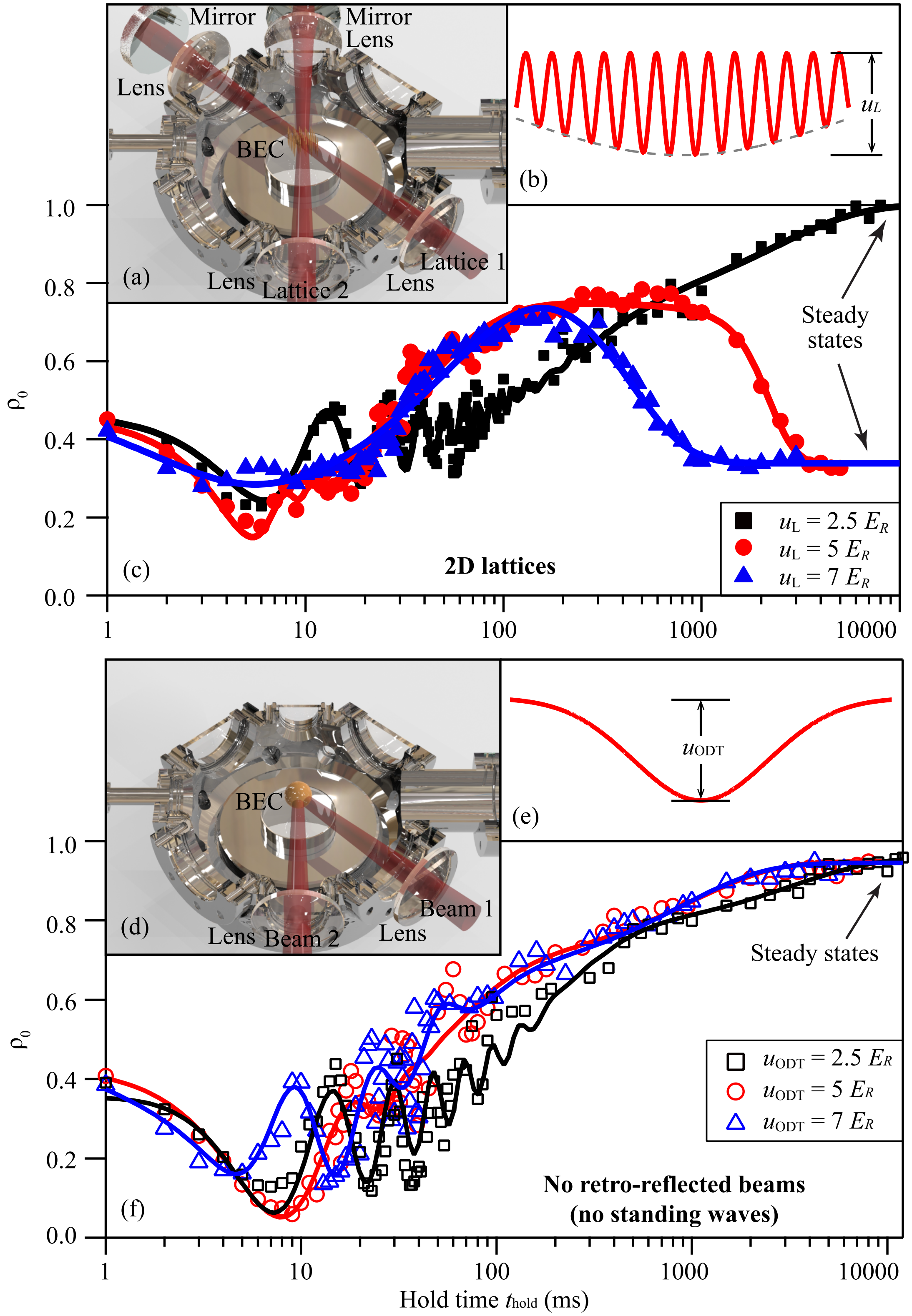

Figure 4.6: (a) A schematic of our lattice setup. (b) An illustration of the resulting lattice potential. (c) Time evolutions of ρ_0 at $q_B/h = 42$ Hz and $m = 0$. Lines are fits to guide the eye. (d-f) Respectively similar to Panels (a-c) except that each beam is not retro-reflected.

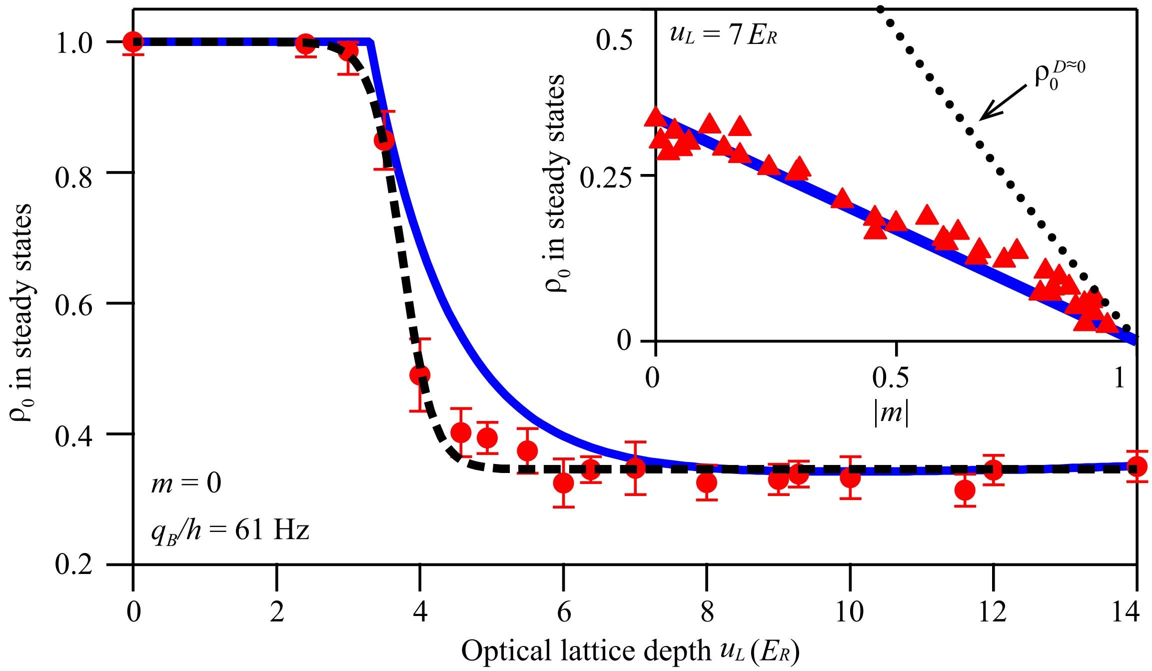

Figure 4.7: ρ_0 in steady states as a function of u_L (main figure) and $|m|$ (inset figure). Solid lines are predictions derived from Eq. (4.20). The dashed and dotted lines respectively represent a sigmoidal fit and the mean field prediction $\rho_0^{D\approx 0}$, i.e., Eq. 3.23.

We also find that D increases with t_{hold} and u_L, and approaches one in steady states when $u_L > 10E_R$, as shown in Fig. 4.9. This lattice-enhanced quantum depletion mainly results from the lattice-flatten dispersion relation and lattice-enhanced interactions, and was originally observed in scalar BEC systems (Xu *et al.*, 2006). We develop one phenomenological model to incorporate the observed D and find this model can semi-quantitatively describe our data without adjustable parameters, as shown in Figs. 4.7 and 4.10. In this model, the steady states are determined by a comparison between $T(\mathbf{k}, m_F = 0)$ and $T(0, m_F = \pm 1)$, where $T(\mathbf{k}, m_F)$ is the dispersion relation of the m_F state. Figure 4.11 illustrates two example comparisons. Note that only the first Brillouin zone is considered, since the population in higher bands is negligible. Based on Refs. (Xu *et al.*, 2006; Fisher *et al.*, 1989; Jaksch *et al.*, 1998) and Eq. 4.18, we calculate $T(\mathbf{k}, m_F)$ as follows,

$$T(\mathbf{k}, m_F) = 4J \sum_{\alpha=x,y} \sin^2\left(\frac{\pi k_\alpha}{2k_L}\right) + E_R \frac{k_z^2}{k_L^2} + q_B m_F^2 \; , \tag{4.19}$$

where a uniform density function is applied along the vertical direction without a lattice

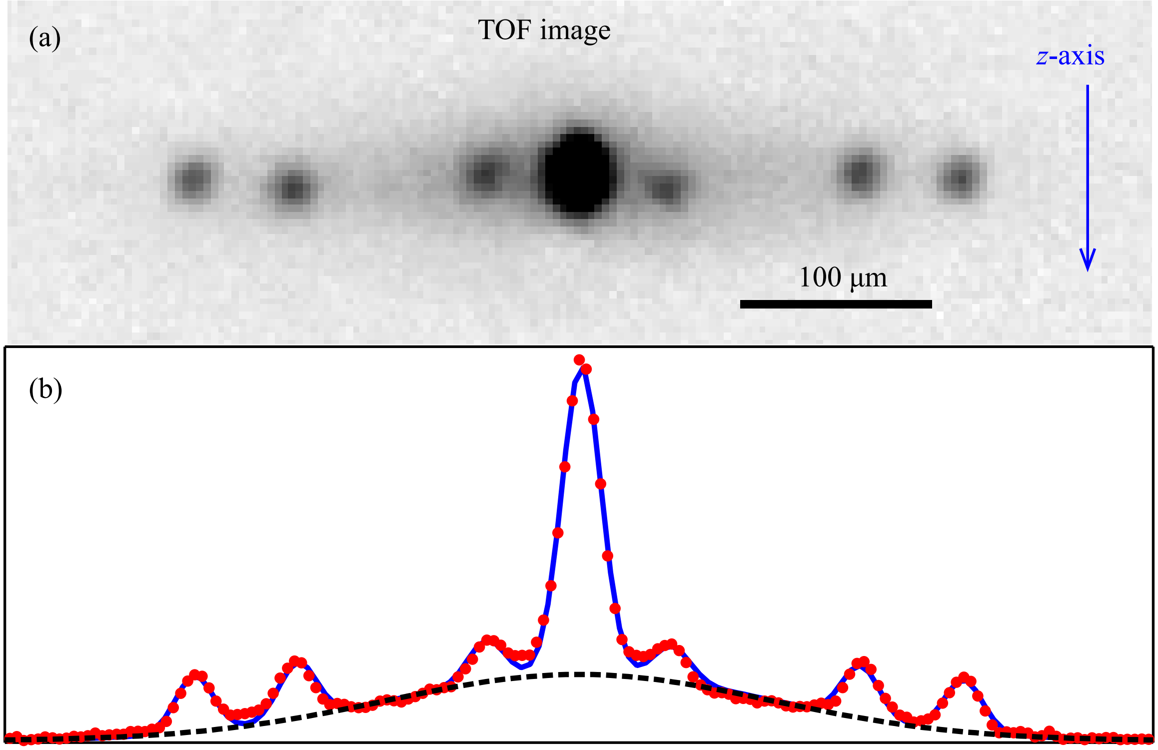

Figure 4.8: (a) A typical TOF image for extracting the number of atoms in all non-zero momentum states N_D. Using Method-1 suggested by Ref.(Xu *et al.*, 2006): we mask off all the interference peaks, and conduct a 2D Gaussian fit to the background for extracting N_D. The extracted D is 53% from this image. (b) Density profile (red dotted line) of the image shown in Panel (a) through all interference peaks. Using Method-2 (blue solid line), we plot a density profile of a TOF image through all interference peaks, and then fit the density profile with a combination of eight Gaussian functions, i.e., one function to each interference peak, and the eighth one to the broad background for extracting N_D. The extracted D is 52.5%. The black dashed line highlights the quantum depleted fraction.

(the z-axis), and J is calculated using a Wannier density function along each of the two horizontal directions with lattices. The linear Zeeman effect is ignored because it remains unchanged in coherent inter-conversions.

We divide $T(\mathbf{k}, m_F = 0)$ into two regions based on $T(0, m_F = \pm 1)$, i.e., set the boundary of the two regions at $\mathbf{k}_c$ which satisfies $T(\mathbf{k}_c, m_F = 0) = T(0, m_F = \pm 1)$, as marked by vertical dotted lines in Fig. 4.11. The dispersion relations are significantly flattened as u_L increases, since the predicted width of the first band is $\sim 4J$ and J exponentially reduces with u_L (Fisher *et al.*, 1989; Xu *et al.*, 2006). To clearly explain our model using the dispersion relations shown in Fig. 4.11, we only consider $m = 0$ and $k_y = k_z = 0$ in this

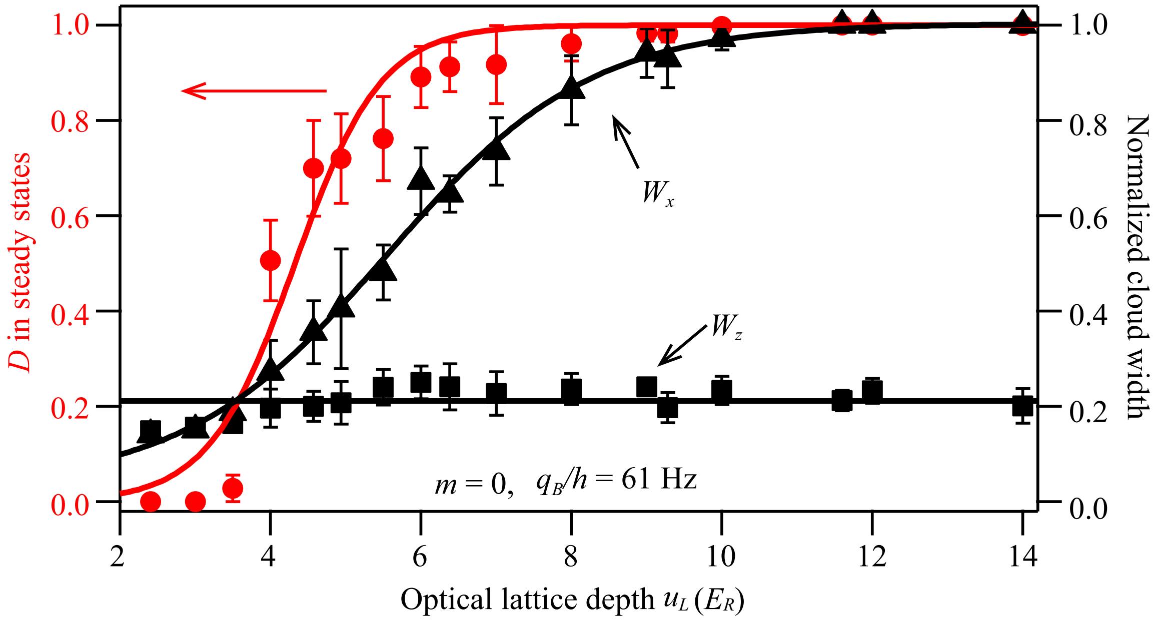

Figure 4.9: W_x (triangles), W_z (squares), and D (circles) in steady states as a function of u_L. The widths are normalized by k_L. Lines are respectively sigmoid fits to W_x and D, and a linear fit to W_z.

paragraph. In Region-1 where $0 \leq |k_x| < |\mathbf{k}_c|$, atoms in the $m_F = 0$ state always have energy smaller than those in the $m_F = \pm 1$ states. The steady states should thus be the $m_F = 0$ state (i.e., $\rho_0 = 1$), which equals $\rho_0^{D\approx 0}$. When D is big enough, atoms start to occupy Region-2 where $|\mathbf{k}_c| \leq |k_x| \leq k_L$. The $m_F = 0$ atoms in Region-2 are degenerate with $m_F = \pm 1$ atoms at certain other momenta. This degeneracy may account for the phenomenological relationship shown in Fig. 4.7, i.e, $\rho_0 = 1/3$ in steady states at a big u_L. Our data and the dispersion relations thus suggest that atoms in steady states may be equally distributed among the three m_F states at a big enough D.

We can apply similar discussions and our model to all non-zero m. Thus ρ_0 in the steady states is expressed as,

$$\rho_0 \approx \int_{\text{Region}-1} n(\mathbf{k})\rho_0^{D\approx 0}\mathrm{d}\mathbf{k} + \int_{\text{Region}-2} n(\mathbf{k})\frac{1-|m|}{3}\mathrm{d}\mathbf{k}\ . \tag{4.20}$$

The normalized atomic density in steady states, $n(\mathbf{k})$, is calculated by the following phenomenological formula: $n(\mathbf{k}) = (1-D)\delta_{\mathbf{k}} + D\exp[-(k_x^2/W_x^2 + k_y^2/W_y^2 + k_z^2/W_z^2)/2]/A$, where W_x and W_z are the half widths of a 2d Gaussian fit to a TOF distribution within the first

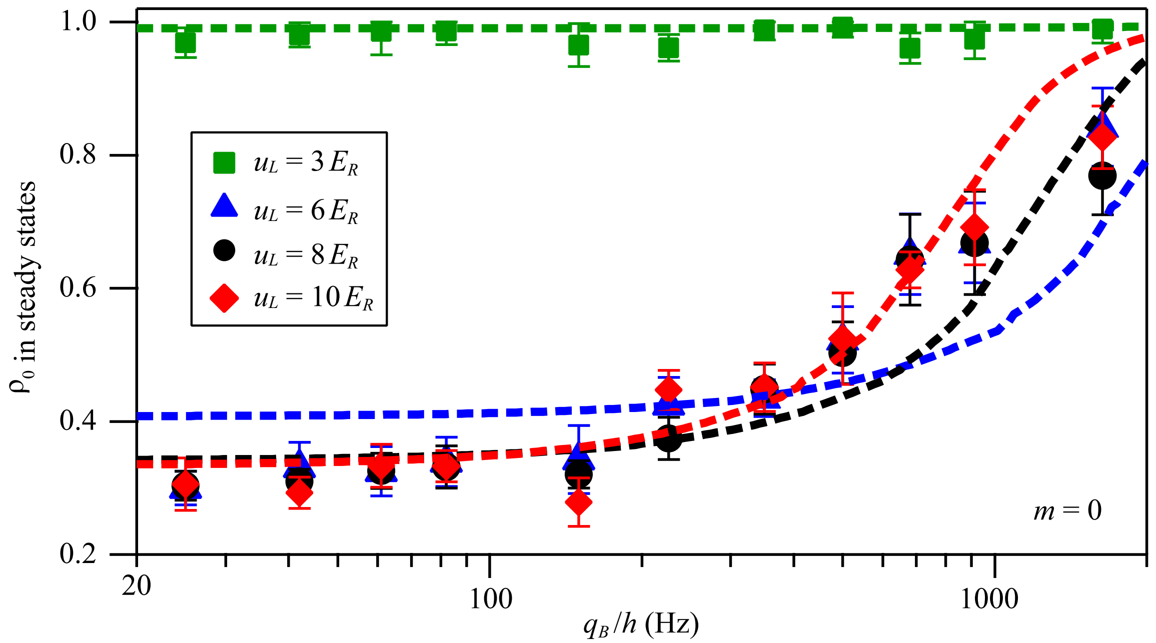

Figure 4.10: ρ_0 in steady states as a function of q_B. Dashed lines are predictions derived from Eq. (4.20). Green, blue, black, and red colors respectively represent results at $u_L = 3$, 6, 8, and $10E_R$.

Brillouin zone, $W_y = W_x$, A is a normalization factor $A = \int \exp[-(k_x^2/W_x^2 + k_y^2/W_y^2 + k_z^2/W_z^2)/2]d\mathbf{k}$, integrate over the first Brillouin zone, and δ is a Dirac-delta function. Figure 4.9 shows that W_x and D sigmoidally increase with u_L, and saturate at their peak values when $u_L > 10E_R$, i.e., atoms occupy all available states and quantum depletion saturates the first Brillouin zone in a deep lattice. In contrast, W_z appears to be independent of u_L, which implies a constant system temperature.

The observed sigmoidal dependence of steady states on u_L and the exponential dependence on q_B can be explained by our model, i.e., Eq. 4.20, as respectively shown in Figs. 4.7 and 4.10. Quantitative agreements between our model and data are found everywhere except in high magnetic fields where $q_B/h > 1000$ Hz, and in a lattice where $4E_R \le u_L \le 6E_R$. Limited imaging resolutions and heating induced by an extra magnetic coil in creating high q_B may both contribute to the discrepancy.

To better understand the LP-BA phase transition, we plot ρ_0 versus U_2D/q_B (a dimensionless ratio) at $m = 0$ in Fig. 4.12. Here U_2/q_B is the key factor determining the spinor

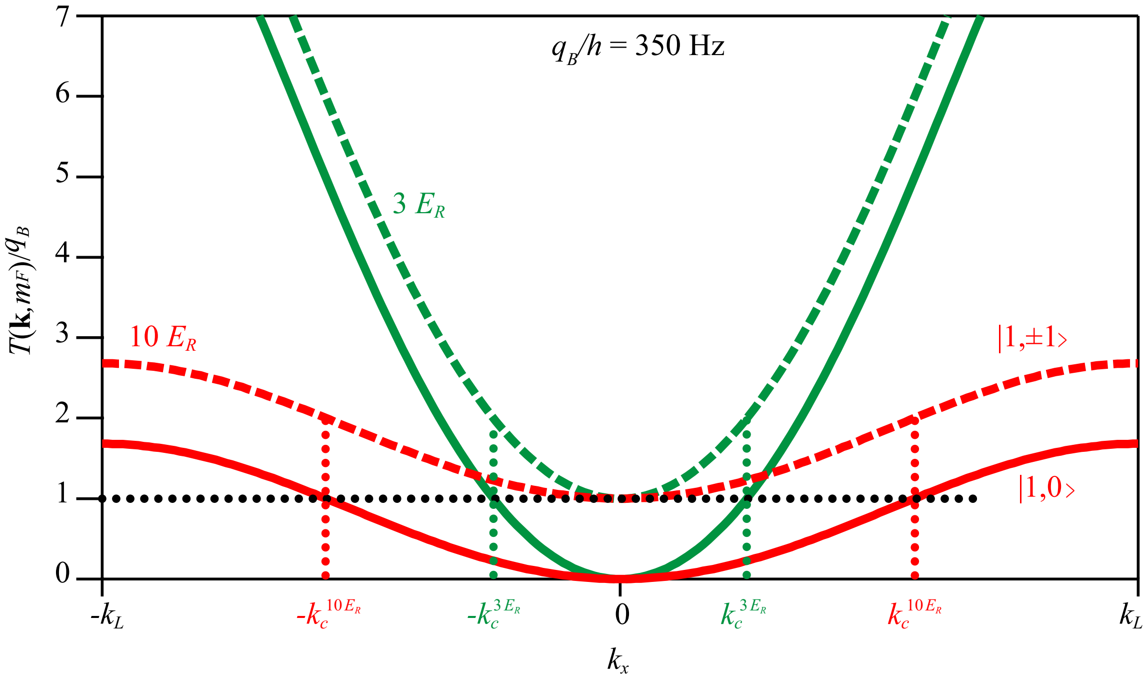

Figure 4.11: Dispersion relations normalized by q_B as a function of k_x when $k_y = k_z = 0$. Solid (dashed) lines represent results of the $m_F = 0$ ($m_F = \pm 1$) states. The black horizontal dotted line marks $T(\mathbf{k}, m_F) = q_B$, and vertical dotted lines mark boundaries between Region-1 and Region-2 at $u_L = 3$ and $10E_R$.

dynamics in free space, D represents the lattice-induced effect, and both D and U_2 increase with the spin-independent interaction U_0. Two interesting results are found in Fig. 4.12: all 80 data points taken at very different u_L and q_B are fit by one sigmoid function; and the critical point of the LP-BA transition appears to be $U_2D/q_B \sim 0.01$. (In contrast, each predicted separatrix locates around $U_2/q_B = 1$ based on SMA and parameters studied in Fig. 4.12.) The LP-BA transition may thus result from a competition between q_B and the “effective” interaction U_2D, i.e., regions with strong enough interactions may prefer the BA phase. In principle, we can verify this using other methods which can efficiently tune interatomic interactions, e.g., via Feshbach resonances.

In conclusion, we have conducted the first experimental study on dynamics and the phase diagram of lattice-trapped antiferromagnetic spinor BECs. A lattice-tuned separatrix in phase space and the LP-BA phase transition in steady states have been observed. We have found that ρ_0, D, and thus the main findings of this paper are nearly independent of

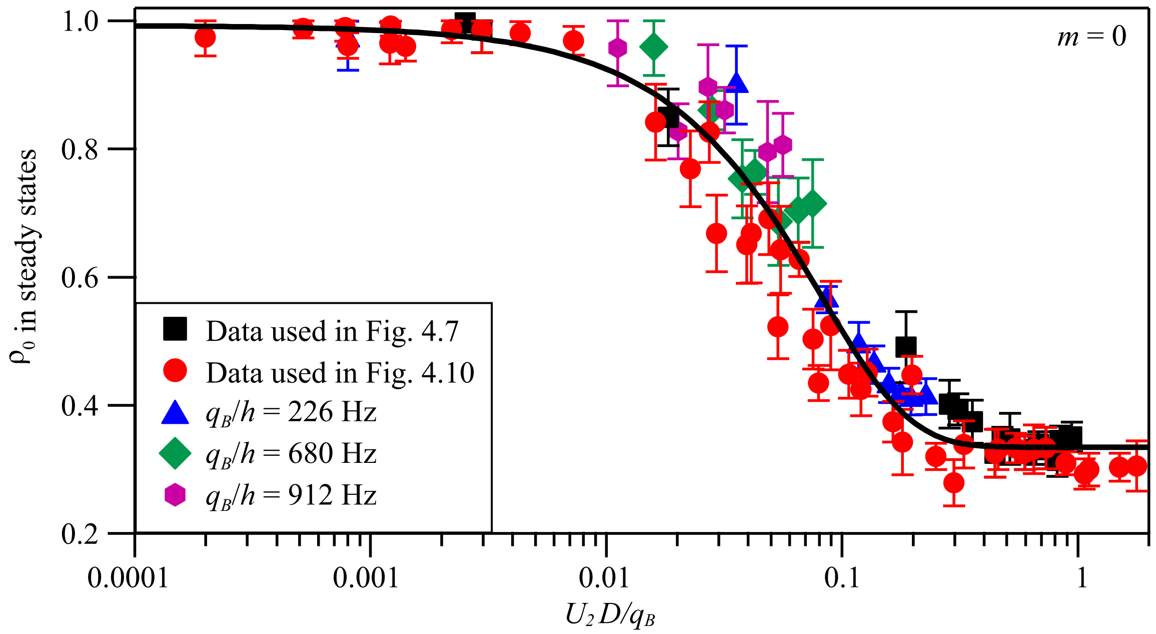

Figure 4.12: ρ_0 in steady states versus U_2D/q_B. Black, red, blue, green, and purple colors respectively represent data used in Figs. 4.7 and 4.10, and additional data taken at $q_B/h =$ 226, 680, and 912 Hz. The solid line is a sigmoid fit.

$t_{\rm TOF}$. We have also developed a phenomenological model that describes our data without adjustable parameters.

CHAPTER V

FUTURE DIRECTIONS: SPIN-SQUEEZING AND ITS IMMEDIATE APPLICATIONS IN QUANTUM INFORMATION SCIENCE

It is well known that nonlinear spin Hamiltonians give rise to spin squeezing (Duan *et al.*, 2000; Shen and Duan, 2013; Kitagawa and Ueda, 1993; Hamley *et al.*, 2012; Gerving *et al.*, 2012). A simplest Hamiltonian that yields squeezing is $\overrightarrow{\alpha} \cdot \overrightarrow{S} + \beta S_z^2$. Ref. (Duan *et al.*, 2000) was able to theoretically realize such a simple nonlinear Hamiltonian for a two-component BEC and showed the existence of squeezing and entanglement. The nonlinearity explained in Ref. (Duan *et al.*, 2000) arose from self interactions in BECs. Self interactions lead to a wide variety of nonlinear effects in BECs, such as solitons (Strecker *et al.*, 2002) and four wave mixing (Deng *et al.*, 1999; Denschlag *et al.*, 2000). At the level of quantum fluctuations, it has been argued that even a one-component BEC can give rise to sub-Poissonian statistics of the BEC density (Dunningham *et al.*, 2002; Deb and Agarwal, 2002). A few experimental groups have recently made significant progress on generating spin-squeezing in a ^{87}Rb BEC, such as Ref. (Riedel *et al.*, 2010) reported a spin-squeezed state with spin-squeezing parameter of -2.5 ± 0.6 dB from controlling elastic collisional interactions with a state-dependent microwave potential, and Ref. (Hamley *et al.*, 2012) demonstrated spin-nematic quadrature squeezing with 8-10 dB improvements over the standard quantum limit due to spin-exchange collisions.

On the other hand, collective coupling of spinor BECs to a light field introduced by a quantum non-demolition (QND) measurement can also create spin-squeezed states. Quantum interface of atoms and a light field and its applications in magnetometry have been studied for decades in various mediums, such as hot atomic vapors, atoms confined in magneto-optical traps (MOT), alkali atoms trapped in an optical dipole trap, and BECs. A BEC appears to be a very attractive medium because it overcomes a number of problems associated with other mediums. Thermal diffusive motions and spin depolarization in hot atomic vapors are frozen out at the ultracold BEC temperatures (hundreds of nanoKelvin). Coherent time of a spinor BEC is significantly longer than those observed in optical or MOT trapped atomic ensembles (Liu *et al.*, 2009a). And most importantly, resonant optical depth in a BEC is very high and can reach a few hundred or more. A good example of these advantages is that the first classical coherent storage of light was observed in BECs (Liu *et al.*, 2001).

The QND measurement projects the system into an eigenstate of the observable such that subsequent measurements of the same observable will return the same result. It can turn a coherent spin state into a spin-squeezed spin state by reducing the uncertainty of the total spin of the BEC in one direction and increasing the uncertainty in the orthogonal direction. Higher detection power and larger optical depth of the ensemble will create larger spin-squeezing with this method. Working with BECs and performing a measurement in a build-up cavity (Tuchman *et al.*, 2006) are two possible methods to obtain larger optical depth, and thus more spin-squeezing. The QND detection can be used both to create the state and to detect the state. One good candidate for the QND projection is Faraday rotation spectroscopy which measures the rotation of the linear polarization of a far off resonant laser beam. Our group will experimentally implement this idea on spinor BECs and to calculate the expected signatures in magneto optical rotations of the incoming light. In order to make the Faraday measurement QND, we can stroboscopically modulate the probe light intensity at a frequency of $2f_L$. Therefore the spin-state is measured with peak intensity when the squeezed axis is along the detection axis, and with minimum intensity when the anti-squeezed axis is along the detection axis (Caves *et al.*, 1980; Braginsky *et al.*, 1992).

In addition, our group will also investigate immediate applications of spin-squeezing in quantum information science. For example, implement the first ultra-precise magnetometer of micron spatial resolution and femto-tesla field sensitivity with spin-squeezed sodium BECs. Precise magnetometers have made it possible to image vortex dynamics in two-dimensional superconducting films, map geomagnetic anomalies, and sense the magnetic field of the brain. We will apply the proven optical measurement methods of atomic magnetometry (Liu *et al.*, 2009b; Budker and Romalis, 2007), but replace the hot atomic vapor at 500 Kelvin with ultracold BECs at 100 nanoKelvin. Thermal diffusions that limit the sensitivity of hot-vapor magnetometers are frozen out at BEC temperatures. Spin noise in conventional magnetometers is suppressed by spin-squeezing. This would improve the field sensitivity of the spinor-BEC-based magnetometer beyond the shot-noise limit. This spinor-BEC-based magnetometer will also be upgraded to a precise magnetic scanning microscope via spatially scanning optical traps.

REFERENCES

Aikawa, K., A. Frisch, M. Mark, S. Baier, A. Rietzler, R. Grimm, and F. Ferlaino. “Bose-einstein condensation of erbium.” Phys. Rev. Lett. **108**, 210401 (2012).

Anderson, M. H., J. R. Ensher, M. R. Matthews, C. E. Wieman, and E. A. Cornell. “Observation of bose-einstein condensation in a dilute atomic vapor.” Science **269**, 198–201 (1995).

Batrouni, G. G., V. G. Rousseau, and R. T. Scalettar. “Magnetic and superfluid transitions in the one-dimensional spin-1 boson hubbard model.” Phys. Rev. Lett. **102**, 140402 (2009).

Becker, C, P Soltan-Panahi, J Kronjäger, S Drscher, K Bongs, and K Sengstock. “Ultracold quantum gases in triangular optical lattices.” New Journal of Physics **12**, 065025 (2010).

Bell, S. C., M. Junker, M. Jasperse, L. D. Turner, Y.-J. Lin, I. B. Spielman, and R. E. Scholten. “A slow atom source using a collimated effusive oven and a single-layer variable pitch coil zeeman slower.” Review of Scientific Instruments **81**, 013105 (2010).

Black, A. T., E. Gomez, L. D. Turner, S. Jung, and P. D. Lett. “Spinor dynamics in an antiferromagnetic spin-1 condensate.” Phys. Rev. Lett. **99**, 070403 (2007).

Bloch, Felix. “über die quantenmechanik der elektronen in kristallgittern.” Zeitschrift für Physik **52**, 555–600 (1929).

Bookjans, E. M., A. Vinit, and C. Raman. “Quantum phase transition in an antiferromagnetic spinor bose-einstein condensate.” Phys. Rev. Lett. **107**, 195306 (2011).

Bradley, C. C., C. A. Sackett, J. J. Tollett, and R. G. Hulet. “Evidence of bose-einstein condensation in an atomic gas with attractive interactions." Phys. Rev. Lett. **75**, 1687–1690 (1995).

Braginsky, V.B., F.Y. Khalili, and K.S. Thorne. *Quantum Measurement* (Cambridge University Press, 1992).

Breit, G. and I. I. Rabi. "Measurement of nuclear spin." Phys. Rev. **38**, 2082–2083 (1931).

Budker, Dmitry and Michael Romalis. "Optical magnetometry." Nature Physics **3**, 227–234 (2007).

Caves, Carlton M., Kip S. Thorne, Ronald W. P. Drever, Vernon D. Sandberg, and Mark Zimmermann. "On the measurement of a weak classical force coupled to a quantum-mechanical oscillator. i. issues of principle." Rev. Mod. Phys. **52**, 341–392 (1980).

Chang, Ming-Shien, Qishu Qin, Wenxian Zhang, Li You, and Michael S. Chapman. "Coherent spinor dynamics in a spin-1 bose condensate." Nature Physics **1**, 111 (2005a).

Chang, Ming-Shien, Qishu Qin, Wenxian Zhang, Li You, and Michael S. Chapman. "Coherent spinor dynamics in a spin-1 bose condensate." Nature Physics **1**, 111–116 (2005b).

Cheiney, P., O. Carraz, D. Bartoszek-Bober, S. Faure, F. Vermersch, C. M. Fabre, G. L. Gattobigio, T. Lahaye, D. Gury-Odelin, and R. Mathevet. "A zeeman slower design with permanent magnets in a halbach configuration." Review of Scientific Instruments **82**, 063115 (2011).

Chen, Zilong, Justin G. Bohnet, Shannon R. Sankar, Jiayan Dai, and James K. Thompson. "Conditional spin squeezing of a large ensemble via the vacuum rabi splitting." Phys. Rev. Lett. **106**, 133601 (2011).

Choi, Jae-yoon, Woo Jin Kwon, and Yong-il Shin. "Observation of topologically stable 2d skyrmions in an antiferromagnetic spinor bose-einstein condensate." Phys. Rev. Lett. **108**, 035301 (2012).

Cornish, S. L., N. R. Claussen, J. L. Roberts, E. A. Cornell, and C. E. Wieman. "Stable

^{85}Rb bose-einstein condensates with widely tunable interactions." Phys. Rev. Lett. **85**, 1795–1798 (2000).

Davis, K. B., M. O. Mewes, M. R. Andrews, N. J. van Druten, D. S. Durfee, D. M. Kurn, and W. Ketterle. "Bose-einstein condensation in a gas of sodium atoms." Phys. Rev. Lett. **75**, 3969–3973 (1995).

de Escobar, Y. N. Martinez, P. G. Mickelson, M. Yan, B. J. DeSalvo, S. B. Nagel, and T. C. Killian. "Bose-einstein condensation of ^{84}Sr." Phys. Rev. Lett. **103**, 200402 (2009).

Deb, B. and G. S. Agarwal. "Tripartite entanglement in a bose-einstein condensate by stimulated bragg scattering." Phys. Rev. A **65**, 063618 (2002).

Dedman, C. J., J. Nes, T. M. Hanna, R. G. Dall, K. G. H. Baldwin, and A. G. Truscott. "Optimum design and construction of a zeeman slower for use with a magneto-optic trap." Review of Scientific Instruments **75** (2004).

Deng, L., E. W. Hagley, J. Wen, M. Trippenbach, Y. Band, P. S. Julienne, J. E. Simsarian, K. Helmerson, S. L. Rolston, and W. D. Phillips. "Formation and propagation of matter-wave soliton trains." Nature **398**, 218–220 (1999).

Denschlag, J., J. E. Simsarian, D. L. Feder, Charles W. Clark, L. A. Collins, J. Cubizolles, L. Deng, E. W. Hagley, K. Helmerson, W. P. Reinhardt, S. L. Rolston, B. I. Schneider, and W. D. Phillips. "Generating solitons by phase engineering of a bose-einstein condensate." Science **287**, 97–101 (2000).

Duan, L.-M., A. Sørensen, J. I. Cirac, and P. Zoller. "Squeezing and entanglement of atomic beams." Phys. Rev. Lett. **85**, 3991–3994 (2000).

Dunningham, J. A., K. Burnett, and Stephen M. Barnett. "Interferometry below the standard quantum limit with bose-einstein condensates." Phys. Rev. Lett. **89**, 150401 (2002).

Durfee, Dallin S. *Dynamic Properties of Dilute Bose-Einstein Condensates.* Ph.D. thesis, Massachusetts Institute of Technology (1999).

Einstein, A. "Quantentheorie des einatomigen idealen gases." Sitzungsberichte der Preussischen Akademie der Wissenschaften **1**, 3 (1925).

Falke, Stephan, Horst Knöckel, Jan Friebe, Matthias Riedmann, Eberhard Tiemann, and Christian Lisdat. "Potassium ground-state scattering parameters and born-oppenheimer potentials from molecular spectroscopy." Phys. Rev. A **78**, 012503 (2008).

Fisher, Matthew P. A., Peter B. Weichman, G. Grinstein, and Daniel S. Fisher. "Boson localization and the superfluid-insulator transition." Phys. Rev. B **40**, 546–570 (1989).

Fried, Dale G., Thomas C. Killian, Lorenz Willmann, David Landhuis, Stephen C. Moss, Daniel Kleppner, and Thomas J. Greytak. "Bose-einstein condensation of atomic hydrogen." Phys. Rev. Lett. **81**, 3811–3814 (1998).

Fukuhara, Takeshi, Seiji Sugawa, and Yoshiro Takahashi. "Bose-einstein condensation of an ytterbium isotope." Phys. Rev. A **76**, 051604 (2007).

Gerbier, Fabrice, Artur Widera, Simon Fölling, Olaf Mandel, and Immanuel Bloch. "Resonant control of spin dynamics in ultracold quantum gases by microwave dressing." Phys. Rev. A **73**, 041602 (2006).

Gersch, H. A. and G. C. Knollman. "Quantum cell model for bosons." Phys. Rev. **129**, 959–967 (1963).

Gerving, C.S., T.M. Hoang, B.J. Land, M. Anquez, C.D. Hamley, and M.S. Chapman. "Non-equilibrium dynamics of an unstable quantum pendulum explored in a spin-1 bose-einstein condensate." Nature Communications **3**, 1169 (2012).

Gibble, Kurt E., Steven Kasapi, and Steven Chu. "Improved magneto-optic trapping in a vapor cell." Opt. Lett. **17**, 526–528 (1992).

Greiner, Markus, Olaf Mandel, Theodor W. Hänsch, and Immanuel Bloch. "Collapse and revival of the matter wave field of a boseeinstein condensate." Nature **419**, 51–54 (2002).

Griesmaier, Axel, Jörg Werner, Sven Hensler, Jürgen Stuhler, and Tilman Pfau. "Bose-einstein condensation of chromium." Phys. Rev. Lett. **94**, 160401 (2005).

Gross, C., H. Strobel, E. Nicklas, T. Zibold, N. Bar-Gill, G. Kurizki, and M. K. Oberthaler. "Atomic homodyne detection of continuous-variable entangled twin-atom states." Nature **480**, 219–223 (2011).

Guzman, J., G.-B. Jo, A. N. Wenz, K. W. Murch, C. K. Thomas, and D. M. Stamper-Kurn. "Long-time-scale dynamics of spin textures in a degenerate $f = 1$ ^{87}rb spinor bose gas." Phys. Rev. A **84**, 063625 (2011).

Hall, D. S., M. R. Matthews, J. R. Ensher, C. E. Wieman, and E. A. Cornell. "Dynamics of component separation in a binary mixture of bose-einstein condensates." Phys. Rev. Lett. **81**, 1539–1542 (1998a).

Hall, D. S., M. R. Matthews, C. E. Wieman, and E. A. Cornell. "Measurements of relative phase in two-component bose-einstein condensates." Phys. Rev. Lett. **81**, 1543–1546 (1998b).

Hamley, C. D., C. S. Gerving, T. M. Hoang, E. M. Bookjans, and M. S. Chapman. "Spin-nematic squeezed vacuum in a quantum gas." Nature Physics **8**, 305–308 (2012).

Hayes, T.C. and P. Horowitz. *The Art of Electronics Student Manual*. Art of electronics / Paul Horowitz; Winfield Hill (Cambridge University Press, 1989).

Ho, Tin-Lun. "Spinor bose condensates in optical traps." Phys. Rev. Lett. **81**, 742–745 (1998).

Hubbard, J. "Electron correlations in narrow energy bands." Proceedings of the Royal Society of London A: Mathematical, Physical and Engineering Sciences **276**, 238–257 (1963).

Jacob, David, Lingxuan Shao, Vincent Corre, Tilman Zibold, Luigi De Sarlo, Emmanuel Mimoun, Jean Dalibard, and Fabrice Gerbier. "Phase diagram of spin-1 antiferromagnetic bose-einstein condensates." Phys. Rev. A **86**, 061601 (2012).

Jaksch, D., C. Bruder, J. I. Cirac, C. W. Gardiner, and P. Zoller. "Cold bosonic atoms in optical lattices." Phys. Rev. Lett. **81**, 3108–3111 (1998).

Jiang, J., L. Zhao, M. Webb, N. Jiang, H. Yang, and Y. Liu. "Simple and efficient all-optical production of spinor condensates." Phys. Rev. A **88**, 033620 (2013).

Jiang, J., L. Zhao, M. Webb, and Y. Liu. "Mapping the phase diagram of spinor condensates via adiabatic quantum phase transitions." Phys. Rev. A **90**, 023610 (2014).

Kawaguchi, Yuki and Masahito Ueda. "Spinor boseeinstein condensates." Physics Reports **520**, 253 – 381 (2012). Spinor Bose–Einstein condensates.

Ketterle, Wolfgang, Kendall B. Davis, Michael A. Joffe, Alex Martin, and David E. Pritchard. "High densities of cold atoms in a *dark* spontaneous-force optical trap." Phys. Rev. Lett. **70**, 2253–2256 (1993).

Kitagawa, Masahiro and Masahito Ueda. "Squeezed spin states." Phys. Rev. A **47**, 5138–5143 (1993).

Knoop, S., T. Schuster, R. Scelle, A. Trautmann, J. Appmeier, M. K. Oberthaler, E. Tiesinga, and E. Tiemann. "Feshbach spectroscopy and analysis of the interaction potentials of ultracold sodium." Phys. Rev. A **83**, 042704 (2011).

Kraft, Sebastian, Felix Vogt, Oliver Appel, Fritz Riehle, and Uwe Sterr. "Bose-einstein condensation of alkaline earth atoms: ^{40}Ca." Phys. Rev. Lett. **103**, 130401 (2009).

Kronjäger, J., C. Becker, P. Navez, K. Bongs, and K. Sengstock. "Magnetically tuned spin dynamics resonance." Phys. Rev. Lett. **97**, 110404 (2006).

Kuwamoto, T., K. Araki, T. Eno, and T. Hirano. "Magnetic field dependence of the dynamics of ^{87}Rb spin-2 bose-einstein condensates." Phys. Rev. A **69**, 063604 (2004).

Lamacraft, Austen. "Spin-1 microcondensate in a magnetic field." Phys. Rev. A **83**, 033605 (2011).

Lercher, A.D., T. Takekoshi, M. Debatin, B. Schuster, R. Rameshan, F. Ferlaino, R. Grimm, and H.-C. Ngerl. "Production of a dual-species bose-einstein condensate of rb and cs atoms." The European Physical Journal D **65**, 3–9 (2011).

Leslie, L. S., A. Hansen, K. C. Wright, B. M. Deutsch, and N. P. Bigelow. "Creation and detection of skyrmions in a bose-einstein condensate." Phys. Rev. Lett. **103**, 250401 (2009a).

Leslie, S. R., J. Guzman, M. Vengalattore, Jay D. Sau, Marvin L. Cohen, and D. M. Stamper-Kurn. "Amplification of fluctuations in a spinor bose-einstein condensate." Phys. Rev. A **79**, 043631 (2009b).

Leslie, Sabrina Rose Ann. *On Spinor Condensates as Amplifiers, Sensors and Tunable Quantum Playgrounds for Studies of Spin.* Ph.D. thesis, University of California, Berkeley (2008).

Lison, F., P. Schuh, D. Haubrich, and D. Meschede. "High-brilliance zeeman-slowed cesium atomic beam." Phys. Rev. A **61**, 013405 (1999).

Liu, Chien, Zachary Dutton, Cyrus H. Behroozi, and Lene Vestergaard Hau. "Observation of coherent optical information storage in an atomic medium using halted light pulses." Nature **409**, 490–493 (2001).

Liu, Y., E. Gomez, S. E. Maxwell, L. D. Turner, E. Tiesinga, and P. D. Lett. "Number fluctuations and energy dissipation in sodium spinor condensates." Phys. Rev. Lett. **102**, 225301 (2009a).

Liu, Y., S. Jung, S. E. Maxwell, L. D. Turner, E. Tiesinga, and P. D. Lett. "Quantum phase transitions and continuous observation of spinor dynamics in an antiferromagnetic condensate." Phys. Rev. Lett. **102**, 125301 (2009b).

Lu, Mingwu, Nathaniel Q. Burdick, Seo Ho Youn, and Benjamin L. Lev. "Strongly dipolar bose-einstein condensate of dysprosium." Phys. Rev. Lett. **107**, 190401 (2011).

Lysebo, M. and L. Veseth. "Feshbach resonances and transition rates for cold homonuclear collisions between ^{39}K and ^{41}K atoms." Phys. Rev. A **81**, 032702 (2010).

Mahmud, K. W. and E. Tiesinga. "Dynamics of spin-1 bosons in an optical lattice: Spin mixing, quantum-phase-revival spectroscopy, and effective three-body interactions." Phys. Rev. A **88**, 023602 (2013).

Markus Greiner, Tilman Esslinger Theodor W. Hänsch, Olaf Mandel and Immanuel Bloch. "Quantum phase transition from a superfluid to a mott insulator in a gas of ultracold atoms." Nature **415**, 39 (2002).

Marti, G. Edward, Ryan Olf, Enrico Vogt, Anton Öttl, and Dan M. Stamper-Kurn. "Two-element zeeman slower for rubidium and lithium." Phys. Rev. A **81**, 043424 (2010).

Matthews, M. R., D. S. Hall, D. S. Jin, J. R. Ensher, C. E. Wieman, E. A. Cornell, F. Dalfovo, C. Minniti, and S. Stringari. "Dynamical response of a bose-einstein condensate to a discontinuous change in internal state." Phys. Rev. Lett. **81**, 243–247 (1998).

McCarron, D. J., H. W. Cho, D. L. Jenkin, M. P. Köppinger, and S. L. Cornish. "Dual-species bose-einstein condensate of ^{87}Rb and ^{133}Cs." Phys. Rev. A **84**, 011603 (2011).

Metcalf, Harold J. and Peter van der Straten. *Laser Cooling and Trapping*. Graduate Texts in Contemporary Physics (Springer Science and Business Media, 1999).

Meyer, V., M. A. Rowe, D. Kielpinski, C. A. Sackett, W. M. Itano, C. Monroe, and D. J. Wineland. "Experimental demonstration of entanglement-enhanced rotation angle estimation using trapped ions." Phys. Rev. Lett. **86**, 5870–5873 (2001).

Miesner, H.-J., D. M. Stamper-Kurn, J. Stenger, S. Inouye, A. P. Chikkatur, and W. Ketterle. "Observation of metastable states in spinor bose-einstein condensates." Phys. Rev. Lett. **82**, 2228–2231 (1999).

Modugno, G., G. Ferrari, G. Roati, R. J. Brecha, A. Simoni, and M. Inguscio. "Bose-einstein condensation of potassium atoms by sympathetic cooling." Science **294**, 1320–1322 (2001).

Modugno, G., M. Modugno, F. Riboli, G. Roati, and M. Inguscio. "Two atomic species superfluid." Phys. Rev. Lett. **89**, 190404 (2002).

Monz, Thomas, Philipp Schindler, Julio T. Barreiro, Michael Chwalla, Daniel Nigg, William A. Coish, Maximilian Harlander, Wolfgang Hänsel, Markus Hennrich, and Rainer Blatt. "14-qubit entanglement: Creation and coherence." Phys. Rev. Lett. **106**, 130506 (2011).

Naik, Devang S. *Bose-Einstein Condensation: Building the Testbeds to Study Superfluidity.* Ph.D. thesis, Georgia Institute of Technology (2006).

Ohmi, Tetsuo and Kazushige Machida. “Bose-einstein condensation with internal degrees of freedom in alkali atom gases.” Journal of the Physical Society of Japan **67**, 1822–1825 (1998).

Pedersen, Poul L., Miroslav Gajdacz, Frank Deuretzbacher, Luis Santos, Carsten Klempt, Jacob F. Sherson, Andrew J. Hilliard, and Jan J. Arlt. “Spin dynamics in a two-dimensional quantum gas.” Phys. Rev. A **89**, 051603 (2014).

Phillips, William D. and Harold Metcalf. “Laser deceleration of an atomic beam.” Phys. Rev. Lett. **48**, 596–599 (1982).

Riedel, Max F., Pascal B ohi, Yun Li, Theodor W. H ansch, Alice Sinatra, and Philipp Treutlein. “Atom-chip-based generation of entanglement for quantum metrology.” Nature **464**, 1170–1173 (2010).

Roati, G., M. Zaccanti, C. D’Errico, J. Catani, M. Modugno, A. Simoni, M. Inguscio, and G. Modugno. “^{39}K bose-einstein condensate with tunable interactions.” Phys. Rev. Lett. **99**, 010403 (2007).

Sadler, L. E., J. M. Higbie, S. R. Leslie, M. Vengalattore, and D. M. Stamper-Kurn. “Spontaneous symmetry breaking in a quenched ferromagnetic spinor bose-einstein condensate.” Nature **443**, 312–315 (2006).

Santos, L., M. Fattori, J. Stuhler, and T. Pfau. “Spinor condensates with a laser-induced quadratic zeeman effect.” Phys. Rev. A **75**, 053606 (2007).

Schmaljohann, H., M. Erhard, J. Kronjäger, M. Kottke, S. van Staa, L. Cacciapuoti, J. J. Arlt, K. Bongs, and K. Sengstock. “Dynamics of $f = 2$ spinor bose-einstein condensates.” Phys. Rev. Lett. **92**, 040402 (2004).

Shen, C. and L.-M. Duan. “Efficient spin squeezing with optimized pulse sequences.” Phys. Rev. A **87**, 051801 (2013).

Stamper-Kurn, D. M., M. R. Andrews, A. P. Chikkatur, S. Inouye, H.-J. Miesner, J. Stenger, and W. Ketterle. “Optical confinement of a bose-einstein condensate.” Phys. Rev. Lett. **80**, 2027–2030 (1998).

Stamper-Kurn, Dan M. and Masahito Ueda. “Spinor bose gases: Symmetries, magnetism, and quantum dynamics.” Rev. Mod. Phys. **85**, 1191–1244 (2013).

Stellmer, Simon, Meng Khoon Tey, Rudolf Grimm, and Florian Schreck. “Bose-einstein condensation of ^{86}Sr.” Phys. Rev. A **82**, 041602 (2010).

Stellmer, Simon, Meng Khoon Tey, Bo Huang, Rudolf Grimm, and Florian Schreck. “Bose-einstein condensation of strontium.” Phys. Rev. Lett. **103**, 200401 (2009).

Stenger, J., S. Inouye, D. M. Stamper-Kurn, H.-J. Miesner, A. P. Chikkatur, and W. Ketterle. “Spin domains in ground-state bose-einstein condensates.” Nature **396**, 345–348 (1998).

Strecker, Kevin E., Guthrie B. Partridge, Andrew G. Truscott, and Randall G. Hulet. “Formation and propagation of matter-wave soliton trains.” Nature **417**, 150–153 (2002).

Takano, T., M. Fuyama, R. Namiki, and Y. Takahashi. “Spin squeezing of a cold atomic ensemble with the nuclear spin of one-half.” Phys. Rev. Lett. **102**, 033601 (2009).

Takasu, Yosuke, Kenichi Maki, Kaduki Komori, Tetsushi Takano, Kazuhito Honda, Mitsutaka Kumakura, Tsutomu Yabuzaki, and Yoshiro Takahashi. “Spin-singlet bose-einstein condensation of two-electron atoms.” Phys. Rev. Lett. **91**, 040404 (2003).

Thalhammer, G., G. Barontini, L. De Sarlo, J. Catani, F. Minardi, and M. Inguscio. “Double species bose-einstein condensate with tunable interspecies interactions.” Phys. Rev. Lett. **100**, 210402 (2008).

Tuchman, A. K., R. Long, G. Vrijsen, J. Boudet, J. Lee, and M. A. Kasevich. “Normal-mode splitting with large collective cooperativity.” Phys. Rev. A **74**, 053821 (2006).

van Kempen, E. G. M., S. J. J. M. F. Kokkelmans, D. J. Heinzen, and B. J. Verhaar.

"Interisotope determination of ultracold rubidium interactions from three high-precision experiments." Phys. Rev. Lett. **88**, 093201 (2002).

Wallis, H and W Ertmer. "Fokker-planck analysis of atomic beam cooling by frequency chirp methods." Journal of Physics B: Atomic, Molecular and Optical Physics **21**, 2999 (1988).

Weber, Tino, Jens Herbig, Michael Mark, Hanns-Christoph Ngerl, and Rudolf Grimm. "Bose-einstein condensation of cesium." Science **299**, 232–235 (2003).

Widera, Artur, Fabrice Gerbier, Simon Fölling, Tatjana Gericke, Olaf Mandel, and Immanuel Bloch. "Coherent collisional spin dynamics in optical lattices." Phys. Rev. Lett. **95**, 190405 (2005).

Widera, Artur, Fabrice Gerbier, Simon Fölling, Tatjana Gericke, Olaf Mandel, and Immanuel Bloch. "Precision measurement of spin-dependent interaction strengths for spin-1 and spin-2 87 rb atoms." New Journal of Physics **8**, 152 (2006).

Will, Sebastian, Thorsten Best, Ulrich Schneider, Lucia Hackermüller, Dirk-Sören Lühmann, and Immanuel Bloch. "Time-resolved observation of coherent multi-body interactions in quantum phase revivals." Nature **465**, 197–201 (2010).

Xu, K., Y. Liu, D. E. Miller, J. K. Chin, W. Setiawan, and W. Ketterle. "Observation of strong quantum depletion in a gaseous bose-einstein condensate." Phys. Rev. Lett. **96**, 180405 (2006).

yoon Choi, Jae, Woo Jin Kwon, Moonjoo Lee, Hyunseok Jeong, Kyungwon An, and Yong il Shin. "Imprinting skyrmion spin textures in spinor boseeinstein condensates." New Journal of Physics **14**, 053013 (2012).

Zhang, Wenxian, Su Yi, and Li You. "Mean field ground state of a spin-1 condensate in a magnetic field." New Journal of Physics **5**, 77 (2003).

Zhang, Wenxian, D. L. Zhou, M.-S. Chang, M. S. Chapman, and L. You. "Coherent spin mixing dynamics in a spin-1 atomic condensate." Phys. Rev. A **72**, 013602 (2005).

Zhao, L., J. Jiang, and Y. Liu. "Optimizing a spin-flip zeeman slower." arXiv:1401.7181 (2014a).

Zhao, L., J. Jiang, T. Tang, M. Webb, and Y. Liu. "Dynamics in spinor condensates tuned by a microwave dressing field." Phys. Rev. A **89**, 023608 (2014b).

Zhao, L., J. Jiang, T. Tang, M. Webb, and Y. Liu. "Antiferromagnetic spinor condensates in a two-dimensional optical lattice." Phys. Rev. Lett. **114**, 225302 (2015).

Zhu, M., C. W. Oates, and J. L. Hall. "Continuous high-flux monovelocity atomic beam based on a broadband laser-cooling technique." Phys. Rev. Lett. **67**, 46–49 (1991).

APPENDIX A

OPTIMIZING A SPIN-FLIP ZEEMAN SLOWER

This appendix includes a reprint of Ref. (Zhao *et al.*, 2014a): L. Zhao, J. Jiang, and Y. Liu, Optimizing a spin-flip Zeeman slower, arXiv:1401.7181.

Optimizing a spin-flip Zeeman slower

L. Zhao,* J. Jiang, and Y. Liu
Department of Physics, Oklahoma State University, Stillwater, OK 74078

We present a design of a spin-flip Zeeman slower controlled by a fast feedback circuit for a sodium Bose-Einstein condensate apparatus. We also demonstrate how the efficiency of the slower strongly depends on its intrinsic parameters, and compare these observations with a few theoretical models. Our findings lead to a simple three-step procedure of designing an optimal Zeeman slower for neutral atoms, especially for those atomic species with high initial velocities, such as sodium and lithium atoms.

PACS numbers: 020.3320, 020.7010, 020.7490, 020.0020

I. INTRODUCTION

Laser cooling and trapping neutral atoms with a magneto-optical trap (MOT) has become an important step in a successful production of ultracold quantum gases [1]. To improve the capture efficiency of a MOT, a number of slowers were invented to slow hot atoms before they overlap with the MOT [1–6]. Atoms and a resonant laser beam counter propagate in a slower. The longitudinal velocity and corresponding Doppler shift of these atoms decrease after they absorb resonant photons. After a few such absorptions, these slowed atoms are no longer resonant with the laser beam and thus cannot be further slowed down. In order to continuously slow atoms along the laser beam path, one can vary the laser frequency accordingly as with the frequency chirp method [7] or by using broadband lasers [8]. Another widely-used method is to compensate differences in the Doppler shift with a spatially varying magnetic field generated by a Zeeman slower while keeping the laser frequency unchanged [1, 3–5, 9–13]. In this paper, we present the design and construction of a spin-flip Zeeman slower controlled by a fast feedback circuit for a sodium Bose-Einstein condensate (BEC) apparatus. An efficient method of optimizing a slower with our simulation program and by monitoring the number of atoms trapped in the MOT is also explained. In addition, our data demonstrates how the efficiency of a slower strongly depends on a few of its intrinsic parameters, such as the intensity of the slowing laser beam and the length of each section in the slower. These findings result in a simple three-step procedure of designing an optimal Zeeman slower for neutral atoms, especially for those atomic species with high initial velocities, for example lithium atoms.

II. EXPERIMENTAL SETUP

A sodium beam is created by an oven consisting of a half nipple and an elbow flange. A double-sided flange with a 6 mm diameter hole in the center is used to collimate the atomic beam. To collect scattered atoms, a cold plate with a 9 mm diameter center hole is placed before a spin-flip Zeeman slower and kept at 10 °C with a Peltier cooler. Our multi-layer slower has three different sections along the x axis (i.e., a decreasing-field section, a spin-flip section, and an increasing-field section), as shown in Fig. 1(a). Compared with the single-layer Zeeman slower with variable pitch coils [11], this multilayer design provides us enormous flexibilities in creating large enough B for slowing atoms with high initial velocities (e.g., sodium and lithium atoms). The first section of our Zeeman slower produces a magnetic field with decreasing magnetic field strength B. We choose $B \sim 650$ Gauss at the entrance of the slower, so the slowing beam only needs to be red-detuned by δ of a few hundred MHz from the D2 line of ^{23}Na atoms. This frequency detuning is easily achieved with an acousto-optic modulator, but is still large enough to avoid perturbing the MOT. The spin-flip section is simply a bellow as to maintain $B = 0$ for atoms to be fully re-polarized and also to damp out mechanical vibrations generated by vacuum pumps. The increasing-field section creates a magnetic field with increasing B but in the opposite direction to that of the decreasing-field section, which ensures the magnetic field quickly dies off outside the slower. This slower can thus be placed close to the MOT, which results in more atoms being captured. The MOT setup is similar to that of our previous work [14] and its maximum capture velocity v_c is ~ 50 m/s.

To precisely adjust B inside the slower, all layers of magnetic coils are divided into four groups, and different layers in each group are connected in series and controlled by one fast feedback circuit. A standard ring-down circuit consisting of a resistor and a diode is also connected in parallel with each coil for safely shutting off the inductive current in the coil. An important chip in our control circuit is a high power metal oxide semiconductor field effect transistor (MOSFET) operated in the linear mode. We use a number of MOSFETs connected in parallel and mount them on the top of a water-cooled cold plate to efficiently cool them. A carefully chosen resistor R_s of 50 mΩ is connected to each MOSFET's source terminal to encourage equal current splitting among the MOSFETs in parallel. R_s also limits MOSFET's transcon-

---

* lichao@okstate.edu

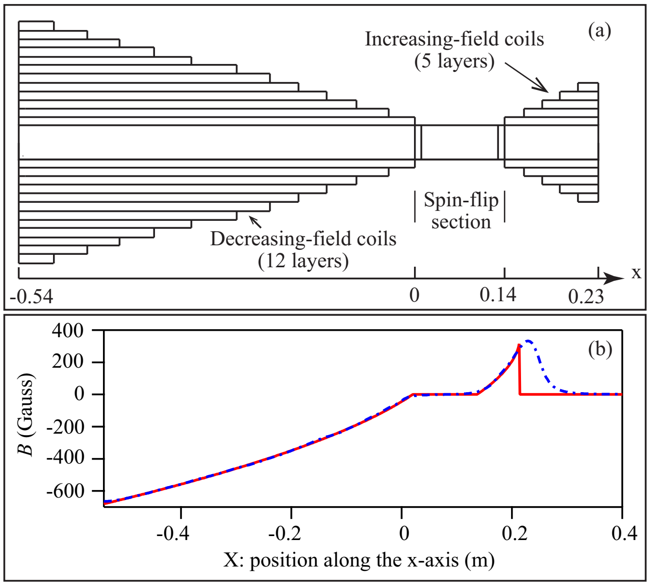

FIG. 1. (color online) (a) schematic of our spin-flip Zeeman slower. The first layer of the decreasing-field coils has 188 turns and its length is 0.54 m. The second layer is 0.51 m long and wrapped on the surface of the first layer. Similarly, the following layers are wrapped on the surface of its corresponding previous layer. The increasing-field section has five layers and is constructed in a similar way. All axes are not to scale. (b) A comparison between a theoretical prediction (solid red line) and the performance of our optimized Zeeman slower (dash-dotted blue line), with $\delta = -512$ MHz and η in decreasing- and increasing-field sections being set at 0.65. Atoms propagate along the positive x-axis direction. The MOT center locates at 0.45 m, where residual magnetic fields created by the slower are negligible.

ductance to a narrow range, which enables our feedback circuit to control both low and high electric currents with a single set of gains. The design of this feedback circuit is available upon request.

III. OPTIMIZATION

When neutral atoms pass through the Zeeman slower, only those atoms with a longitudinal velocity $v(x) = -[2\pi\delta + \mu B(x)/\hbar]/k$ are resonant with the slowing beam and can be slowed. Here μ is the magnetic moment, $\hbar$ is the reduced Planck's constant, k and δ are the wavevector and frequency detuning of the laser beam, respectively. The actual deceleration $a_s = \eta a_{\max}$ in the slower is thus given by

$$\frac{dB(x)}{dx} = -a_s \frac{\hbar k}{\mu v} = \eta a_{\max} \frac{\hbar k^2}{\mu[2\pi\delta + \mu B(x)/\hbar]} \ , \qquad (1)$$

where η is a safe factor to account for magnetic field imperfections in a given slower and the finite intensity of the slowing laser beam, and $a_{\max} = \hbar k \Gamma / 2m$ is the maximal achievable deceleration. m and Γ are the mass and the natural linewidth of the atoms, respectively.

Our largest MOT is achieved when we match $B(x)$ inside the slower as precisely as possible to a prediction derived from Eq. 1 with η being set at 0.65 in decreasing- and increasing-field sections and $v_f = 40$ m/s, as shown in Fig. 1(b). Here v_f is the velocity of atoms at the end of the slower. N, the number of atoms in a MOT, can also be boosted by a larger atomic flux with a hotter atomic oven. However, this is generally not a favorable method due to two reasons. First, a hotter oven generates atoms with higher initial average velocities, but a slower can only handle entering atoms of a certain maximum velocity. Second, alkali metals' consumption rates sharply increase with the oven temperature.

We find that convenient parameters to adjust are slowing beam's intensity I and frequency detuning δ, electric current i in each magnetic coil, and the length of each section of the slower. These parameters, however, cannot be optimized independently since there is a strong correlation among them. In order to efficiently optimize the slower, we developed a computer program to simulate $B(x)$ and compared the simulation results to the actual magnetic field strengths in the slower under many different conditions (e.g., at various values of i). The actual magnetic field strengths were measured with a precise Hall probe before the slower was connected to the vacuum apparatus. The agreements between the simulation results and the measurements are good, i.e., the discrepancies are < 5 %. This simulation program can thus mimic the actual performance of a Zeeman slower and provide a reasonable tuning range for each aforementioned parameter, which allows for efficiently optimizing the slower. Our simulation program is available upon request.

One common way to evaluate a slower's performance is from knowing the exact number of atoms whose velocities are smaller than $v_{\rm c}$ with a costly resonant laser. In the next four subsections, we show that a convenient detection method of optimizing a slower is to monitor the number of atoms captured in the MOT, i.e., more atoms trapped in a given MOT setup indicate a better performance of the slower.

A. Intensity of the slowing beam

Figure 2 shows that the MOT capture efficiency strongly depends on the slowing beam power P, i.e., N increases with P and then stays at its peak value $N_{\max}$ when P is higher than a critical value. This can be understood from the relationship between the safe factor η of a slower and the slowing beam intensity I. Based on Ref. [13], the safe factor $\eta_{\rm laser}$ at a finite I can be expressed as,

$$\eta_{\rm laser} = \frac{I/I_s}{1 + I/I_s + [\frac{2\pi\delta + \mu B/\hbar + kv}{\Gamma/2}]^2} \leq \eta_{\rm laser}^{\max} = \frac{I/I_s}{1 + I/I_s} \ , \qquad (2)$$

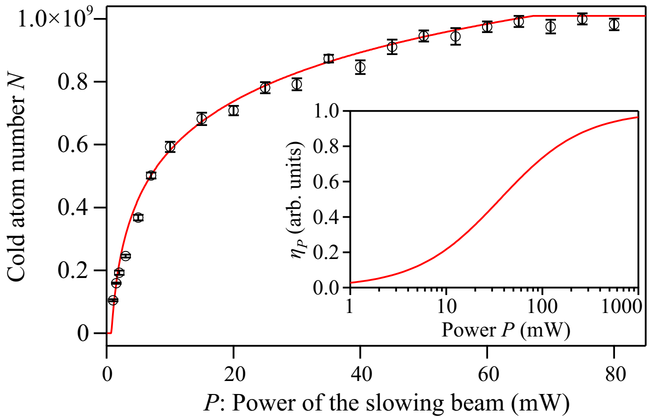

FIG. 2. (color online) N as a function of the slowing beam power P with 1 mW corresponding to $I_0/I_s = 2.5$. The solid line is a fit based on Eq. 3 with η in decreasing- and increasing-field sections being set at 0.65. Inset: η_p as a function of P for our apparatus.

where I_s is the saturation intensity of neutral atoms, e.g., it is 6.26 mW/cm^2 for sodium atoms. Eq. 2 implies that the safe factor of any optimal Zeeman slower has an upper limit, $\eta^{\max}_{\text{laser}}$, as long as the slowing beam intensity is fixed. In other words, a bigger η in the decreasing- or increasing-field section does not always lead to a more efficient Zeeman slower if I is given.

For a Gaussian slowing beam with a width W, its intensity I can be expressed as $I(r) = I_0 \cdot e^{-\frac{2r^2}{W^2}}$. Here r is the distance away from the slowing beam center and $I_0 = 2P/(\pi W^2)$ is the beam intensity at $r = 0$. N can be given by,

$$N(P) = \frac{N_{\max}}{\pi R_0^2}\int_0^{R_0} H\left[\eta^{\max}_{\text{laser}}(r) - \eta\right] 2\pi r dr$$
$$= \frac{N_{\max}}{R_0^2/2}\int_0^{R_0} H\left[\frac{P\cdot\exp(-\frac{2r^2}{W^2})}{\frac{\pi}{2}W^2 I_s + P\cdot\exp(-\frac{2r^2}{W^2})} - \eta\right] r dr \ . \quad (3)$$

Here $H[r]$ is a unit step function of r to account for the fact that atoms can be efficiently slowed only when $\eta \leq \eta^{\max}_{\text{laser}}(r)$, and R_0 is the radius of the atomic beam. Figure 2 shows that our data taken with $\eta = 0.65$ in decreasing- and increasing-field sections can be well fitted by Eq. 3 and N saturates at $P \geq 70$ mW. This indicates that 70 mW is the minimum power to achieve $\eta = 0.65$ for our apparatus. We can thus define a η_p, the preferred η in decreasing- and increasing-field sections at a given P, and derive its expression from Eq. 3 as follows,

$$\eta_p = P\cdot\exp(-\frac{2R_0^2}{W^2})/[\frac{\pi}{2}W^2 I_s + P\cdot\exp(-\frac{2R_0^2}{W^2})] \ . \quad (4)$$

The predicted η_p as a function of P for our apparatus is shown in the inset in Fig. 2, which implies P sharply increases with η_p and is infinitely large at $\eta_p = 1$. Therefore, the first step in designing an optimal Zeeman slower is to determine η_p from Eq. 4 based on the available slowing beam power.

B. The decreasing-field section

To focus on the decreasing-field section, our data shown in this subsection are taken with η being set at 0.65 in the increasing-field section, a fixed distance between the atomic oven and the MOT center to maintain a fixed solid angle for an atomic beam, $\delta = -512$ MHz, and $P = 70$ mW which implies η_p is 0.65. Based on the discussions in Refs. [3, 9], N can be expressed as

$$N = \int_0^{v_{\max}} N_0(v) f(v) dv \ , \quad (5)$$

where $N_0(v) \propto v^3 e^{-\frac{mv^2}{k_B T}}$ is the initial number of atoms created by the oven, k_B is the Boltzmann constant, and the oven temperature T is set at 530 K in this work. $f(v)$ is a correction factor to account for the transverse velocity distribution of slowed atoms after they absorb resonant photons in a Zeeman slower, which can be expressed as

$$f(v) = 1 - \exp\left[-\frac{r^2_{\text{mot}}}{(v_r v/3)L^2/v_f^2}\right] \ . \quad (6)$$

Here r_{mot} is the radius of a MOT, L is the distance between the MOT center and the end of a Zeeman slower, v_r is the recoil velocity of an atom in a slowing process, and $\sqrt{v_r v/3}$ is the transverse velocity of slowed atoms [9]. In Eq. 5, $v_{\max}$ is the maximum velocity of entering atoms which can be handled by a slower. For a spin-flip Zeeman slower, $v_{\max}$ is given by

$$v_{\max} = \sqrt{v_{\text{sf}}^2 + 2\eta_d \cdot a_{\max} \cdot L_d} \ , \quad (7)$$

where L_d and η_d are the length and the actual safe factor of the decreasing-field section, respectively. And $v_{\text{sf}} = 2\pi\delta/k$ is the velocity of atoms which are resonant with the slowing beam at the spin-flip section, since B is zero in this section. For example, v_{sf} is 302 m/s at $\delta = -512$ MHz in our sodium BEC apparatus.

For a given δ, Eqs. 5-7 predict that N should monotonically increase with $v_{\max}$, i.e., N increases with η_d at a fixed L_d (or N increases with L_d at a fixed η_d). However, our observations shown in Fig. 3(a) are drastically different from this prediction: at each L_d studied in this paper, N appears to first increase with η_d, reach its peak $N_{\max}$ at a critical value of η_d, and then decrease with η_d. Based on Eq. 7, we can also plot these data points as a function of $v_{\max}$, as shown in Fig. 3(b). At each value of L_d, the agreement between our data and a theoretical prediction derived from Eqs. 5-7 (dotted black line) can only be found when $v_{\max}$ is smaller than 800 m/s, which is approximately equal to the mean velocity ($\sqrt{9\pi k_B T/8m}$) of atoms entering our slower.

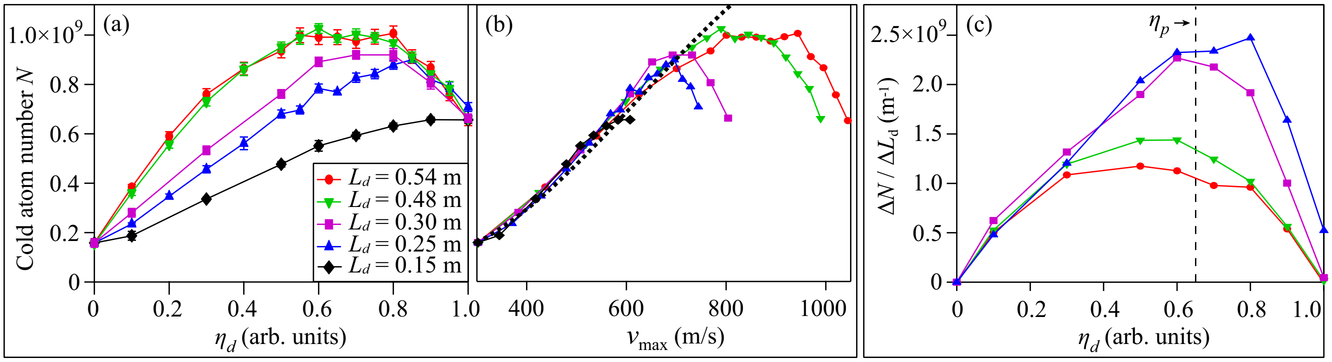

FIG. 3. (color online) N as a function of η_d (a) and $v_{\max}$ (b) with η being set at 0.65 in the increasing-field section, $\delta = -512$ MHz, and $P = 70$ mW. Dotted black line in Panel (b) is a fit based on Eqs. 5-7. (c) $\Delta N/\Delta L_d$ as a function of η_d. Here $\Delta L_d = L_d - 0.15$ m, and ΔN is the number of extra atoms being slowed when L_d is set at a value longer than 0.15 m. Black dashed line marks the position of η_p, which is determined by the slowing laser beam power.

In addition, we plot $\Delta N/\Delta L_d$ as a function of η_d in Fig. 3(c), where $\Delta N/\Delta L_d$ represents the number of extra atoms in the MOT gained from elongating the decreasing-field section by $\Delta L_d = L_d - 0.15$ m. Figure 3(c) shows that $\Delta N/\Delta L_d$ drops to a much smaller value when L_d is increased from 0.3 m to 0.48 m. This implies the ideal length of the decreasing-field section for our apparatus should be longer than 0.3 m and shorter than 0.48 m. It is worth noting that $\Delta N/\Delta L_d$ peaks at $\eta_d \sim 0.65$ for each value of L_d, as shown in Fig. 3(c). Interestingly, the predicted η_p from Eq. 4 is also 0.65 at $P = 70$ mW, and Fig. 3(a) shows $\eta_d \sim 0.65$ is also the position where the largest N occurs. This indicates that η of our optimized decreasing-field section is actually equal to η_p. Therefore, one important procedure in designing an optimal Zeeman slower is as follows: 1) find out η_p based on Eq. 4 from the available slowing beam intensity; 2) determine the length of the decreasing-field section from Eq. 7, i.e., $L_d = [9\pi k_B T/8m - (2\pi\delta/k)^2]/(2\eta_p a_{\max})$; 3) find out electric currents i of decreasing-field coils with our simulation program by precisely matching the simulated B to a prediction derived from Eq. 1.

C. The increasing-field section

The aforementioned discussion on the decreasing-field section applies to the increasing-field section as well. To only study the increasing-field section, data shown in this subsection are taken at $\eta_d = \eta_p = 0.65$, $L_d = 0.54$ m, and $P = 70$ mW.

Our data in Fig. 4(a) shows that N is not a monotonic function of i at a given δ. N first increases with i and reaches a peak at a critical value i_c, because a higher i leads to a larger deceleration which means more atoms can be slowed and captured in the MOT. When i is higher than i_c, we find that N sharply decreases with i due to atoms being over-slowed. Because $v_f = -(2\pi\delta + \mu B_{\mathrm{iMax}}/\hbar)/k$, the data points in Fig. 4(a) can be converted to reveal the relationship between N and v_f, as shown in Fig. 4(b). Here B_{iMax} is the maximum magnetic field strength created by the increasing-field section at a fixed i. We find four interesting results: N always peaks around $v_f = 40$ m/s $< v_c$ at any δ within the range of -450 MHz $\leq \delta \leq -650$ MHz; the minimal

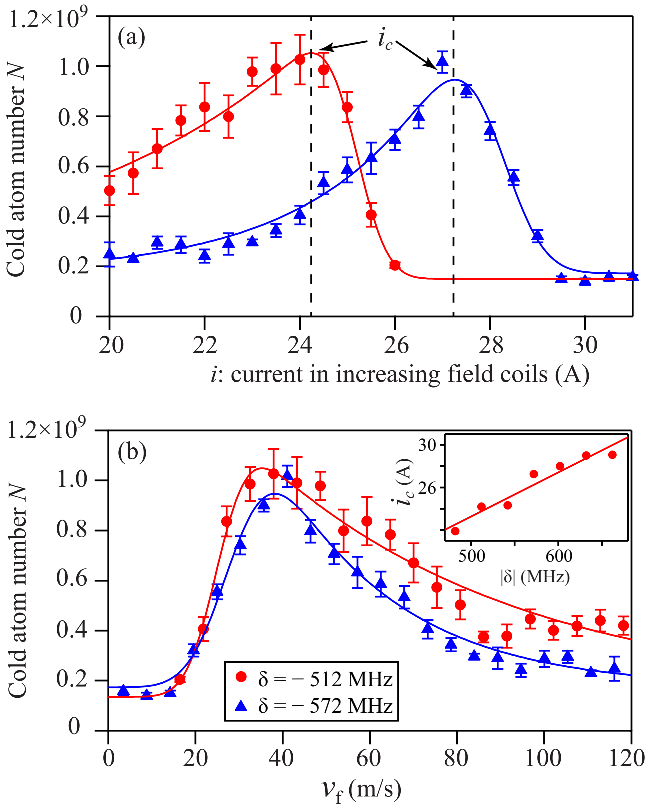

FIG. 4. (color online) N as a function of i (a) and v_{f} (b) at $\delta = -512$ MHz (red circles) and $\delta = -572$ MHz (blue triangles). i_c at a given δ is defined as the electric current at which N peaks. Solid lines are fits to guide the eye. Inset: i_c extracted from Panel(a) as a function of $|\delta|$. The solid line is a linear fit.

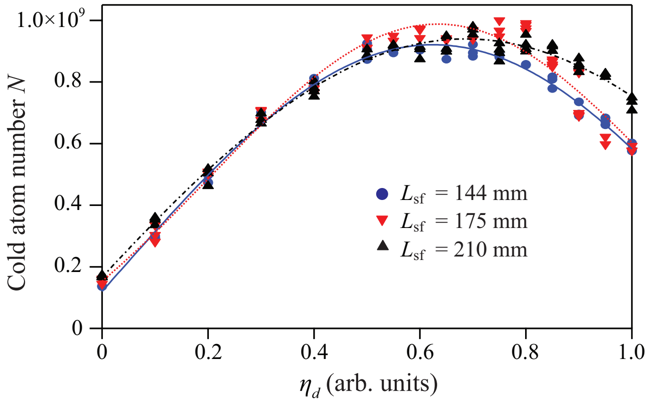

FIG. 5. (color online) N as a function of η_d at three different $L_{\rm sf}$, the length of the spin-flip section (see text). Lines are Gaussian fits to the data.

velocity of the atoms captured in the MOT appears to be ~ 20 m/s; the maximum value of N does not depend on δ; and i_c linearly increases with δ, as shown in Fig. 4. Therefore, in addition to the procedures listed in Sections 3.A and 3.B, another useful procedure in designing an optimal spin-flip Zeeman slower is as follows: 1) choose a convenient δ, for example, δ is around -500 MHz for sodium or lithium atoms; 2) find out the ideal length of the increasing-field section from the following equation, $L_i = (v_{\rm sf}^2 - v_c^2)/(2a_s) = [(2\pi\delta/k)^2 - v_c^2]/(2\eta_p a_{\rm max})$; 3) determine i_c from a figure similar to Fig. 4(a) and then set the current i at a value slightly smaller than i_c in the increasing-field coils.

D. The spin-flip section

We have also studied the contribution of the spin-flip section, but have not found a strong correlation between the slower's efficiency and $L_{\rm sf}$, the length of the spin-flip section. Figure 5 shows that N always peaks at $\eta_d \approx \eta_p = 0.65$ for three different values of $L_{\rm sf}$, when L_d is kept at 0.54 m, η is set at 0.65 in the increasing-field section, δ is -512 MHz, and P is 70 mW. This figure also implies that a longer spin-flip section does not boost the number of atoms captured in the MOT, as long as its length $L_{\rm sf}$ is sufficient to fully re-polarize atoms. A very long $L_{\rm sf}$, however, has a negative effect on the MOT capture efficiency, because it also unavoidably reduces the solid angle of the atomic beam when all other parameters of the system remain unchanged.

IV. CONCLUSIONS

We have presented the design and construction of a spin-flip Zeeman slower controlled by a fast feedback circuit, and demonstrated an efficient method to optimize a slower by using our simulation program and monitoring the number of atoms trapped in the MOT. Our data suggests that an optimal Zeeman slower may be designed with the following procedures: 1) determine η_p based on Eq. 4 from the available slowing beam intensity; 2) choose a convenient δ and find out the ideal lengths of the increasing- and decreasing-field sections from $L_i = [(2\pi\delta/k)^2 - v_c^2]/(2\eta_p a_{\rm max})$ and $L_d = [9\pi k_B T/8m - (2\pi\delta/k)^2]/(2\eta_p a_{\rm max})$, respectively; 3) set i at a value slightly smaller than i_c in the increasing-field coils and determine i of decreasing-field coils with our simulation program. We have found that a longer spin-flip section does not boost the number of atoms captured in the MOT, as long as its length $L_{\rm sf}$ is sufficient to fully re-polarize atoms. These conclusions are very useful in designing an optimal Zeeman slower for other atomic species, especially those with high initial velocities, for example lithium atoms.

V. ACKNOWLEDGMENTS

We thank Ian Spielman and Karl Nelson for insightful discussions, and Jared Austin and Micah Webb for experimental assistances. We also thank the U. S. Army Research Office, Oklahoma Center for the Advancement of Science and Technology, and Oak Ridge Associated Universities for financial support.

---

[1] H. Metcalf and P. Van Der Straten, *Laser Cooling and Trapping*, Graduate Texts in Contemporary Physics (Springer, 1999).
[2] W. Ketterle, K. B. Davis, M. A. Joffe, A. Martin, and D. E. Pritchard, "High densities of cold atoms in a dark spontaneous-force optical trap," Phys. Rev. Lett. **70**, 2253–2256 (1993).
[3] D. Durfee, "Dynamic properties of dilute bose-einstein condensation," Ph.D. thesis, Massachusetts Institute of Technology (1999).
[4] W. D. Phillips and H. Metcalf, "Laser deceleration of an atomic beam," Phys. Rev. Lett. **48**, 596–599 (1982).
[5] D. S. Naik, "Bose-einstein condensation: Building the testbeds to study superfluidity," Ph.D. thesis, Georgia Institute of Technology (2006).
[6] K. E. Gibble, S. Kasapi, and S. Chu, "Improved magneto-optic trapping in a vapor cell," Opt. Lett. **17**, 526–528 (1992).
[7] H. Wallis and W. Ertmer, "Fokker-planck analysis of atomic beam cooling by frequency chirp methods," Journal of Physics B: Atomic, Molecular and Optical Physics **21**, 2999 (1988).
[8] M. Zhu, C. W. Oates, and J. L. Hall, "Continuous high-flux monovelocity atomic beam based on a broad-

band laser-cooling technique," Phys. Rev. Lett. **67**, 46–49 (1991).

[9] G. E. Marti, R. Olf, E. Vogt, A. Öttl, and D. M. Stamper-Kurn, "Two-element zeeman slower for rubidium and lithium," Phys. Rev. A **81**, 043424 (2010).

[10] P. Cheiney, O. Carraz, D. Bartoszek-Bober, S. Faure, F. Vermersch, C. M. Fabre, G. L. Gattobigio, T. Lahaye, D. Guéry-Odelin, and R. Mathevet, "A zeeman slower design with permanent magnets in a halbach configuration," Review of Scientific Instruments **82**, 063115 (2011).

[11] S. C. Bell, M. Junker, M. Jasperse, L. D. Turner, Y.-J. Lin, I. B. Spielman, and R. E. Scholten, "A slow atom source using a collimated effusive oven and a single-layer variable pitch coil zeeman slower," Review of Scientific Instruments **81**, 013105 (2010).

[12] C. J. Dedman, J. Nes, T. M. Hanna, R. G. Dall, K. G. H. Baldwin, and A. G. Truscott, "Optimum design and construction of a zeeman slower for use with a magneto-optic trap," Review of Scientific Instruments **75**, 5136–5142 (2004).

[13] F. Lison, P. Schuh, D. Haubrich, and D. Meschede, "High-brilliance zeeman-slowed cesium atomic beam," Phys. Rev. A **61**, 013405 (1999).

[14] J. Jiang, L. Zhao, M. Webb, N. Jiang, H. Yang, and Y. Liu, "Simple and efficient all-optical production of spinor condensates," Phys. Rev. A **88**, 033620 (2013).

APPENDIX B

DYNAMICS IN SPINOR CONDENSATES TUNED BY A MICROWAVE DRESSING FIELD

This appendix includes a reprint of Ref. (Zhao *et al.*, 2014b): L. Zhao, J. Jiang, T. Tang, M. Webb, and Y. Liu, Dynamics in spinor condensates tuned by a microwave dressing field, Phys. Rev. A **89**, 023608 (2014).

PHYSICAL REVIEW A **89**, 023608 (2014)

Dynamics in spinor condensates tuned by a microwave dressing field

L. Zhao, J. Jiang, T. Tang, M. Webb, and Y. Liu[*]
Department of Physics, Oklahoma State University, Stillwater, Oklahoma 74078, USA

(Received 24 October 2013; revised manuscript received 16 December 2013; published 10 February 2014)

We experimentally study spin dynamics in a sodium antiferromagnetic spinor condensate as a result of spin-dependent interactions c and microwave dressing field interactions characterized by the net quadratic Zeeman effect q_{net}. In contrast to magnetic fields, microwave dressing fields enable us to access both negative and positive values of q_{net}. We find an experimental signature to determine the sign of q_{net} and observe harmonic spin population oscillations at every q_{net} except near each separatrix in phase space where spin oscillation period diverges. No spin domains and spatial modes are observed in our system. Our data in the negative q_{net} region exactly resembles what is predicted to occur in a ferromagnetic spinor condensate in the positive q_{net} region. This observation agrees with an important prediction derived from the mean-field theory: spin dynamics in spin-1 condensates substantially depends on the sign of q_{net}/c. This work uses only one atomic species to reveal mean-field spin dynamics, especially the remarkably different relationship between each separatrix and the magnetization, of spin-1 antiferromagnetic and ferromagnetic spinor condensates.

DOI: 10.1103/PhysRevA.89.023608 PACS number(s): 67.85.Hj, 32.60.+i, 03.75.Kk, 03.75.Mn

I. INTRODUCTION

An atomic Bose-Einstein condensate (BEC) is a state where all atoms have a single collective wave function for their spatial degrees of freedom. The key benefit of spinor BECs is the additional spin degree of freedom. Together with Feshbach resonances and optical lattices which tune the interatomic interactions, spinor BECs constitute a fascinating collective quantum system offering an unprecedented degree of control over such parameters as spin, temperature, and the dimensionality of the system [1,2]. Spinor BECs have become one of the fastest-moving research frontiers in the past 15 years. A number of atomic species have proven to be perfect candidates in the study of spinor BECs, such as $F = 1$ and $F = 2$ hyperfine spin states of ^{87}Rb atoms [1–7] and $F = 1$ hyperfine spin manifolds of ^{23}Na atoms [8–12]. Many interesting phenomena due to the interconversion among multiple spin states and magnetic field interactions have been experimentally demonstrated in spinor BECs, such as spin population dynamics [1–9], quantum number fluctuation [10,13], various quantum phase transitions [1,9,11,12], and quantum spin-nematic squeezing [14]. Spinor BEC systems have been successfully described with a classical two-dimensional phase space [1,2,15–17], a rotor model [18], or a quantum model [13,17].

In this paper, we experimentally study spin-mixing dynamics in a $F = 1$ sodium spinor condensate starting from a nonequilibrium initial state, driven by the net quadratic Zeeman energy $q_{\mathrm{net}} = q_M + q_B$ and antiferromagnetic spin-dependent interactions c. Here q_B and q_M are the quadratic Zeeman shifts induced by magnetic fields and microwave dressing fields, respectively. The spin-dependent interaction energy c is proportional to the mean BEC density and the difference in the $f = 0$ and $f = 2$ s-wave scattering lengths, where f is the summed spin angular momentum in a collision. It is well known that $c > 0$ (or $c < 0$) in $F = 1$ antiferromagnetic ^{23}Na (or ferromagnetic ^{87}Rb) spinor BECs. In contrast to a magnetic field, a microwave dressing field enables us to access both negative and positive values of q_{net}. A method to characterize microwave dressing fields and an approach to adiabatically sweep q_{net} from $-\infty$ to $+\infty$ are also explained. In both negative and positive q_{net} regions, we observe spin population oscillations resulting from coherent collisional interconversion among two $|F = 1, m_F = 0\rangle$ atoms, one $|F = 1, m_F = +1\rangle$ atom, and one $|F = 1, m_F = -1\rangle$ atom. In every spin oscillation studied in this paper, our data show that the population of the $m_F = 0$ state averaged over time is always larger (or smaller) than its initial value as long as $q_{\mathrm{net}} < 0$ (or $q_{\mathrm{net}} > 0$). This observation provides a clear experimental signature to determine the sign of q_{net}. We also find a remarkably different relationship between the total magnetization m and a separatrix in phase space where spin oscillation period diverges: The position of the separatrix moves slightly with m in the positive q_{net} region, while the separatrix quickly disappears when m is away from zero in the negative q_{net} region. Our data agree with an important prediction derived by Ref. [17]: The spin-mixing dynamics in $F = 1$ spinor condensates substantially depends on the sign of $R = q_{\mathrm{net}}/c$. This work uses only one atomic species to reveal mean-field spin dynamics, especially the relationship between each separatrix and the magnetization, which are predicted to appear differently in $F = 1$ antiferromagnetic and ferromagnetic spinor condensates.

Because no spin domains and spatial modes are observed in our system, the single spatial mode approximation (SMA), in which all spin states have the same spatial wave function, appears to be a proper theoretical model to understand our data. Similarly to Refs. [1,16], we take into account the conservation of the total atom number and the total magnetization m. Spin-mixing dynamics in a $F = 1$ spinor BEC can thus be described with a two-dimensional (ρ_0 versus θ) phase space, where the fractional population ρ_{m_F} and the phase θ_{m_F} of each m_F state are independent of position. The BEC energy E and the time evolution of ρ_0 and θ may be expressed as [1,16]

$$\begin{aligned} E &= q_{\mathrm{net}}(1-\rho_0) \\ &\quad + c\rho_0[(1-\rho_0) + \sqrt{(1-\rho_0)^2 - m^2}\cos\theta], \\ \dot{\rho}_0 &= -(2/\hbar)\partial E/\partial\theta, \dot{\theta} = (2/\hbar)\partial E/\partial\rho_0. \end{aligned} \tag{1}$$

---

[*] yingmei.liu@okstate.edu

Here $\theta = \theta_{+1} + \theta_{-1} - 2\theta_0$ is the relative phase among the three m_F spin states and $\hbar$ is the reduced Planck constant. The induced linear Zeeman shift remains the same during the collisional spin interconversion and is thus ignored. The total magnetization is $m = \rho_{+1} - \rho_{-1}$. Spin dynamics in $F = 1$ antiferromagnetic and ferromagnetic spinor BECs have been studied in magnetic fields where $q_{\rm net} = q_B \propto B^2 > 0$ with ^{23}Na and ^{87}Rb atoms, respectively [1]. A few methods have been explored for generating a negative quadratic Zeeman shift, such as via a microwave dressing field [1,11,19–21] or through a linearly polarized off-resonant laser beam [22]. In this paper, we choose the first method.

II. EXPERIMENTAL SETUP

The experimental setup is similar to that illustrated in our previous work [23]. Hot ^{23}Na atoms are slowed by a spin-flip Zeeman slower, captured in a standard magneto-optical trap, cooled through a polarization gradient cooling process to 40 μK, and loaded into a crossed optical dipole trap originating from a linearly polarized high-power infrared laser at 1064 nm. After an optimized 6-s forced evaporative cooling process, a pure $F = 1$ BEC of 1.0×10^5 sodium atoms is created. The spin healing length and the Thomas-Fermi radii of a typical condensate studied in this paper are 13 μm and (6.1, 6.1, 4.3) μm, respectively. We can polarize atoms in the $F = 1$ BEC fully to the $|F = 1, m_F = -1\rangle$ state by applying a weak magnetic field gradient during the first half of the forced evaporation (or fully to the $|F = 1, m_F = 0\rangle$ state by adding a very strong magnetic bias field during the entire 6-s forced evaporation). We then ramp up a small magnetic bias field with its strength B being 271.5(4) mG, while turning off the field gradient. An rf-pulse resonant with the linear Zeeman splitting is applied to prepare an initial state with any desired combination of the three m_F states, which is followed by abruptly switching on an off-resonant microwave pulse to generate a proper microwave dressing field. To create sufficiently large $q_{\rm net}$, a microwave antenna designed for a frequency near the $|F = 1\rangle \leftrightarrow |F = 2\rangle$ transition is placed a few inches above the center of the magneto-optical trap and connected to a function generator outputting a maximum power of 10 W. The actual power used in this paper is ~8 W. After various hold times t in the optical dipole trap, the microwave dressing fields are quickly turned off. Populations of the multiple spin states are then measured via the standard absorption imaging preceded by a 3-ms Stern-Gerlach separation and a 7-ms time of flight.

The exact value of $q_{\rm net}$ is carefully calibrated from a few experimental parameters, such as the polarization and frequency of a microwave pulse. Similarly to Refs. [19,21], we express the value of $q_{\rm net}$ as

$$q_{\rm net} = q_{\rm B} + q_{\rm M} = aB^2h + \frac{\delta E|_{m_F=1} + \delta E|_{m_F=-1} - 2\delta E|_{m_F=0}}{2},$$

$$\delta E|_{m_F} = \frac{h}{4}\sum_{k=0,\pm1}\frac{\Omega^2_{m_F,m_F+k}}{\Delta_{m_F,m_F+k}} = \frac{h}{4}\sum_{k=0,\pm1}\frac{\Omega^2_{m_F,m_F+k}}{\Delta - [(m_F+k)/2 - (-m_F/2)]\mu_B B}, \quad (2)$$

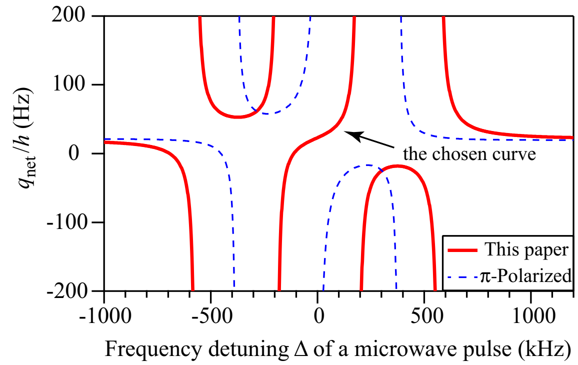

FIG. 1. (Color online) $q_{\rm net}$ as a function of Δ. The residual magnetic field is $B = 271.5(4)$ mG. Dashed blue lines represent the predictions derived from Eq. (2) when the microwave pulse is purely π polarized and its corresponding on-resonance Rabi frequencies are $\Omega_{-1,-2} = \Omega_{0,-1} = \Omega_{1,0} = \Omega_{-1,0} = \Omega_{0,1} = \Omega_{1,2} = 0$, $\Omega_{-1,-1} = \Omega_{1,1} = 4.2$ kHz, and $\Omega_{0,0} = 4.9$ kHz. Solid red lines represent the predictions from Eq. (2) for a typical microwave pulse used in this paper. The specially chosen polarization of this pulse yields nine on-resonance Rabi frequencies as follows: $\Omega_{-1,-2} = 5.1$ kHz, $\Omega_{0,-1} = 3.6$ kHz, and $\Omega_{1,0} = 2.1$ kHz are from the σ^--polarized component of the pulse; $\Omega_{-1,-1} = \Omega_{0,0} = \Omega_{1,1} = 0$ are from the π-polarized component of the pulse; and $\Omega_{-1,0} = 2.3$ kHz, $\Omega_{0,1} = 3.9$ kHz, and $\Omega_{1,2} = 5.5$ kHz are from the σ^+-polarized component of the pulse (see text). In this paper, Δ is tuned within the range of -190 kHz to 190 kHz from the $|F = 1, m_F = 0\rangle \leftrightarrow |F = 2, m_F = 0\rangle$ transition.

where $a \approx 277$ Hz/G^2 (or $a \approx 71$ Hz/G^2) for $F = 1$ ^{23}Na (or ^{87}Rb) atoms, the microwave pulse is detuned by Δ from the $|F = 1, m_F = 0\rangle \leftrightarrow |F = 2, m_F = 0\rangle$ transition, and h is the Planck constant. We define k as 0 or ±1 for a π- or a $\sigma^\pm$-polarized microwave pulse, respectively. For a given polarization k, the allowed transition is $|F = 1, m_F\rangle \leftrightarrow |F = 2, m_F + k\rangle$ and its on-resonance Rabi frequency is $\Omega_{m_F,m_F+k} \propto \sqrt{I_k}C_{m_F,m_F+k}$, where C_{m_F,m_F+k} is the Clebsch-Gordan coefficient of the transition and I_k is the intensity of this purely polarized microwave pulse. We also define $\Delta_{m_F,m_F+k} = \Delta - [(m_F + k)/2 - (-m_F/2)]\mu_B B$ as the frequency detuning of the microwave pulse with respect to the $|F = 1, m_F\rangle \rightarrow |F = 2, m_F + k\rangle$ transition, where μ_B is the Bohr magneton.

A purely π-polarized microwave pulse has been a popular choice in some publications [1,20,21]. However, we apply microwave pulses of a specially chosen polarization, in order to continuously scan $q_{\rm net}$ from large negative values to big positive values at a moderate microwave power. Figure 1 compares microwave dressing fields induced by a typical microwave pulse used in this paper and a purely π-polarized microwave pulse. This comparison clearly shows that it is possible to continuously or adiabatically sweep $q_{\rm net}$ from $-\infty$ to $+\infty$ simply by continuously tuning Δ from -190 kHz to 190 kHz with our specially chosen microwave pulses at a power of 8 W. Another advantage of choosing such microwave pulses is to conveniently place the microwave antenna on our apparatus without blocking optical components. To ensure an accurate calibration of $q_{\rm net}$ based on Eq. (2), we measure the nine on-resonance Rabi frequencies Ω daily through monitoring the number of atoms excited by a resonant microwave pulse

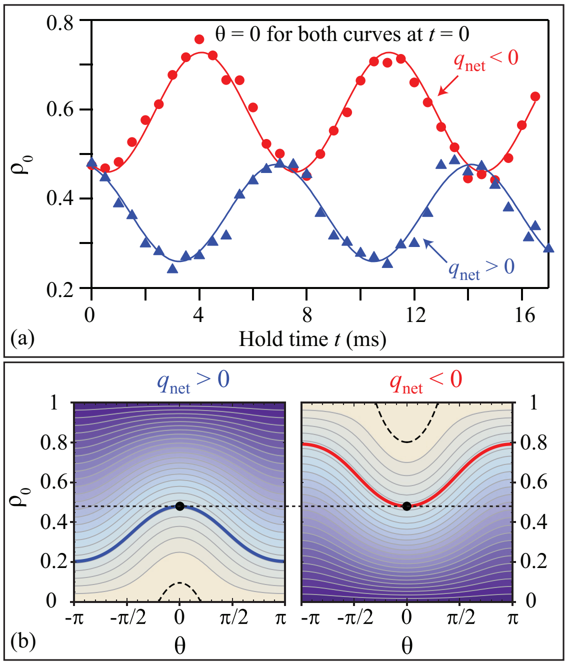

FIG. 2. (Color online) (a) Time evolutions of ρ_0 at $q_{\rm net}/h = +93\text{Hz} > 0$ (solid blue triangles) and $q_{\rm net}/h = -83$ Hz < 0 (solid red circles) with $m = 0$ and $c/h = 52(1)$ Hz. It is important to note that the two curves start from the same initial state with $\theta|_{t=0} = 0$. Solid lines are sinusoidal fits to the data. (b) Equal-energy contour plots based on Eq. (1) for the two experimental conditions shown in Fig. 2(a), i.e., $q_{\rm net} > 0$ (left) and $q_{\rm net} < 0$ (right). The heavy solid blue and red lines represent the energy of the above two experimental conditions, respectively. The dotted black horizontal line is to emphasize the fact that the above two experiments start with the same initial state which is marked by the solid black circles. Dashed black lines represent the energy of the separatrix between the running and oscillatory phase solutions. Darker colors correspond to lower energies.

to the $F = 2$ state as a function of the pulse duration. A typical example of the Rabi frequency measurement is shown in Fig. 3(a). We find that uncertainties of Ω and $q_{\rm net}$ are ~2% and ~5%, respectively.

III. DYNAMICS OF SPINOR CONDENSATES IN MICROWAVE DRESSING FIELDS

We observe spin oscillations at every given value of $q_{\rm net}$ within a wide range, i.e., $-240\text{ Hz} \leqslant q_{\rm net}/h \leqslant 240$ Hz. Typical time evolutions of ρ_0 starting with the same nonequilibrium initial state at a negative and a positive $q_{\rm net}$ are shown in Fig. 2(a). We find that these evolutions can be well fit by sinusoidal functions of the similar oscillation period T and amplitude A. Note that the hold time t is kept between zero and $2T < 100$ ms, in order to ensure accurate measurements of spin dynamics and avoid significant atom losses due to the presence of off-resonant microwave pulses. On the other hand, our data in Fig. 2(a) show that the value of $\langle\rho_0\rangle$ drastically differs in the two spin oscillations: $\langle\rho_0\rangle > \rho_0|_{t=0}$ as long as $q_{\rm net} < 0$, while $\langle\rho_0\rangle < \rho_0|_{t=0}$ if $q_{\rm net} > 0$. Here $\langle\rho_0\rangle$ is the average value of ρ_0 over time in a spin oscillation and $\rho_0|_{t=0}$ is the initial value of ρ_0. This phenomenon is observed at every value of $q_{\rm net}$ when spin oscillations start with the same initial state, although the period T and amplitude A change with $q_{\rm net}$. The above observations agree well with predictions from the mean-field SMA theory [i.e., Eq. (1)] as shown by the heavy solid lines in Fig. 2(b): ρ_0 is limited between $(\rho_0|_{t=0} - 2A)$ and $\rho_0|_{t=0}$ at $q_{\rm net} > 0$, while it is restricted between $\rho_0|_{t=0}$ and $(\rho_0|_{t=0} + 2A)$ at $q_{\rm net} < 0$. We can thus use the phenomenon to conveniently determine the sign of $q_{\rm net}$, i.e., by comparing the value of $\langle\rho_0\rangle$ of a spin oscillation to the value of $\rho_0|_{t=0}$.

The value of T as a function of $q_{\rm net}$ is then plotted in Fig. 3 for $m = 0$ and $m = 0.2$, which demonstrates two interesting results. First, when $m = 0$, the spin oscillation is harmonic except near the critical values (i.e., $q_{\rm net}/h = \pm 52$ Hz) where the period diverges. This agrees with the predictions derived from Eq. (1), as shown by the dotted red line in Fig. 3. The energy contour $E_{\rm sep}$ where the oscillation becomes anharmonic is defined as a separatrix in phase space. A point on the separatrix satisfies the equation $\dot{\rho}_0 = \dot{\theta} = 0$ according to the mean-field SMA theory. In fact, for our sodium system with $c > 0$, $E_{\rm sep} = q_{\rm net}$ for $q_{\rm net} > 0$, while $E_{\rm sep} = 0$ at $m = 0$ for $q_{\rm net} < 0$. Figure 3 shows that the T versus $q_{\rm net}$ curve is symmetric with respect to the $q_{\rm net} = 0$ axis at $m = 0$. The period T decreases rapidly with increasing $|q_{\rm net}|$ when $|q_{\rm net}|$ is large, which corresponds to the "Zeeman regime" with running phase solutions. In the opposite limit, the period only weakly depends on $|q_{\rm net}|$, which represents the "interaction regime" with oscillatory phase solutions. Here $|q_{\rm net}|$ is the absolute value of $q_{\rm net}$. The value of θ is (or is not) restricted in the regions with oscillatory (or running) phase solutions. References [8,9] reported observations of the similar phenomena for $q_{\rm net} > 0$ with a $F = 1$ antiferromagnetic spinor condensate; however, they did not access the negative $q_{\rm net}$ region.

Figure 3 also demonstrates a remarkably different relationship between the total magnetization m and the separatrix in phase space: the position of the separatrix moves slightly with m in the positive $q_{\rm net}$ region, while the separatrix quickly disappears when m is away from zero in the negative $q_{\rm net}$ region. Good agreements between our data and the mean-field SMA theory are shown in the inset [Fig. 3(b)] and the main figure in Fig. 3. Interestingly, we find that the spin dynamics which appear in our antiferromagnetic sodium system in the negative $q_{\rm net}$ region exactly resembles what is predicted to occur in a ferromagnetic spinor condensate in the positive $q_{\rm net}$ region [16,17]. Note that $R = q_{\rm net}/c$ is negative in both of these two cases. This observation agrees with an important prediction made by Ref. [17]: The spin-mixing dynamics in $F = 1$ spinor condensates substantially depends on the sign of R. As a matter of fact, our results in the negative $q_{\rm net}$ region are similar to those reported with a $F = 1$ ferromagnetic ^{87}Rb spinor condensate in magnetic fields where $q_{\rm net} > 0$ [1,3]. It is worth noting that our data in Fig. 3 may also be extrapolated to understand the relationship between the separatrix and m in the ferromagnetic Rb system, although this relationship has not been experimentally explored yet. This paper may thus be the first to use only one atomic species to reveal mean-field spin dynamics, especially the different relationship between each separatrix and the magnetization of $F = 1$ antiferromagnetic and ferromagnetic spinor condensates.

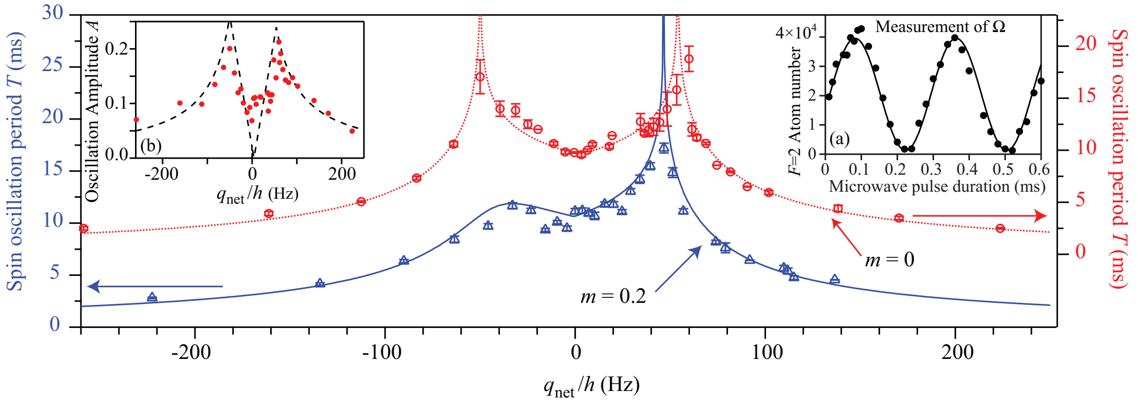

FIG. 3. (Color online) The spin oscillation period as a function of $q_{\rm net}$ for $m = 0$ (open red circles) and $m = 0.2$ (open blue triangles). The lines are fits based on Eq. (1), which yield the following fit parameters: $\rho_0|_{t=0} = 0.48$, $\theta|_{t=0} = 0$, and $c/h = 52(1)$ Hz for $m = 0$ and $\rho_0|_{t=0} = 0.48$, $\theta|_{t=0} = 0$, and $c/h = 47(1)$ Hz for $m = 0.2$. The fit parameters are within the 5% uncertainty of our measurements. Note the different scales of the left and right vertical axes. Inset (a): The number of $F = 2$ atoms excited by a resonant microwave pulse as a function of the pulse duration. The solid line is a sinusoidal fit to extract the on-resonance Rabi frequency Ω of the pulse. Inset (b): Amplitudes A of spin oscillations shown in the main figure as a function of $q_{\rm net}$ at $m = 0$. The dashed black line is a fit based on Eq. (1) with the same set of fit parameters as that applied in the main figure.

IV. CONCLUSION

In conclusion, we have experimentally studied spin dynamics of a sodium spinor condensate in a microwave dressing field. In both negative and positive $q_{\rm net}$ regions, we have observed harmonic spin oscillations and found that the sign of $q_{\rm net}$ can be determined by comparing $\langle\rho_0\rangle$ to $\rho_0|_{t=0}$. Our data also demonstrate that the position of the separatrix in phase space moves slightly with m in the positive $q_{\rm net}$ region, while the separatrix quickly disappears when m is away from zero in the negative $q_{\rm net}$ region. Our data can be well fit by the mean-field theory and agree with one of its important predictions: The spin-mixing dynamics in $F = 1$ spinor condensates substantially depends on the sign of $R = q_{\rm net}/c$. This work uses only one atomic species to reveal mean-field spin dynamics and the different dependence of each separatrix on m in $F = 1$ antiferromagnetic and ferromagnetic spinor condensates. In addition, microwave pulses used in this paper can be applied to cancel out stray magnetic fields and adiabatically sweep $q_{\rm net}$ from $-\infty$ to $+\infty$. This allows studies on interesting but unexplored phenomena at $q_{\rm net} = 0$, for example, realizing a maximally entangled Dicke state with antiferromagnetic spinor condensates through quantum phase transitions [24].

ACKNOWLEDGMENTS

We thank the Army Research Office, Oklahoma Center for the Advancement of Science and Technology, and Oak Ridge Associated Universities for financial support. M.W. thanks the Niblack Research Scholar program.

---

[1] D. M. Stamper-Kurn and M. Ueda, Rev. Mod. Phys. **85**, 1191 (2013).
[2] Y. Kawaguchi and M. Ueda, Phys. Rep. **520**, 253 (2012).
[3] M.-S. Chang, Q. Qin, W. Zhang, L. You, and M. S. Chapman, Nat. Phys. **1**, 111 (2005).
[4] A. Widera, F. Gerbier, S. Fölling, T. Gericke, O. Mandel, and I. Bloch, New J. Phys. **8**, 152 (2006).
[5] J. Kronjäger, C. Becker, P. Navez, K. Bongs, and K. Sengstock, Phys. Rev. Lett. **97**, 110404 (2006).
[6] H. Schmaljohann, M. Erhard, J. Kronjäger, M. Kottke, S. van Staa, L. Cacciapuoti, J. J. Arlt, K. Bongs, and K. Sengstock, Phys. Rev. Lett. **92**, 040402 (2004).
[7] T. Kuwamoto, K. Araki, T. Eno, and T. Hirano, Phys. Rev. A **69**, 063604 (2004).
[8] A. T. Black, E. Gomez, L. D. Turner, S. Jung, and P. D. Lett, Phys. Rev. Lett. **99**, 070403 (2007).
[9] Y. Liu, S. Jung, S. E. Maxwell, L. D. Turner, E. Tiesinga, and P. D. Lett, Phys. Rev. Lett. **102**, 125301 (2009).
[10] Y. Liu, E. Gomez, S. E. Maxwell, L. D. Turner, E. Tiesinga, and P. D. Lett, Phys. Rev. Lett. **102**, 225301 (2009).
[11] E. M. Bookjans, A. Vinit, and C. Raman, Phys. Rev. Lett. **107**, 195306 (2011).
[12] D. Jacob, L. Shao, V. Corre, T. Zibold, L. De Sarlo, E. Mimoun, J. Dalibard, and F. Gerbier, Phys. Rev. A **86**, 061601 (2012).
[13] L. Chang, Q. Zhai, R. Lu, and L. You, Phys. Rev. Lett. **99**, 080402 (2007).
[14] C. D. Hamley, C. S. Gerving, T. M. Hoang, E. M. Bookjans, and M. S. Chapman, Nature Physics **8**, 305 (2012).
[15] W. Zhang, S. Yi, and L. You, New J. Phys. **5**, 77 (2003).
[16] W. Zhang, D. L. Zhou, M.-S. Chang, M. S. Chapman, and L. You, Phys. Rev. A **72**, 013602 (2005).
[17] A. Lamacraft, Phys. Rev. A **83**, 033605 (2011).
[18] R. Barnett, J. D. Sau, and S. Das Sarma, Phys. Rev. A **82**, 031602 (2010).

[19] F. Gerbier, A. Widera, S. Fölling, O. Mandel, and I. Bloch, Phys. Rev. A **73**, 041602(R) (2006).

[20] S. R. Leslie, J. Guzman, M. Vengalattore, J. D. Sau, M. L. Cohen, and D. M. Stamper-Kurn, Phys. Rev. A **79**, 043631 (2009).

[21] Sabrina R. A. Leslie, Ph.D. thesis, University of California, Berkeley, 2008.

[22] L. Santos, M. Fattori, J. Stuhler, and T. Pfau, Phys. Rev. A **75**, 053606 (2007).

[23] J. Jiang, L. Zhao, M. Webb, N. Jiang, H. Yang, and Y. Liu, Phys. Rev. A **88**, 033620 (2013).

[24] Z. Zhang and L.-M. Duan, Phys. Rev. Lett. **111**, 180401 (2013).

APPENDIX C

ANTIFERROMAGNETIC SPINOR CONDENSATES IN A TWO-DIMENSIONAL OPTICAL LATTICE

This appendix includes a reprint of Ref. (Zhao *et al.*, 2015): L. Zhao, J. Jiang, T. Tang, M. Webb, and Y. Liu, Antiferromagnetic Spinor Condensates in a Two-Dimensional Optical Lattice, Phys. Rev. Lett. **114**, 225302 (2015).

Antiferromagnetic Spinor Condensates in a Two-Dimensional Optical Lattice

L. Zhao, J. Jiang, T. Tang, M. Webb, and Y. Liu[*]
Department of Physics, Oklahoma State University, Stillwater, Oklahoma 74078, USA

(Received 30 December 2014; published 4 June 2015)

We experimentally demonstrate that spin dynamics and the phase diagram of spinor condensates can be conveniently tuned by a two-dimensional optical lattice. Spin population oscillations and a lattice-tuned separatrix in phase space are observed in every lattice where a substantial superfluid fraction exists. In a sufficiently deep lattice, we observe a phase transition from a longitudinal polar phase to a broken-axisymmetry phase in steady states of lattice-confined spinor condensates. The steady states are found to depend sigmoidally on the lattice depth and exponentially on the magnetic field. We also introduce a phenomenological model that semiquantitatively describes our data without adjustable parameters.

DOI: 10.1103/PhysRevLett.114.225302 PACS numbers: 67.85.Fg, 03.75.Kk, 03.75.Mn, 05.30.Rt

A spinor Bose-Einstein condensate (BEC) confined in optical lattices has attracted much attention for its abilities to systematically study, verify, and optimize condensed matter models [1–3]. An optical lattice is a versatile technique to enhance interatomic interactions and control the mobility of atoms [4–6]. Atoms held in shallow lattices can tunnel freely among lattice sites and form a superfluid (SF) phase. The tunneling rate is suppressed while the on-site atom-atom interaction increases in deeper lattices. This may result in a transition from a SF phase to a Mott-insulator (MI) phase at a critical lattice depth, which has been confirmed in various scalar BEC systems [4–7]. In contrast to scalar BECs, spinor BECs have unique advantages due to an additional spin degree of freedom. The predicted SF-MI phase transition is remarkably different in lattice-trapped antiferromagnetic spinor BECs; i.e., the transition may be first (second) order around the tip of each Mott lobe for an even (odd) occupation number [1,8].

Spin-mixing dynamics and phase diagrams of spinor BECs in free space, due to the interplay of the spin-dependent interaction U_2 and the quadratic Zeeman energy q_B, have been well studied using sodium [9–16] and rubidium atoms [17–20]. Known phenomena in spin-1 spinor BECs include spin population oscillations resulting from coherent interconversions among two $|F=1, m_F=0\rangle$ atoms, one $|F=1, m_F=+1\rangle$ atom, and one $|F=1, m_F=-1\rangle$ atom. Spin oscillations are harmonic except near a separatrix in phase space where the oscillation period diverges. The separatrix sets a boundary between the U_2-dominated region and the q_B-dominated region [1,15]. Richer spin dynamics are predicted in lattice-trapped spinor BECs, which allow for many immediate applications. These include constructing a novel quantum-phase-revival spectroscopy driven by a competition between U_2 and spin-independent interaction U_0, understanding quantum magnetism, and realizing massive entanglement [1,3]. However, dynamics of lattice-trapped spinor BECs remain less explored, and most of such experimental studies have been conducted in ferromagnetic ^{87}Rb spinor BECs [21–24].

In this Letter, we experimentally demonstrate that a two-dimensional (2D) optical lattice can conveniently tune spin dynamics of $F=1$ antiferromagnetic spinor BECs. We find that the properties of spinor BECs remain largely unchanged in the presence of a shallow lattice, while sufficiently deep lattices introduce some interesting changes. First, in every lattice depth u_L that supports a substantial superfluid fraction, we observe spin population oscillations after taking spinor BECs out of equilibrium at a fixed q_B. Second, we demonstrate a lattice-tuned separatrix in phase space, and explain it using lattice-enhanced spin-dependent interactions. Another remarkable result is our observation of a phase transition from a longitudinal polar (LP) phase to a broken-axisymmetry (BA) phase in steady states of spinor BECs confined by sufficiently deep lattices [25]. We find the steady states depend exponentially on q_B and sigmoidally on u_L, which agrees with our phenomenological model.

We create a BEC of 7×10^4 sodium atoms fully polarized into the $|F=1, m_F=-1\rangle$ state in a crossed optical trap similar to our previous work [14]. To adiabatically load the BEC into a 2D lattice, we decompress the optical trap to a value which minimizes intraband excitations and ensures approximately constant Thomas-Fermi radii while linearly ramping the lattice potential within $t_{\mathrm{ramp}} > 40$ ms. We construct the 2D lattice in the $\hat{x}$-$\hat{y}$ horizontal plane using two linearly polarized beams which originate from a single-mode laser at $\lambda_L = 1064$ nm, have a waist of ~ 90 μm at the condensate, and are retroreflected to form standing waves. To eliminate cross interference between different beams, the two lattice beams are frequency shifted by 20 MHz with respect to each other. u_L is calibrated using Kapitza-Dirac diffraction patterns. All lattice depths studied in this Letter are kept below $15.0(8)E_R$ to avoid SF-MI phase transitions and thus maintain a sufficient superfluid fraction in our system.

Here $E_R = h^2 k_L^2/(8\pi^2 M)$ is recoil energy, $k_L = 2\pi/\lambda_L$ is the lattice wave number, M is the atomic mass, and h is the Planck constant. We apply a resonant rf pulse of a proper amplitude and duration to lattice-trapped BECs for preparing an initial state with any desired combination of the three m_F states at $q_B/h = 42$ Hz, and then quench q_B to a desired value. After holding atoms for a variable time duration t_{hold}, we abruptly switch off all lattice and trapping potentials. The fractional population of each m_F state, ρ_{m_F}, is measured with Stern-Gerlach absorption imaging after a certain time of flight t_{TOF}. The initial ρ_0 is 0.46, the initial relative phase among the three spin states is zero, and t_{TOF} is 6 ms unless otherwise specified. The total magnetization $m = \rho_{+1} - \rho_{-1}$ appears to be conserved in every time evolution studied in this Letter.

In the presence of a shallow lattice of $u_L < 5E_R$, we observe spin population oscillations similar to those occurring in free space, as shown in Fig. 1. Sharp interference peaks are observed after we release BECs from the shallow lattice [see Fig. 1(a) inset], which indicates coherence and superfluid behavior in the system. As the lattice is made deeper, the separatrix position shifts to a much higher q_B, and the spin oscillations damp out more quickly (especially in the vicinity of each separatrix). These fast damped oscillations make it hard to extract oscillation periods and precisely locate each separatrix even at a moderate u_L (e.g., $4.5E_R$), as shown in Fig. 1(b). A typical anharmonic spin oscillation near a separatrix is shown in the inset in Fig. 1(b). We find our system can be understood by two models: the Bose-Hubbard (BH) model discussed in Ref. [3] for $u_L > 5E_R$, and the single-spatial mode approximation (SMA) defined in Ref. [26] for $u_L < 5E_R$. The BH model has three important terms: U_0, U_2, and the tunneling energy J among adjacent lattice sites. U_2 is proportional to the atomic density in each lattice site, and is positive (negative) in $F = 1$ ^{23}Na (^{87}Rb) BECs. In fact, $U_2/U_0 \simeq 0.04$ for our ^{23}Na system [3], and $U_2 \simeq q_B$ at each separatrix for the initial state studied in Fig. 1 [15]. The observed lattice-tuned separatrix in phase space (i.e., the separatrix position shifts with u_L) is thus mainly due to the fact that U_2 greatly increases with u_L. Figure 1(b) shows a good numerical example: U_2/h is increased from 14 Hz to 32 Hz by changing u_L from $2.5E_R$ to $4.5E_R$.

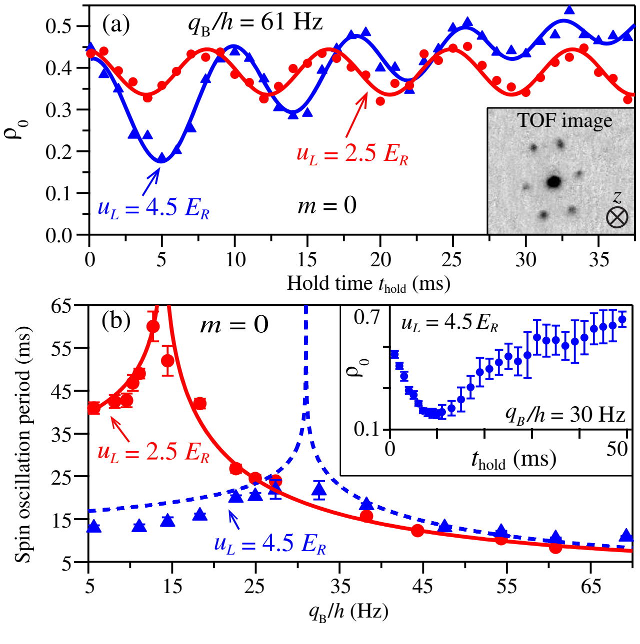

FIG. 1 (color online). (a) Time evolutions of ρ_0 when $u_L = 4.5E_R$ (triangles) and $2.5E_R$ (circles). Solid lines are sinusoidal fits to extract oscillation periods. Inset: a TOF image taken along the vertical direction (z axis) at $t_{\text{TOF}} = 5$ ms. (b) Oscillation period versus q_B. Lines are fits based on SMA. Inset: time evolution of ρ_0 near a separatrix. Uncertainties are extracted from 15–20 repeated Stern-Gerlach measurements. Large uncertainties of ρ_0 near the separatrix may result from shot-to-shot fluctuations, similar to Ref. [11].

Spin oscillations completely damp out and spinor BECs reach their steady states when t_{hold} is long enough [see Fig. 2(a)]. Sufficiently deep lattices are found to bring some interesting changes to the steady states. Figure 2(a) demonstrates one of such changes: once u_L is sufficiently large, the steady states undergo a phase transition from a LP phase (where $\rho_0 = 1$) to a BA phase (where $0 < \rho_0 < 1$) at $m = 0$. We repeat the same measurements with only one parameter changed, i.e., by blocking the retroreflected path of each lattice beam to eliminate standing waves and construct a crossed optical dipole trap (ODT). Its resulting

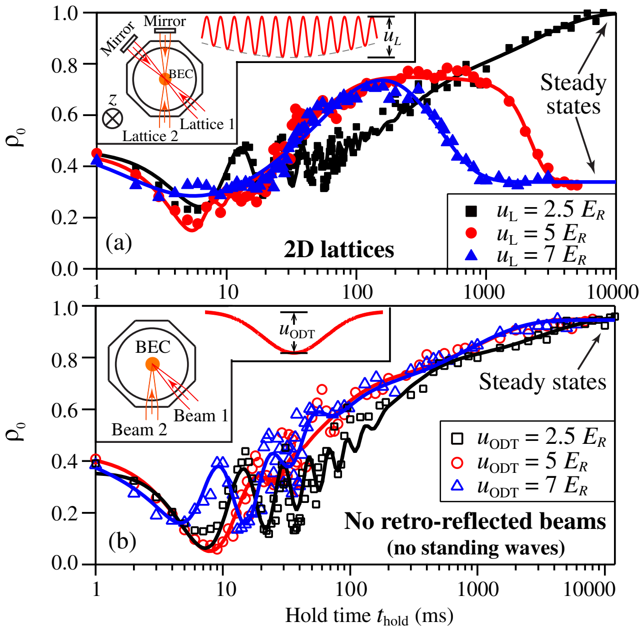

FIG. 2 (color online). (a) Time evolutions of ρ_0 at $q_B/h = 42$ Hz and $m = 0$. Inset: a schematic of our lattice setup and an illustration of the resulting lattice potential. Lines are fits to guide the eye (see Ref. [27]). (b) Similar to panel (a) except that each beam is not retroreflected.

trap depth is u_{ODT}, as illustrated in Fig. 2(b) inset. The power of every beam in Fig. 2(b) is 4 times of that in Fig. 2(a) to ensure $u_L = u_{\mathrm{ODT}}$. Our data in Fig. 2(b) show that spinor BECs at $m = 0$ always reach the LP phase when there are no standing waves. The dramatically different results shown in Figs. 2(a) and 2(b) imply a necessity to understand this LP-BA transition with lattice-modified band structures.

We then study spin oscillations and steady states within a much wider range of u_L and m. Steady states appear to depend sigmoidally on u_L at a fixed q_B, as shown in Fig. 3(a). The inset in Fig. 3(a) demonstrates another surprising result: the observed relationship between ρ_0 and m in steady states at a sufficiently large u_L is well fit by $\rho_0 = (1 - |m|)/3$, which is drastically different from a well-known mean-field prediction (i.e., $\rho_0^{D\approx 0}$ as illustrated by the black dotted line) [25]. This mean-field prediction assumes quantum depletion D is negligible, where D represents the fraction of atoms situated in non-zero momentum states. Based on Bogoliubov theory, the $D \approx 0$ assumption is correct in free space and very shallow lattices for our system [7]. We extract D from TOF images (see Fig. 3 and Ref. [28]) and confirm $D < 5\%$ at $u_L \le 3E_R$. Note that the trapping frequency in each lattice site is much bigger than U_0/h. Our TOF images thus reflect the momentum distribution at the instant of the lattice release and enable us to directly measure D [7].

We also find that D increases with t_{hold} and u_L, and approaches one in steady states when $u_L > 10E_R$, as shown in Fig. 3(d). This lattice-enhanced quantum depletion mainly results from the lattice-flatten dispersion relation and lattice-enhanced interactions, and was originally observed in scalar BEC systems [7]. We develop one phenomenological model to incorporate the observed D and find this model can semiquantitatively describe our data without adjustable parameters, as shown in Figs. 3(a) and 4(a). In this model, the steady states are determined by a comparison between $T(\mathbf{k}, m_F = 0)$ and $T(0, m_F = \pm 1)$, where $T(\mathbf{k}, m_F)$ is the dispersion relation of the m_F state and $\mathbf{k}$ is the atom's quasimomentum. Figure 4(b) illustrates two example comparisons. Note that only the first Brillouin zone is considered, since the population in higher bands is negligible. Based on Refs. [5–7], we calculate $T(\mathbf{k}, m_F)$ as follows:

$$T(\mathbf{k}, m_F) = 4J \sum_{\alpha=x,y} \sin^2\left(\frac{\pi k_\alpha}{2k_L}\right) + E_R \frac{k_z^2}{k_L^2} + q_B m_F^2, \quad (1)$$

where a uniform density function is applied along the vertical direction without a lattice (the z axis), and J is calculated using a Wannier density function along each of the two horizontal directions with lattices. The linear Zeeman effect is ignored because it remains unchanged in coherent interconversions.

We divide $T(\mathbf{k}, m_F = 0)$ into two regions based on $T(0, m_F = \pm 1)$, i.e., set the boundary of the two regions at $\mathbf{k}_c$ which satisfies $T(\mathbf{k}_c, m_F = 0) = T(0, m_F = \pm 1)$, as marked by vertical dotted lines in Fig. 4(b). The dispersion relations are significantly flattened as u_L increases, since the predicted width of the first band is $\sim 4J$ and J exponentially reduces with u_L [6,7]. To clearly explain our model using the dispersion relations shown in Fig. 4(b), we only consider $m = 0$ and $k_y = k_z = 0$ in this paragraph. In region 1 where $0 \le |k_x| < |\mathbf{k}_c|$, atoms in the $m_F = 0$ state always have energy smaller than those in the $m_F = \pm 1$ states. The steady states should thus be the $m_F = 0$ state (i.e., $\rho_0 = 1$), which equals $\rho_0^{D\approx 0}$. When D is big enough, atoms start to occupy region 2 where $|\mathbf{k}_c| \le |k_x| \le k_L$. The $m_F = 0$ atoms in region 2 are degenerate with $m_F = \pm 1$ atoms at certain other momenta. This degeneracy may account for the phenomenological relationship shown in Fig. 3(a), i.e., $\rho_0 = 1/3$ in steady states at a big u_L. Our data and the dispersion relations thus suggest that atoms in steady states may be equally distributed among the three m_F states at a big enough D.

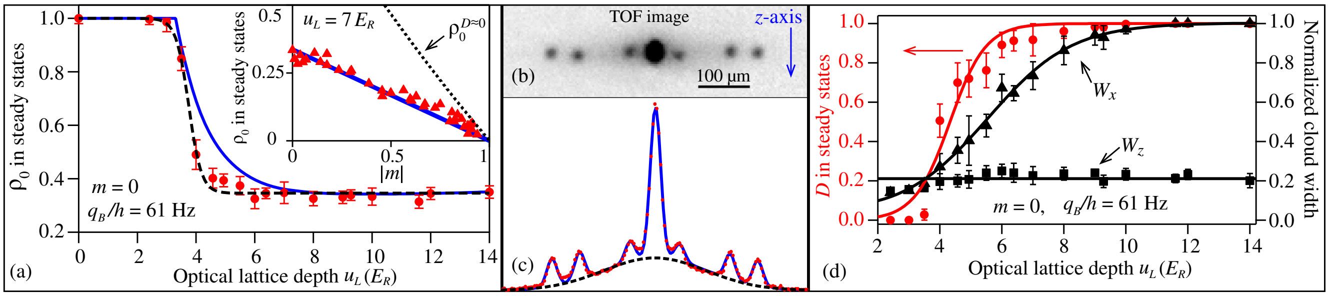

FIG. 3 (color online). (a) ρ_0 in steady states as a function of u_L (main figure) and $|m|$ (inset figure). Solid lines are predictions derived from Eq. (2). The dashed and dotted lines, respectively, represent a sigmoidal fit and $\rho_0^{D\approx 0}$ (see Ref. [25]). (b) A typical TOF image. Using method 1, the extracted D is 53% from this image (see Ref. [28]). (c) Density profile (red dotted line) of the image shown in panel (b) through all interference peaks. Using method 2 (blue solid line), the extracted D is 52.5% (see Ref. [28]). The black dashed line highlights the quantum depleted fraction. (d) W_x (triangles), W_z (squares), and D (circles) in steady states as a function of u_L. The widths are normalized by k_L. Lines are respectively sigmoid fits to W_x and D, and a linear fit to W_z.

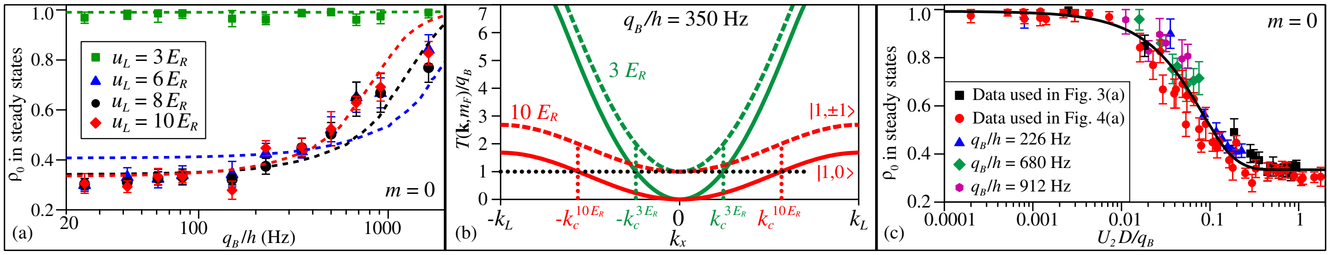

FIG. 4 (color online). (a) ρ_0 in steady states as a function of q_B. Dashed lines are predictions derived from Eq. (2). Green, blue, black, and red colors, respectively, represent results at $u_L = 3$, 6, 8, and $10E_R$. (b) Dispersion relations normalized by q_B as a function of k_x when $k_y = k_z = 0$. Solid (dashed) lines represent results of the $m_F = 0$ ($m_F = \pm 1$) states. The black horizontal dotted line marks $T(\mathbf{k}, m_F) = q_B$, and vertical dotted lines mark boundaries between region 1 and region 2 at $u_L = 3$ and $10E_R$. (c) ρ_0 in steady states versus U_2D/q_B. Black, red, blue, green, and purple colors, respectively, represent data used in Figs. 3(a) and 4(a), and additional data taken at $q_B/h = 226$, 680, and 912 Hz. The solid line is a sigmoid fit.

We can apply similar discussions and our model to all nonzero m. Thus ρ_0 in the steady states is expressed as

$$\rho_0 \approx \int_{\text{region 1}} n(\mathbf{k})\rho_0^{D\approx 0}\, d\mathbf{k} + \int_{\text{region 2}} n(\mathbf{k})\frac{1-|m|}{3}\, d\mathbf{k}. \qquad (2)$$

The normalized atomic density in steady states, $n(\mathbf{k})$, is calculated by the following phenomenological formula: $n(\mathbf{k}) = (1-D)\delta_{\mathbf{k}} + D\exp[-(k_x^2/W_x^2 + k_y^2/W_y^2 + k_z^2/W_z^2)/2]/A$, where W_x and W_z are the half widths of a 2D Gaussian fit to a TOF distribution within the first Brillouin zone, $W_y = W_x$, A is a normalization factor, and δ is a Dirac-delta function [29]. Figure 3(d) shows that W_x and D sigmoidally increase with u_L, and saturate at their peak values when $u_L > 10E_R$; i.e., atoms occupy all available states and quantum depletion saturates the first Brillouin zone in a deep lattice. In contrast, W_z appears to be independent of u_L, which implies a constant system temperature.

The observed sigmoidal dependence of steady states on u_L and the exponential dependence on q_B can be explained by our model [Eq. (2)], as respectively shown in Figs. 3(a) and 4(a). Quantitative agreements between our model and data are found everywhere except in high magnetic fields where $q_B/h > 1000$ Hz, and in a lattice where $4E_R \leq u_L \leq 6E_R$. Limited imaging resolutions and heating induced by an extra magnetic coil in creating high q_B may both contribute to the discrepancy.

To better understand the LP-BA phase transition, we plot ρ_0 versus U_2D/q_B (a dimensionless ratio) at $m = 0$ in Fig. 4(c). Here U_2/q_B is the key factor determining the spinor dynamics in free space, D represents the lattice-induced effect, and both D and U_2 increase with the spin-independent interaction U_0. Two interesting results are found in Fig. 4(c): all 80 data points taken at very different u_L and q_B are fit by one sigmoid function; and the critical point of the LP-BA transition appears to be $U_2D/q_B \sim 0.01$. (In contrast, each predicted separatrix locates around $U_2/q_B = 1$ based on SMA and parameters studied in Fig. 4.) The LP-BA transition may thus result from a competition between q_B and the "effective" interaction U_2D; i.e., regions with strong enough interactions may prefer the BA phase. In principle, we can verify this using other methods which can efficiently tune interatomic interactions, e.g., via Feshbach resonances.

In conclusion, we have conducted the first experimental study on dynamics and the phase diagram of lattice-trapped antiferromagnetic spinor BECs. A lattice-tuned separatrix in phase space and the LP-BA phase transition in steady states have been observed. We have found that ρ_0, D, and thus the main findings of this Letter are nearly independent of t_{TOF}. We have also developed a phenomenological model that describes our data without adjustable parameters.

We thank the Army Research Office and the National Science Foundation for financial support.

---

[*] yingmei.liu@okstate.edu

[1] D. M. Stamper-Kurn and M. Ueda, Rev. Mod. Phys. **85**, 1191 (2013).
[2] Y. Kawaguchi and M. Ueda, Phys. Rep. **520**, 253 (2012).
[3] K. W. Mahmud and E. Tiesinga, Phys. Rev. A **88**, 023602 (2013).
[4] M. Greiner, O. Mandel, T. Esslinger, T. W. Hasch, and I. Bloch, Nature (London) **415**, 39 (2002).
[5] D. Jaksch, C. Bruder, J. I. Cirac, C. W. Gardiner, and P. Zoller, Phys. Rev. Lett. **81**, 3108 (1998).
[6] M. P. A. Fisher, P. B. Weichman, G. Grinstein, and D. S. Fisher, Phys. Rev. B **40**, 546 (1989).
[7] K. Xu, Y. Liu, D. E. Miller, J. K. Chin, W. Setiawan, and W. Ketterle, Phys. Rev. Lett. **96**, 180405 (2006).
[8] G. G. Batrouni, V. G. Rousseau, and R. T. Scalettar, Phys. Rev. Lett. **102**, 140402 (2009).
[9] A. T. Black, E. Gomez, L. D. Turner, S. Jung, and P. D. Lett, Phys. Rev. Lett. **99**, 070403 (2007).
[10] Y. Liu, S. Jung, S. E. Maxwell, L. D. Turner, E. Tiesinga, and P. D. Lett, Phys. Rev. Lett. **102**, 125301 (2009).
[11] Y. Liu, E. Gomez, S. E. Maxwell, L. D. Turner, E. Tiesinga, and P. D. Lett, Phys. Rev. Lett. **102**, 225301 (2009).

[12] E. M. Bookjans, A. Vinit, and C. Raman, Phys. Rev. Lett. **107**, 195306 (2011).

[13] D. Jacob, L. Shao, V. Corre, T. Zibold, L. De Sarlo, E. Mimoun, J. Dalibard, and F. Gerbier, Phys. Rev. A **86**, 061601(R) (2012).

[14] J. Jiang, L. Zhao, M. Webb, N. Jiang, H. Yang, and Y. Liu, Phys. Rev. A **88**, 033620 (2013).

[15] L. Zhao, J. Jiang, T. Tang, M. Webb, and Y. Liu, Phys. Rev. A **89**, 023608 (2014).

[16] J. Jiang, L. Zhao, M. Webb, and Y. Liu, Phys. Rev. A **90**, 023610 (2014).

[17] M.-S. Chang, Q. Qin, W. Zhang, L. You, and M. S. Chapman, Nat. Phys. **1**, 111 (2005).

[18] T. Kuwamoto, K. Araki, T. Eno, and T. Hirano, Phys. Rev. A **69**, 063604 (2004).

[19] J. Kronjäger, C. Becker, P. Navez, K. Bongs, and K. Sengstock, Phys. Rev. Lett. **97**, 110404 (2006).

[20] H. Schmaljohann, M. Erhard, J. Kronjäger, M. Kottke, S. van Staa, L. Cacciapuoti, J. J. Arlt, K. Bongs, and K. Sengstock, Phys. Rev. Lett. **92**, 040402 (2004).

[21] C. Becker, P. Soltan-Panahi, J. Kronjäger, S. Dörscher, K. Bongs, and K. Sengstock, New J. Phys. **12**, 065025 (2010).

[22] A. Widera, F. Gerbier, S. Fölling, T. Gericke, O. Mandel, and I. Bloch, Phys. Rev. Lett. **95**, 190405 (2005).

[23] P. L. Pedersen, M. Gajdacz, F. Deuretzbacher, L. Santos, C. Klempt, J. F. Sherson, A. J. Hilliard, and J. J. Arlt, Phys. Rev. A **89**, 051603(R) (2014).

[24] A. Widera, F. Gerbier, S. Fölling, T. Gericke, O. Mandel, and I. Bloch, New J. Phys. **8**, 152 (2006).

[25] Based on the mean-field theory [16], the ground states of antiferromagnetic $F = 1$ spinor BECs at a positive q_B are in one of the following three phases: (a) an antiferromagnetic phase where $\rho_0^{D\approx 0} = 0$, when $q_B < U_2(1 - \sqrt{1 - m^2})$; (b) a LP phase where $\rho_0^{D\approx 0} = 1$, when $m = 0$; (c) a BA phase where $\rho_0^{D\approx 0}$ is the root of the following equation: $1 - 2\rho_0^{D\approx 0} - [(1 - 2\rho_0^{D\approx 0})(1 - \rho_0^{D\approx 0}) - m^2]/[\sqrt{(1 - \rho_0^{D\approx 0})^2 - m^2}] = q_B/U_2$.

[26] W. Zhang, D. L. Zhou, M.-S. Chang, M. S. Chapman, and L. You, Phys. Rev. A **72**, 013602 (2005).

[27] The fitting functions used in Figs. 2(a) and 2(b) are respectively $\rho_0(t) = A_0 - A_1 e^{-t/\tau_0} - A_2/(1 + A_3 e^{-t/\tau_1}) + A_4 e^{-t/\tau_2} \sin(\omega e^{t/\tau_3} t + \phi)$ and $\rho_0(t) = A_0 - A_1 e^{-t/\tau_0} - A_2 e^{-t/\tau_1} + A_4 e^{-t/\tau_2} \sin(\omega e^{t/\tau_3} t + \phi)$, where A_0, A_1, A_2, A_3, A_4, τ_0, τ_1, τ_2, τ_3, ω and ϕ are fitting parameters.

[28] We extract N_D (the number of atoms in all nonzero momentum states) from TOF images with two fitting methods which render similar results. Method 1 is suggested by Ref. [7]: we mask off all the interference peaks, and conduct a 2D Gaussian fit to the background for extracting N_D. In method 2, we plot a density profile of a TOF image through all interference peaks, and then fit the density profile with a combination of eight Gaussian functions, i.e., one function to each interference peak, and the eighth one to the broad background for extracting N_D.

[29] The normalization factor A is an integration, $\int \exp[-(k_x^2/W_x^2 + k_y^2/W_y^2 + k_z^2/W_z^2)/2] d\mathbf{k}$, over the first Brillouin zone.

APPENDIX D

MAPPING THE PHASE DIAGRAM OF SPINOR CONDENSATES VIA ADIABATIC QUANTUM PHASE TRANSITIONS

This appendix includes a reprint of Ref. (Jiang *et al.*, 2014): J. Jiang, L. Zhao, M. Webb, and Y. Liu, Mapping the phase diagram of spinor condensates via adiabatic quantum phase transitions, Phys. Rev. A **90**, 023610 (2014).

PHYSICAL REVIEW A **90**, 023610 (2014)

Mapping the phase diagram of spinor condensates via adiabatic quantum phase transitions

J. Jiang, L. Zhao, M. Webb, and Y. Liu*

Department of Physics, Oklahoma State University, Stillwater, Oklahoma 74078, USA

(Received 28 April 2014; published 7 August 2014)

We experimentally study two quantum phase transitions in a sodium spinor condensate immersed in a microwave dressing field. We also demonstrate that many previously unexplored regions in the phase diagram of spinor condensates can be investigated by adiabatically tuning the microwave field across one of the two quantum phase transitions. This method overcomes two major experimental challenges associated with some widely used methods, and is applicable to other atomic species. Agreements between our data and the mean-field theory for spinor Bose gases are also discussed.

DOI: 10.1103/PhysRevA.90.023610 PACS number(s): 67.85.Fg, 03.75.Kk, 03.75.Mn, 05.30.Rt

I. INTRODUCTION

A spinor Bose-Einstein condensate (BEC) is a multicomponent BEC with an additional spin degree of freedom, which has provided exciting opportunities to study quantum magnetism, superfluidity, strong correlations, spin squeezing, and massive entanglement [1–5]. The interesting interactions in spinor BECs are interconversions among multiple spin states and magnetic-field interactions (or microwave dressing field interactions) characterized by $q_{\rm net}$, the net quadratic Zeeman energy. The interplay of these interactions leads to oscillations among multiple spin populations, which has been experimentally confirmed in $F = 1$ ^{23}Na spinor BECs [6–12], and in both $F = 1$ and $F = 2$ ^{87}Rb spinor condensates [13–17].

Several groups demonstrated the mean-field (MF) ground states of spinor BECs by holding BECs in a fixed magnetic field and letting spin population oscillations damp out over a few seconds [8–11]. The required damping time, determined by energy dissipation, may in some cases exceed the BEC lifetime. The exact mechanism involved in energy dissipation requires further study, although it has been shown that energy dissipates much faster in high magnetic fields [10]. For $F = 1$ BECs, a magnetic field introduces only a positive $q_{\rm net}$, while a microwave field has a distinct advantage since it can induce both positive and negative $q_{\rm net}$ [1,7,12,18,19]. As shown in Ref. [12], the same physics model explains spin-mixing dynamics observed in both microwave fields and magnetic fields. One would assume that, if given a long enough exposure to a microwave field, a spinor BEC could also reach its MF ground states. However, experimental studies on ground states of spinor BECs in microwave fields have proven to be very difficult, since these fields are created by near-resonant microwave pulses. Two major experimental challenges associated with microwave fields are atom losses and variations in magnetization m. A different inelastic collision rate in each hyperfine state may be one of the possible reasons to account for these challenges. Microwave-induced changes in both m and the atom number N can be detrimental, especially when a spinor BEC is exposed to a large microwave field for a prolonged time [7,12]. As a result, the phase diagram of $F = 1$ BECs has not been well explored in the $q_{\rm net} \leqslant 0$ region, where applying microwave fields may be necessary.

In this paper, we demonstrate another method to overcome the aforementioned experimental challenges and report the observation of two quantum phase transitions in a spinor BEC. In this method, we quickly prepare an initial equilibrium state at a very high magnetic field to minimize the damping time for spin population oscillations and prevent unnecessary exposure to microwave pulses. Equilibrium states at a desired $q_{\rm net}$ are then created by adiabatically sweeping an additional microwave field. Using this method, we are able to investigate many previously unexplored regions in the phase diagram of antiferromagnetic spinor BECs and observe three distinct quantum phases. Similarly to Refs. [1,2,11], we define three phases in the MF ground states based on ρ_0, the fractional population of the $|F = 1, m_F = 0\rangle$ state: $\rho_0 = 1$, $\rho_0 = 0$, and $0 < \rho_0 < 1$ respectively represent a longitudinal polar phase, an antiferromagnetic (AFM) phase, and a broken-axisymmetry (BA) phase. We observe two quantum phase transitions: one is between a longitudinal polar phase and a BA phase at a fixed positive $q_{\rm net}$, and the other is an AFM-BA phase transition at a given m. We also calculate the energy gap between the ground states and the first excited states in a spinor BEC, which provides an explanation for the feasibility of this method. In addition, spin domains and spatial modes are not observed in our system, and our data can be well fit by predictions of the single spatial-mode approximation (SMA).

The SMA assumes all spin states share the same spatial wave function, which has been a successful model to understand spinor microcondensates [8–13,20–22]. The fractional population ρ_{m_F} and the phase θ_{m_F} of each m_F state are thus independent of position in SMA, and $m = \rho_{+1} - \rho_{-1}$. The spin-dependent interaction energy c is proportional to the atom density, and is positive (or negative) in $F = 1$ antiferromagnetic ^{23}Na (or ferromagnetic ^{87}Rb) spinor BECs. For example, c/h is 40 Hz for our ^{23}Na system in this paper, where h is the Planck constant. After taking into account that N and m are independent of time t and neglecting all constant terms in the Hamiltonian of spinor BECs, we use the SMA to express the BEC energy E and the time evolution of ρ_0 and θ as [1,20,21]

$$E(t) = c\rho_0(t)\{[1 - \rho_0(t)] + \sqrt{[1 - \rho_0(t)]^2 - m^2}\cos[\theta(t)]\} + q_{\rm net}(t)[1 - \rho_0(t)], \tag{1}$$

---

*yingmei.liu@okstate.edu

$$\dot{\rho}_0 = -\frac{4\pi}{h}\frac{\partial E(t)}{\partial \theta(t)}, \quad \dot{\theta} = \frac{4\pi}{h}\frac{\partial E(t)}{\partial \rho_0(t)}. \tag{2}$$

Here $q_{\rm net} = q_M + q_B$ is the net quadratic Zeeman energy with q_B (or q_M) being induced by magnetic (or microwave dressing) fields. The relative phase among the three m_F spin states is $\theta = \theta_{+1} + \theta_{-1} - 2\theta_0$.

By minimizing Eq. (1), we find ρ_0 in a MF ground state of $F = 1$ spinor BECs is zero if $q_{\rm net} < c(1 \pm \sqrt{1-m^2})$, or equal to one if $m = 0$ and $q_{\rm net} > -c(1 \pm 1)$, or is the root of the following equation at all other $q_{\rm net}$ and m:

$$c\left[1 - 2\rho_0 \pm \frac{(1-2\rho_0)(1-\rho_0) - m^2}{\sqrt{(1-\rho_0)^2 - m^2}}\right] - q_{\rm net} = 0, \tag{3}$$

where the + (or −) sign applies to ferromagnetic (or antiferromagnetic) spinor BECs. Typical MF ground states of spin-1 sodium BECs are shown in Figs. 1 and 2. Our experimental phase diagram and the theoretical phase diagram based on Eqs. (1)–(3) are also plotted in Fig. 3.

II. EXPERIMENTAL SETUP

The experimental setup is similar to that elaborated in our recent publications [6,12]. A $F = 1$ BEC of 5×10^4 atoms is created by a forced evaporation in a crossed optical dipole trap. To fully polarize atoms into the $|F = 1, m_F = -1\rangle$ state, we turn on a weak magnetic-field gradient and a low magnetic bias field in the forced evaporative cooling process. A resonant rf pulse of a proper amplitude and duration is applied to prepare an initial state with any desired combination of the three m_F states. This moment is defined as the starting point ($t = 0$) of our experimental sequences, as shown in Fig. 1(a). Every sequence ends at $t = t_f$. Populations of multiple spin states are then measured by a standard Stern-Gerlach absorption imaging.

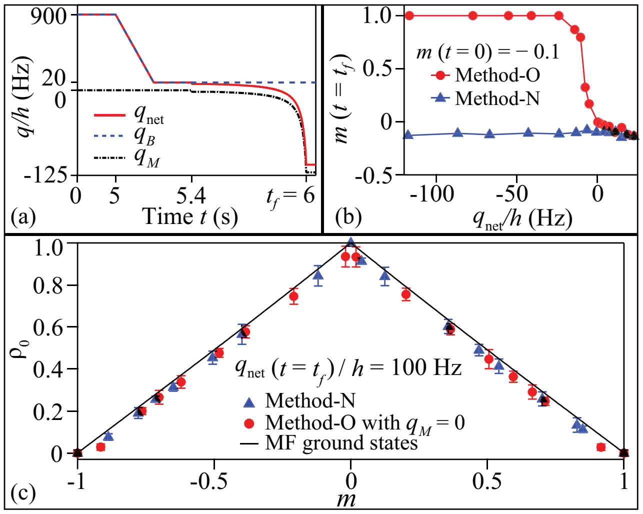

FIG. 1. (Color online) (a) Typical experimental sequence of Method-N, which is our method to create equilibrium states via adiabatically sweeping a microwave field. In this paper -150 Hz $\leqslant q_{\rm net}(t = t_f)/h \leqslant 150$ Hz. All axes are not to scale. (b) m as a function of $q_{\rm net}$ at $t = t_f$ in the two methods starting from the same initial state, i.e., $m(t = 0) = -0.1$. Note that t_f for Method-O in this panel is only 1 s, which is much shorter than the typical hold time for creating equilibrium states. (c) ρ_0 as a function of m at $q_{\rm net}(t = t_f)/h = 100$ Hz in equilibrium states created by the two methods. In this panel, Method-O prepares equilibrium states by holding BECs for 8 s in a high magnetic field, where $q_M = 0$ and $q_B/h = 100$ Hz. The solid black line represents the MF ground states (see text).

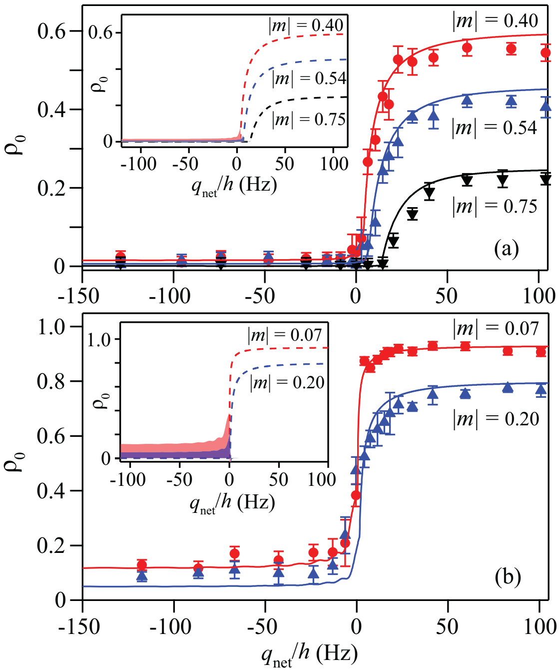

FIG. 2. (Color online) ρ_0 as a function of $q_{\rm net}$ at $t = t_f$ for three large $|m|$ in panel (a) and for two small $|m|$ in panel (b) in equilibrium states created by our Method-N. Solid lines are simulation results for the experimental processes based on Eq. (2) (see text). Insets: dashed lines are the MF ground states. Shaded areas represent the differences between our simulation results and the MF theory at various m. The black, blue, and red colors in panel (a) respectively correspond to results at $|m| = 0.75$, 0.54, and 0.40. The blue and red colors in panel (b) represent results at $|m| = 0.20$ and 0.07, respectively.

We use two different methods to generate equilibrium states. The Method-O is an old and widely used method, which creates equilibrium states simply by holding a BEC at a fixed $q_{\rm net}$ for a sufficiently long time. We find that the required hold time is longer than 2 s for all positive $q_{\rm net}$ studied in this paper. This old method fails for our system in low magnetic fields (i.e, the small positive $q_{\rm net}$ region), because energy dissipates very slowly and the required hold time is longer than the BEC lifetime (∼10 s) in this region. This old method is more problematic in the negative $q_{\rm net}$ region, because it leads to significant atom losses and detrimental changes in m. In order to overcome these experimental challenges associated with the old method, we have developed another method, Method-N. A comparison of these two methods starting from the same initial state is shown in Fig. 1(b), which highlights the advantage of our method. Note that m and N may not be conserved using the old method, when a microwave field induced by a near-resonant microwave pulse is applied. This is due to the fact that the microwave pulse unavoidably excites some atoms

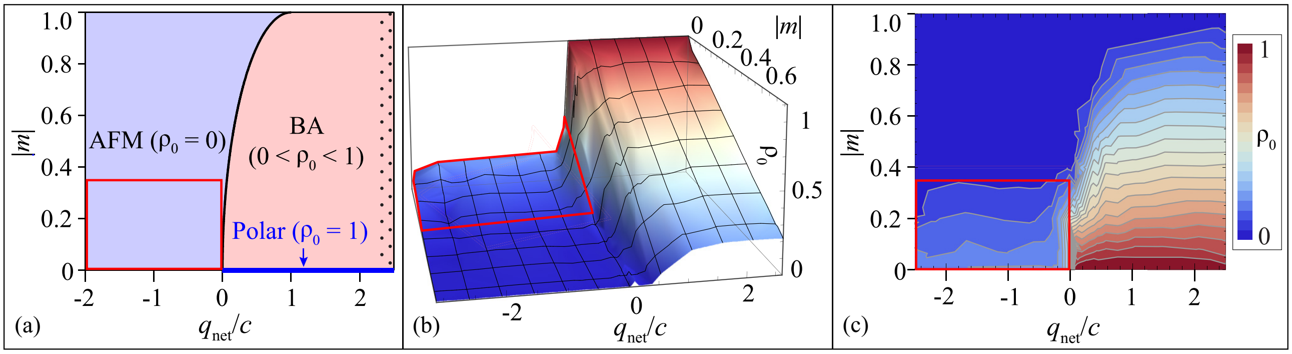

FIG. 3. (Color online) (a) MF phase diagram of spin-1 antiferromagnetic spinor BECs based on Eqs. (1)–(3). Our Method-N works everywhere except in the area marked by red solid lines, while Method-O only applies to the area filled with dots at large $q_{\rm net}$. Panel (b) [or (c)] is a 3D (or a contour) plot of the experimental phase diagram consisting of data taken by Method-N at 153 different $q_{\rm net}$ and m. Red solid lines in panels (b) and (c) mark the region where our data are different from the MF ground states.

in a $F = 1$ spinor BEC to the $F = 2$ manifold, and more atoms are excited when the microwave pulse has a higher power or a smaller frequency detuning with respect to the $|F = 1\rangle \leftrightarrow |F = 2\rangle$ transitions.

A typical experimental sequence of our Method-N is listed in Fig. 1(a). We first hold a spinor BEC in the optical trap for 5 s at a very high magnetic field with $q_B/h = 900$ Hz. This step ensures the BEC reaches its ground states, since we and Ref. [10] find that the energy dissipation rate quickly increases with q_B. Second, we adiabatically ramp the magnetic field down to $q_B/h = 20$ Hz in 0.1 s, keep q_B at this value for 0.3 s, and then turn on a far off-resonant microwave pulse in 0.1 s. Third, we tune only the frequency of this pulse slowly within 0.5 s, in order to adiabatically sweep its corresponding microwave field to a desired $q_{\rm net}$. Our approach to characterize microwave dressing fields and the frequency tuning curve for adiabatically sweeping $q_{\rm net}$ within the range of $-\infty$ to $+\infty$ is the same as those illustrated in our previous work [12].

In theory, once a BEC is prepared into its ground state, the BEC may stay in its ground state at each $q_{\rm net}$ when a microwave field is adiabatically ramped [3]. We can thus initially check whether our Method-N is applicable by comparing equilibrium states created by both our method and the old method in a region, $q_{\rm net} \gg 0$, where the old method has been proven to generate the MF ground states [8–11]. Figure 1(c) shows such comparisons made at $q_{\rm net}(t = t_f)/h = 100$ Hz for various magnetization m. The equilibrium states created by the two methods appear to be quite similar, and they stay very close to the same black solid line which represents the MF ground states in Fig. 1(c). This suggests that our method is adiabatic enough to replace the old method in studies related to the BEC phase diagrams. We also find that a spinor BEC returns to its original state when we ramp a microwave field from $q_M = 0$ to a fixed nonzero q_M and then back to $q_M = 0$ with Method-N, although this observation may not be sufficient to prove the process is adiabatic.

III. MAPPING THE PHASE DIAGRAM OF SPINOR CONDENSATES

We then apply our method to a much wider range of $q_{\rm net}$ and m, especially in the negative and small positive $q_{\rm net}$ regions which cannot be easily explored by the old method, as shown in Fig. 2. We find two interesting results from this figure. First, our data in Fig. 2(a) show a quantum phase transition between a BA phase and an AFM phase at each m. This BA-AFM phase transition appears to occur at a larger $q_{\rm net}$ when $|m|$ gets bigger, which can be well explained by the MF theory [i.e., dashed lines in the inset in Fig. 2(a)]. Another interesting result is that Method-N does allow us to access many previously unexplored regions in the phase diagram, although there is a visible discrepancy between the MF ground states and our data at a small m in the negative $q_{\rm net}$ region, as shown in Fig. 2(b). To understand this phenomenon, we simulate the experimental processes based on Eq. (2) by taking a proper formula to account for the time evolution of $q_{\rm net}$ during an adiabatic ramping of microwave fields. Figure 2 shows that the simulation results can well resemble the experimental data, while the differences between our simulation results and the MF ground states are emphasized by a shaded area at each m in the two insets in Fig. 2. These shaded areas appear to slowly increase in the negative $q_{\rm net}$ region when $|m|$ approaches zero. In other words, the discrepancy between our data and the MF ground states only becomes noticeable at a small $|m|$ in the negative $q_{\rm net}$ region. Due to this discrepancy, we find that the predicted quantum phase transition between an AFM phase and a longitudinal polar phase at $m = 0$ and $q_{\rm net} = 0$ is replaced by a transition between a BA phase and a longitudinal polar phase. Since our experimental resolution for ρ_0 is around 0.02, Fig. 2 implies that our method is sufficient to map out the BEC phase diagram in the positive $q_{\rm net}$ region at each m, and in the negative $q_{\rm net}$ as long as $|m| \geqslant 0.4$.

Figure 3 clearly summarizes the improvement provided by Method-N, after comparing the theoretical MF phase diagram to an experimental phase diagram consisting of our data taken at 153 different $q_{\rm net}$ and m. All three predicted phases (i.e., an AFM, a polar, and a BA phase), an AFM-BA phase transition at a fixed m, and a transition between a longitudinal polar phase and a BA phase at a certain positive $q_{\rm net}$ are shown in the experimental phase diagram. Good agreement between our data and the MF ground states can be found everywhere in the two phase diagrams except in the region where $|m| < 0.4$ and $q_{\rm net} < 0$. This problematic region has been marked by red solid lines in Fig. 3. Ramping microwave fields at a slower rate should help to diminish this problematic region; however, a slower rate requires holding a BEC in microwave

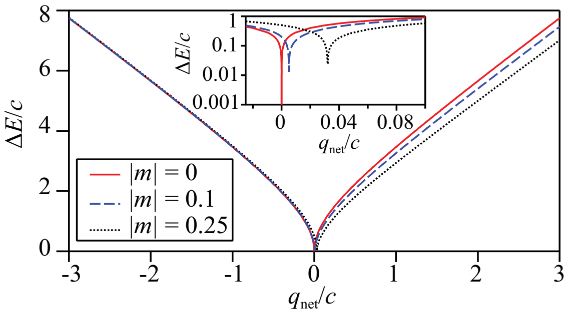

FIG. 4. (Color online) Energy gap ΔE in the unit of c as a function of $q_{\rm net}/c$ at three $|m|$ based on Eq. (4) (see text). Inset: a magnified view of the main figure in the region of $-0.025 < q_{\rm net}/c < 0.1$.

fields for a longer time and thus inevitably leads to more atom losses and a bigger change in m. In fact, we tried quite a few different microwave ramping rates, but none of them enabled a spinor BEC to reach its MF ground states when m is very small and $q_{\rm net} < 0$. The same problem also exists in simulation results: our simulation program cannot suggest a reasonable ramping rate to ensure an adiabatic sweep of $q_{\rm net}$ across a phase transition for a small m.

To understand this problem, we need to find the exact value of ΔE, the energy gap between the ground state and the first excited state in spinor BECs. Similar to Ref. [3], we can describe a spinor BEC in the Fock space. The spin-dependent part of the Hamiltonian in a $F = 1$ spinor BEC can be expressed as [3,20,23]

$$H = \sum_{i,j,k,l=-1}^{1} \left[q_{\rm net} k^2 a_k^\dagger a_k + \frac{c}{2} \sum_\gamma a_k^\dagger a_i^\dagger (F_\gamma)_{ij} (F_\gamma)_{kl} a_j a_l \right], \tag{4}$$

since m is conserved and there are only a finite number of atoms in a typical equilibrium state studied in this paper. Here a_k ($a_k^\dagger$) is the annihilation (creation) operator of the $|F = 1, m_F = k\rangle$ state, and $F_{\gamma=x,y,z}$ are the spin-1 matrices. By diagonalizing the Hamiltonian in Eq. (4) and performing an exact numerical many-body calculation, we can find the energy gaps. Figure 4 shows numerical examples of ΔE at three typical $|m|$. It appears that ΔE drastically drops by more than three orders of magnitude when $|m|$ and $q_{\rm net}$ approach zero, as shown in the inset in Fig. 4. Therefore, it is not surprising that adiabatically sweeping $q_{\rm net}$ across a quantum phase transition point is not feasible at a very small m, especially at $m = 0$. We can also calculate ΔE_e, the energy gap between the highest eigenstate and the second highest eigenstate of Eq. (4). The minimal value of ΔE_e at $m = 0$ appears to be larger than that of ΔE (the energy gap associated with the ground state) at $m = 0.75$. In other words, adiabatically sweeping $q_{\rm net}$ across a quantum phase transition demonstrated in this paper may be useful for confirming other important predictions, for instance, realizing massive entanglement in the highest eigenstate of antiferromagnetic spinor BECs [3].

IV. CONCLUSION

In conclusion, we have observed two types of quantum phase transitions in a spin-1 antiferromagnetic spinor BEC, and developed another method to create the equilibrium states of spinor condensates by adiabatically sweeping a microwave field. The biggest advantage of this method is to avoid significant atom losses and detrimental changes in m at large microwave fields. We have demonstrated that this method enables us to conduct an experimental study on the phase diagram of antiferromagnetic spinor BECs at various m in the negative $q_{\rm net}$ region. Our experimental phase diagram agrees with the MF theory for all m in the positive $q_{\rm net}$ region and for all negative $q_{\rm net}$ as long as $|m| \geqslant 0.4$. This method can be applied to other atomic species and may be helpful to discover interesting quantum phase transitions in other systems, for example, revealing a BA-AFM quantum phase transition in $F = 1$ ^{87}Rb spinor BECs at a negative $q_{\rm net}$.

ACKNOWLEDGMENTS

We thank the Army Research Office, the National Science Foundation, and the Oklahoma Center for the Advancement of Science and Technology for financial support. M.W. thanks the Niblack Research Scholar program.

---

[1] D. M. Stamper-Kurn and M. Ueda, Rev. Mod. Phys. **85**, 1191 (2013).
[2] Y. Kawaguchi and M. Ueda, Phys. Rep. **520**, 253 (2012).
[3] Z. Zhang and L.-M. Duan, Phys. Rev. Lett. **111**, 180401 (2013).
[4] T. M. Hoang, C. S. Gerving, B. J. Land, M. Anquez, C. D. Hamley, and M. S. Chapman, Phys. Rev. Lett. **111**, 090403 (2013).
[5] C. D. Hamley, C. S. Gerving, T. M. Hoang, E. M. Bookjans, and M. S. Chapman, Nat. Phys. **8**, 305 (2012).
[6] J. Jiang, L. Zhao, M. Webb, N. Jiang, H. Yang, and Y. Liu, Phys. Rev. A **88**, 033620 (2013).
[7] E. M. Bookjans, A. Vinit, and C. Raman, Phys. Rev. Lett. **107**, 195306 (2011).
[8] A. T. Black, E. Gomez, L. D. Turner, S. Jung, and P. D. Lett, Phys. Rev. Lett. **99**, 070403 (2007).
[9] Y. Liu, S. Jung, S. E. Maxwell, L. D. Turner, E. Tiesinga, and P. D. Lett, Phys. Rev. Lett. **102**, 125301 (2009).
[10] Y. Liu, E. Gomez, S. E. Maxwell, L. D. Turner, E. Tiesinga, and P. D. Lett, Phys. Rev. Lett. **102**, 225301 (2009).
[11] D. Jacob, L. Shao, V. Corre, T. Zibold, L. De Sarlo, E. Mimoun, J. Dalibard, and F. Gerbier, Phys. Rev. A **86**, 061601 (2012).
[12] L. Zhao, J. Jiang, T. Tang, M. Webb, and Y. Liu, Phys. Rev. A **89**, 023608 (2014).
[13] M.-S. Chang, Q. Qin, W. Zhang, L. You, and M. S. Chapman, Nat. Phys. **1**, 111 (2005).
[14] A. Widera, F. Gerbier, S. Fölling, T. Gericke, O. Mandel, and I. Bloch, New J. Phys. **8**, 152 (2006).
[15] J. Kronjäger, C. Becker, P. Navez, K. Bongs, and K. Sengstock, Phys. Rev. Lett. **97**, 110404 (2006).

[16] H. Schmaljohann, M. Erhard, J. Kronjäger, M. Kottke, S. van Staa, L. Cacciapuoti, J. J. Arlt, K. Bongs, and K. Sengstock, Phys. Rev. Lett. **92**, 040402 (2004).

[17] T. Kuwamoto, K. Araki, T. Eno, and T. Hirano, Phys. Rev. A **69**, 063604 (2004).

[18] F. Gerbier, A. Widera, S. Fölling, O. Mandel, and I. Bloch, Phys. Rev. A **73**, 041602(R) (2006).

[19] S. R. Leslie, J. Guzman, M. Vengalattore, J. D. Sau, M. L. Cohen, and D. M. Stamper-Kurn, Phys. Rev. A **79**, 043631 (2009).

[20] W. Zhang, D. L. Zhou, M.-S. Chang, M. S. Chapman, and L. You, Phys. Rev. A **72**, 013602 (2005).

[21] Y. Kawaguchi, H. Saito, K. Kudo, and M. Ueda, Phys. Rev. A **82**, 043627 (2010).

[22] A. Lamacraft, Phys. Rev. A **83**, 033605 (2011).

[23] W. Zhang, S. Yi, and L. You, New J. Phys. **5**, 77 (2003).

APPENDIX E

SIMPLE AND EFFICIENT ALL-OPTICAL PRODUCTION OF SPINOR CONDENSATES

This appendix includes a reprint of Ref. (Jiang *et al.*, 2013): J. Jiang, L. Zhao, M. Webb, N. Jiang, H. Yang, and Y. Liu, Simple and efficient all-optical production of spinor condensates, Phys. Rev. A **88**, 033620 (2013).

PHYSICAL REVIEW A **88**, 033620 (2013)

Simple and efficient all-optical production of spinor condensates

J. Jiang,[1] L. Zhao,[1] M. Webb,[1] N. Jiang,[2] H. Yang,[2] and Y. Liu[1,*]
[1]*Department of Physics, Oklahoma State University, Stillwater, Oklahoma 74078, USA*
[2]*Center for Quantum Information, IIS, Tsinghua University, Beijing, China*

(Received 4 June 2013; revised manuscript received 13 August 2013; published 17 September 2013)

We present a simple and optimal experimental scheme for an all-optical production of a sodium spinor Bose-Einstein condensate (BEC). With this scheme, we demonstrate that the number of atoms in a pure BEC can be greatly boosted by a factor of 5 over some widely used schemes in a simple single-beam or crossed-beam optical trap. Our scheme avoids technical challenges associated with some all-optical BEC methods and may be applicable to other optically trappable atomic species. In addition, we discuss an upper limit for evaporative cooling efficiency in all-optical BEC approaches and a good agreement between our theoretical model and experimental data.

DOI: 10.1103/PhysRevA.88.033620 PACS number(s): 67.85.Hj, 64.70.fm, 37.10.Jk, 32.60.+i

I. INTRODUCTION

In the last two decades, many techniques have been developed to reliably generate a Bose-Einstein condensate (BEC) of more than 10^4 atoms. Almost every one of these techniques requires evaporative cooling in a trapping potential, including a magnetic trap, an optical dipole trap (ODT), or a combined magnetic and optical potential [1–5]. Among these techniques, all-optical methods have been proven to be versatile and popularly applied in producing quantum-degenerate gases of both bosonic [6–14] and fermionic [15] species. ODTs have tight confinement, which allows for fast evaporation with a duty cycle of a few seconds [6]. Unlike magnetic potentials that only trap atoms in the weak-field-seeking spin state, an ODT can confine all spin components. This is crucial for creating vector (spinor) BECs with a spin degree of freedom [16]. ODTs can also be applied to a wider variety of atomic species (e.g., ytterbium, alkaline-earth metals, and cesium) which cannot be feasibly condensed in a magnetic trap [8,13]. In addition, optical trapping does not require magnetic coils around trapped atoms, which not only provides better optical access but also reduces residual magnetic fields. The simplicity and versatility of ODTs widens the accessibility of BEC research on many-body physics, precision measurements, and quantum information science [17].

Forced evaporation in an ODT can be performed by simply reducing its trap depth U (e.g., lowering the trapping laser power). In this process, collision rates decrease with U, which leads to slow rethermalization and eventually stagnation in evaporative cooling. Several methods have been reported to overcome this difficulty, including tilting an ODT with a magnetic-field gradient [18], using a misaligned crossed ODT [12,14], compressing an ODT with a mobile lens [11], and applying multiple ODTs for staged evaporation [8,10]. In this paper, however, we show that these methods may not be necessary for some atomic species, in particular, sodium atoms. Good agreements between our model and experimental data enable us to develop an optimal ODT ramp and evaporation sequence for an all-optical production of sodium BECs. With this optimal scheme, we find that the number of atoms in a pure BEC is greatly boosted by a factor of 5 over some popular schemes and evaporation efficiency $\gamma = -d(\ln D)/d(\ln N)$ can be 3.5 in a crossed ODT. Here D is the phase space density, and N is the number of atoms. We also show an upper limit for γ at a given truncation parameter $\eta = U/k_B T$ and demonstrate that a constant η does not yield more efficient evaporative cooling. Here T is the atom temperature and k_B is the Boltzmann constant. This optimal experimental scheme allows us to avoid technical challenges associated with some all-optical BEC approaches.

II. EXPERIMENTAL SETUP

Our apparatus is divided by differential pumping tubes into an atomic oven chamber, an intermediate chamber, and a main chamber where a magneto-optical trap (MOT) is located [19], as shown in Fig. 1(a). Hot atoms are slowed down by a spin-flip Zeeman slower [21] and then collected in the MOT, which is constructed with six cooling beams and a pair of 24-turn anti-Helmholtz coils. Each MOT cooling beam is detuned by $\delta_{\text{cooling}} = -20$ MHz from the cycling transition, has a power of 6 mW, and combines with one 3.5-mW MOT repumping beam in a single-mode fiber. Every MOT repumping beam is detuned by $\delta_{\text{repump}} = -5$ MHz from the $|F = 1\rangle$ to $|F' = 2\rangle$ transition. After 8.5 s of MOT loading, a three-step polarization gradient cooling process efficiently cools 3×10^8 atoms to 40 μK [19]. To depump atoms into the $F = 1$ hyperfine states, the repumping beams are extinguished 1 ms before cooling beams and MOT coils are turned off. Figure 1(b) lists a typical experimental sequence for our all-optical BEC approach.

A crossed ODT consists of two far-detuned beams which originate from an IR laser with a maximum power of 13 W at 1064 nm and have a waist of 33 μm [22] at their intersection point, as shown in Fig. 1(a). A single-mode polarization-maintaining fiber is used to polish the beam mode and to minimize pointing fluctuations due to imperfections of the IR laser and thermal contractions of an acoustic-optical modulator. As a result, atoms which are transferred from the MOT into the tightly focused crossed ODT demonstrate a long lifetime of 8 s and a large collision rate. These are essential for all-optical BEC approaches.

A couple of ODT ramp sequences were proposed to improve the ODT capture efficiency by finding a reasonable balance between two competing ODT-induced effects [6,7,9,10,12–14,23,24]. First, a larger U enables more atoms to

---

[*] yingmei.liu@okstate.edu

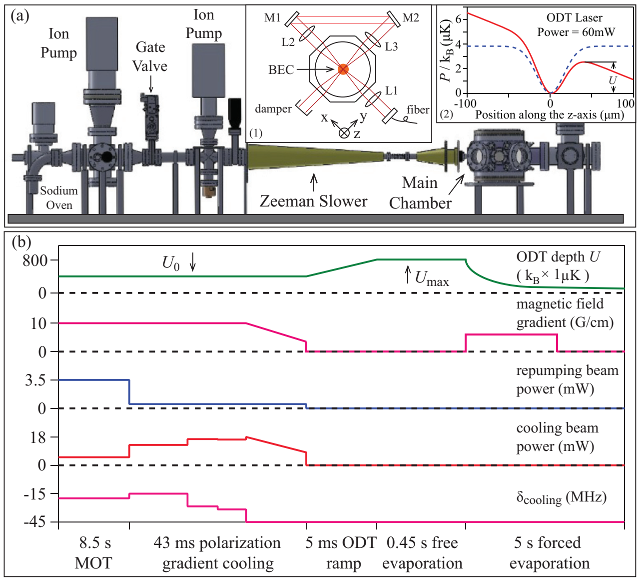

FIG. 1. (Color online) (a) Schematic of our apparatus. Inset 1: schematic of the crossed ODT setup around the main chamber. The positive z axis represents the direction of gravity. L_1, L_2, and L_3 are convex lenses. M_1 and M_2 are mirrors. Inset 2: the definition of the ODT trap depth U. The solid red line and dashed blue line represent the crossed ODT's trap potential energy P as a function of position along the z axis with and without taking into account the influence of gravity, respectively [20]. Here $x = y = 0$ and the ODT laser power is 60 mW. (b). Experimental sequence of creating sodium BECs with the all-optical approach (see text). Each MOT cooling beam is detuned by δ_{cooling} from the cycling transition. All axes are not to scale.

be captured in the ODT if the ODT beams do not interact with the MOT. The number of atoms loaded in the ODT is $N_{\text{rampA}} \sim \int_0^U \rho(\epsilon) f(\epsilon) d\epsilon$, where $\rho(\epsilon)$ and $f(\epsilon)$ are the density of states and occupation number at energy ϵ, respectively. This is confirmed by our data (blue triangles in Fig. 2) taken with scheme A, in which the ODT depth is linearly ramped in 5 ms from zero to U_0 immediately after MOT beams are switched off. On the other hand, there are some advantages to turning on intense ODT beams in the presence of MOT beams. For example, this allows the ODT to capture a larger number of cold and dense atoms by using MOT beams to prevent the gas from expanding. However, atoms experience non-negligible ac Stark shifts in regions where the ODT beams and the MOT overlap. As a result, the MOT's cooling capability is impaired in the MOT and ODT overlapping regions, and the number of atoms loaded into the ODT decreases when the ODT becomes too deep. N is thus not a monotonic function of U.

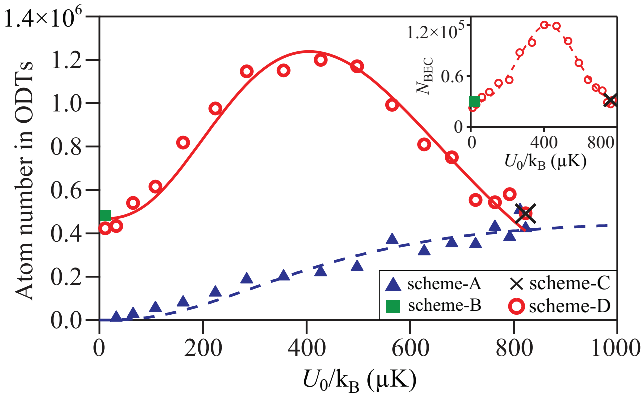

FIG. 2. (Color online) The number of atoms captured in the crossed ODT as a function of U_0 with the four ODT ramp sequences (see text). Our optimal scheme is the best scenario of scheme D when $U_0 \simeq U_{\max}/2$. The dashed blue line and the solid red line are fits based on N_{rampA} and N_{rampD}, respectively (see text). Inset: the number of atoms in a BEC as a function of U_0 when one of the three schemes (i.e., schemes B–D) and the same evaporation curve are applied. The dashed red line is a Gaussian fit to the data.

Scheme B (green squares in Fig. 2) is a popular scheme used to improve the ODT capture efficiency, in which ODT beams overlap with a MOT for a very short amount of time (20–200 ms) before the MOT beams are switched off [12,14,23,24]. Scheme C (black crosses in Fig. 2) is another widely applied scheme, which keeps the ODT beam at its maximum power during the entire MOT stage [6,9,10,13]. Figure 2 clearly shows that there is an optimal scheme which can increase the number of atoms loaded into the crossed ODT by a factor of 2.5 over the above two popular schemes. This optimal scheme is the best-case scenario for our scheme D. As shown in Fig. 1(b), the ODT in scheme D is kept at a small trap depth U_0 during the entire laser cooling process and is then linearly ramped to $U_{\max}$ in $t_{\text{ramp}} = 5$ ms. $U_{\max} \approx k_B \times 800\ \mu$K is the maximal trap depth used in this work, and $0 \leqslant U_0 \leqslant U_{\max}$. The number of atoms loaded into the ODT in scheme D may be expressed as $N_{\text{rampD}} \sim A\xi(U_0)\int_0^{U_0} \rho(\epsilon) f(\epsilon) d\epsilon + \int_{U_0}^{U_{\max}} \rho(\epsilon) f(\epsilon) d\epsilon$. Here $\xi(U_0) = \exp\{-[\delta_{\text{ODT}}(U_0)]^2/\omega_0^2\}$ is a correction factor due to the ODT-induced shift $\delta_{\text{ODT}}(U_0)$, while A and ω_0 are fitting parameters. Our data collected with scheme D (red circles in Fig. 2) can be well fitted by this model. The fit value of ω_0 is 1.2Γ, where $\Gamma/2\pi = 9.7$ MHz is the natural linewidth of sodium. The number of atoms in the ODT reaches its peak when the optimal ramp sequence with $U_0 \simeq U_{\max}/2$ is applied. Compared to the two popular schemes, the optimal scheme allows us to use ODT beams with smaller waists while loading the same amount of laser-cooled atoms to the ODT. The resulting high initial atom density and high collision rates from the optimal scheme enable very efficient evaporative cooling. This greatly boosts the number of atoms in a BEC by a factor of 5 over the two popular schemes for our apparatus, as shown in the inset in Fig. 2.

We find that our optimal scheme leads to a better ODT capture efficiency over the two popular schemes at every given frequency of the MOT beams within a wide range (i.e., -24 MHz $\leqslant \delta_{\text{cooling}} \leqslant -10$ MHz and -15 MHz $\leqslant \delta_{\text{repump}} \leqslant 6$ MHz). One mechanism may explain this phenomenon: well-aligned crossed ODT beams have a much larger intensity in the intersection region than that in the "wing" (nonintersecting) region. In other words, the light shift induced by the ODT beams is not uniform, i.e., a big shift in the intersection region and a small shift in the "wing" region. These ODT-induced nonuniform shifts cannot be mimicked by simply varying the frequencies of the MOT cooling and repumping beams. Because this mechanism does not depend on atomic species, our optimal scheme may thus be applicable to rubidium and other optical trappable atomic species.

III. EVAPORATIVE COOLING

To optimize γ, it is necessary to understand the time evolution of the system energy E and the atom number N during an evaporation process. Similar to Refs. [14,25–27], we use $\kappa k_B T \approx (\eta - 5)/(\eta - 4) k_B T$ to represent the average kinetic energy taken by an atom when it is removed from the ODT, and we assume the mean kinetic energy and mean potential energy to be $E/2$ when η is large. The time evolution of E and N is thus given by

$$\begin{aligned} \dot{E} &= -\frac{2(\eta - 4)e^{-\eta}N}{\tau_2}(U + \kappa k_B T) + \frac{\dot{U}}{U}\frac{E}{2} + \dot{E}|_{\text{loss}}, \\ \dot{N} &= -2(\eta - 4)e^{-\eta}N/\tau_2 + \dot{N}|_{\text{loss}}, \end{aligned} \tag{1}$$

where τ_2 is the time constant of the two-body elastic collision. In Eq. (1), $\dot{E}|_{\text{loss}}$ and $\dot{N}|_{\text{loss}}$ are due to various inelastic loss mechanisms and may be expressed as

$$\begin{aligned} \dot{E}|_{\text{loss}} &= k_s N - k_1 N(3k_B T) - k_3 n^2 N(2k_B T), \\ \dot{N}|_{\text{loss}} &= -k_1 N - k_3 n^2 N, \end{aligned} \tag{2}$$

where k_1 and k_3 are one-body and three-body loss rates, respectively. k_s represents heating introduced by ODT beams via a number of different mechanisms, such as pointing fluctuations of the ODT beams, a bad laser beam mode, and spontaneous light scattering. The term $2k_B T$ in Eq. (2) accounts for the fact that atoms in the ODT's center have higher density and thus are more affected by the three-body inelastic loss [12].

In our apparatus with the UHV pressure in the 10^{-12} Torr range, background collisions are negligible. Since the ODT beams are delivered via a single-mode polarization-maintaining fiber, heating induced by the ODT beams is minimized. k_1 and k_s are thus very small. If we ignore k_1 and k_s, Eq. (1) can be simplified to

$$\dot{E} = \dot{N}\eta_{\text{eff}} k_B T + \frac{\dot{U}}{U}\frac{E}{2}, \tag{3}$$

where $\eta_{\text{eff}} = \eta + \kappa - R(\eta + \kappa - 2)$. We define $R = (\dot{N}|_{\text{loss}})/\dot{N} = 1/[1 + 2(\eta - 4)e^{-\eta} R_{\text{gTb}}]$ to represent the portion of atom losses due to inelastic collisions, where R_{gTb} is the ratio of the inelastic collision time constant to τ_2. From solving the above equations, γ may be expressed as

$$\gamma = \eta_{\text{eff}} - 4 = \eta + \kappa - R(\eta + \kappa - 2) - 4. \tag{4}$$

The value of η in many publications on optical productions of BECs was held constant with $\Delta\eta = 0$ [6,7,11,12,14,15,18]. Our data in Fig. 3, however, show that a constant η does not lead to better evaporation or a larger γ. The values of γ in Fig. 3 are extracted from 36 evaporation processes in which the forced evaporation speed and the hold time at U_{max} are changed independently, although they all start with the same initial number of cold atoms in the crossed ODT. $\Delta\eta = \eta_{\text{f}} - \eta_{\text{i}}$ is the change of η during forced evaporation, where η_{i} and η_{f} are the values of η at U_{max} (i.e., the beginning of forced evaporation) and at U_{f}, respectively. In order to avoid overestimating γ due to the bosonic enhancement near the BEC transition temperature, we choose $U_{\text{f}} = k_B \times 30\mu\text{K}$, where no BEC appears. We find that $\Delta\eta$ tends to be a non-negative value when the forced evaporation time is longer than 1 s (solid black squares in Fig. 3), which is a good indication of sufficient rethermalization. We also find that γ is too small to yield a BEC when $\Delta\eta < -2.5$.

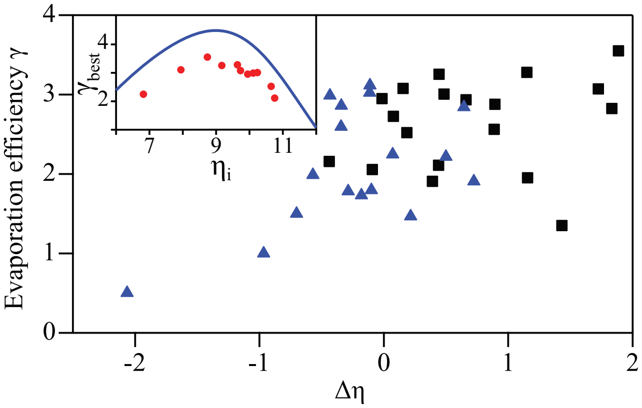

FIG. 3. (Color online) Evaporation efficiency γ in 36 different evaporation processes as a function of $\Delta\eta$. Solid black squares are data taken with the forced evaporation time longer than 1 s. Inset: γ_{best} as a function of η_{i} extracted from the main figure. The solid line sets an upper limit for γ based on Eq. (4) by assuming $k_1 = k_s = 0$ (see text).

We compare the evaporation efficiency at different values of η_{i}, as shown in the inset of Fig. 3. γ_{best} (the best achieved value of γ at a given η_i in our system) does not show a strong dependence on η_i if $8 < \eta_i < 10$, while γ_{best} sharply diminishes when η_i becomes too large or too small. In the inset of Fig. 3, a similar relationship between γ and η_i is also predicted by the solid blue line, which is a result based on Eq. (4) by ignoring k_1 and k_s and by applying a nonzero R (i.e., $R_{\text{gTb}} = 4000$ [4]). All of our data lie below the solid line in the inset, which may indicate that k_1 and k_s are larger than zero and cannot be ignored. Therefore, based on Fig. 3, we need to choose a value between 8 and 10 for η_i and keep $\Delta\eta$ larger than -0.5 in order to optimize evaporation efficiency γ.

The maximum achievable value for η_{i} appears to be 10.8, as shown in the inset of Fig. 3. To understand this, we monitor the time evolution of η and find that η has a maximal value η_{max} at a given ODT depth U. The value of η_{max} decreases exponentially with U, and η_{max} at U_{max} is 10.8, which agrees well with our theoretical prediction (solid red line in Fig. 4). Therefore, if one wishes to keep η unchanged during forced evaporation, η must be limited to 10.8 even though η_{max} can be much higher at low ODT depths (e.g., $\eta_{\text{max}} > 13$ for $U/k_B < 100\mu\text{K}$). This may be one reason why a constant η does not yield more efficient evaporative cooling. We also find that the time evolution of η at every U discussed in this paper can be well fitted with our model. Two typical fitting curves are shown in the inset of Fig. 4.

A pure $F = 1$ BEC of 1.2×10^5 sodium atoms at 50 nK is created from a 0.45-s free evaporation at U_{max} followed by a 5-s forced evaporation in which U is exponentially reduced. This evaporation curve provides two important parameters for efficient evaporative cooling: η_i is between 8 and 10, and the forced evaporation time is long enough for sufficient rethermalization but short enough to avoid excessive atom losses. Two time-of-flight absorption images in Fig. 5(a) show a typical change in the condensate fraction (CF) after

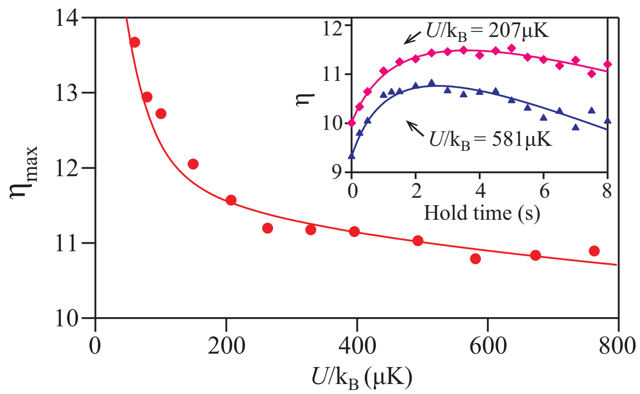

FIG. 4. (Color online) $\eta_{\max}$ as a function of the ODT depth U when atoms are held at a fixed U for 8 s. The solid line is a fit based on Eqs. (1) and (2) (see text). Inset: the time evolution of η at two typical ODT depths. Solid lines are fits based on the same model applied in the main figure (see text).

interrupting the evaporation curve at various U. We also apply the above all-optical approach to evaporate atoms in a single-beam ODT. A similar result can also be achieved in the single-beam ODT as long as its beam waist is smaller than 16 μm so that it can provide a high enough collision rate. The resulting number of condensed atoms in the single-beam ODT, however, is four times smaller than that in the crossed ODT.

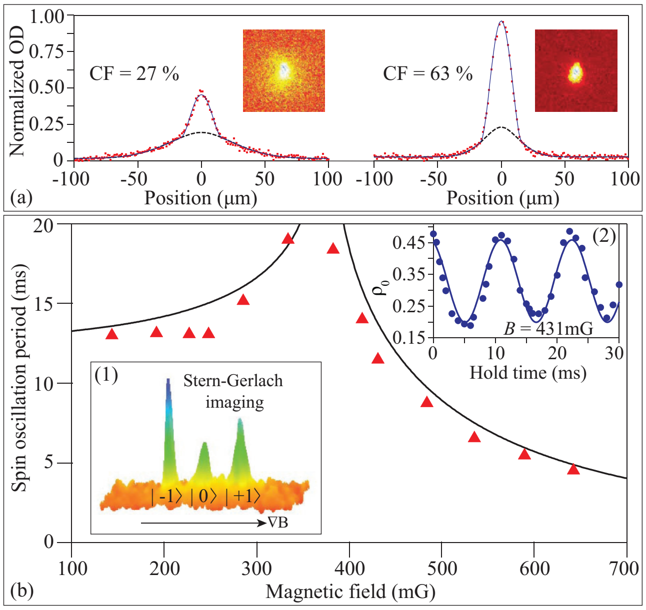

FIG. 5. (Color online) (a) Absorption images taken after interrupting an optimized evaporation curve at various U followed by a 10-ms time of flight (see text). OD stands for the optical density. Dashed black lines and solid blue lines are fits to the column densities based on a Gaussian distribution and a bimodal distribution, respectively. $\mathrm{CF} = \tilde{n}_c/(\tilde{n}_{th} + \tilde{n}_c)$, where $\tilde{n}_{th}$ and $\tilde{n}_c$ are column densities for the thermal cloud and the condensate, respectively. (b) The period of spin population oscillations as a function of B at $m = \rho_{+1} - \rho_{-1} = 0$. Here ρ_{m_F} is the fractional population of the m_F state. The solid black line is a fit based on the mean-field theory (see text). Inset 1: Three spin components of a $F = 1$ spinor BEC are spatially separated in a 3D Stern-Gerlach absorption image. Inset 2: A typical time evolution of ρ_0 at $B = 431$ mG and $m = 0$ when the spinor BEC is held in the crossed ODT. The solid blue line is a sinusoidal fit to the data.

To fully polarize atoms in a $F = 1$ BEC to the $|F = 1, m_F = 1\rangle$ state, a weak-magnetic-field gradient is applied during forced evaporation, as shown in Fig. 1(b). We then ramp up a magnetic bias field with its strength B between 100 and 700 mG while turning off the field gradient. We can prepare an initial state with any desired combination of three m_F states by altering the amplitude and duration of a resonant rf pulse and/or a resonant microwave pulse. A Stern-Gerlach separation followed by absorption imaging is used to measure the populations of different spin states, as shown in inset 1 in Fig. 5(b).

The interesting interactions in spinor BECs are interconversion among multiple spin states and magnetic-field interactions characterized by the quadratic Zeeman effect. Such a system can be described with a simple two-dimensional phase space that we can manipulate to some degree by changing the magnetic-field strength or the density of the BEC [17,28]. When a $F = 1$ spinor BEC is taken out of equilibrium at a nonzero magnetic field, spin population oscillations can be observed, as shown in inset (2) in Fig. 5(b). The population oscillations are nearly harmonic except near $B = 370$ mG, a separatrix in phase space where the period diverges. The data can be well fitted by a prediction from the mean-field theory [solid line in Fig. 5(b)] [17] with only one fitting parameter (i.e., the mean BEC density). Figure 5(b) may thus be a good way to measure the mean BEC density and to check the values of the crossed ODT's trap frequency and trap depth [22].

IV. CONCLUSION

In conclusion, we have presented an optimal experimental scheme for an all-optical production of sodium spinor BECs. For our apparatus, we have found that the number of atoms in a pure BEC with this scheme is greatly boosted by a factor of 5 over two popular schemes in a crossed ODT. Our scheme avoids technical challenges associated with some all-optical BEC approaches and may be applicable to other optically trappable atomic species and molecules [29]. We have showed an upper limit for γ at a given η, demonstrated that a constant η could not yield a larger γ, and discussed good agreements between our model and experimental data. We may be able to further improve evaporation efficiency to reach its upper limit and thus to increase the number of atoms in a BEC by combining our scheme with one of the clever ideas shown in [8,12,14,18].

ACKNOWLEDGMENTS

We thank the Army Research Office, Oklahoma Center for the Advancement of Science and Technology, and Oak Ridge Associated Universities for financial support. M.W. thanks the Niblack Research Scholar program. N.J. and H.Y. thank the National Basic Research Program of China.

[1] K. B. Davis, M.-O. Mewes, M. R. Andrews, N. J. van Druten, D. S. Durfee, D. M. Kurn, and W. Ketterle, Phys. Rev. Lett. **75**, 3969 (1995).

[2] M. H. Anderson, J. R. Ensher, M. R. Matthews, C. E. Wieman, and E. A. Cornell, Science **269**, 198 (1995).

[3] C. C. Bradley, C. A. Sackett, J. J. Tollett, and R. G. Hulet, Phys. Rev. Lett. **75**, 1687 (1995).

[4] W. Ketterle and N. J. van Druten, Adv. At. Mol. Opt. Phys. **37**, 181 (1996).

[5] Y.-J. Lin, A. R. Perry, R. L. Compton, I. B. Spielman, and J. V. Porto, Phys. Rev. A **79**, 063631 (2009).

[6] M. D. Barrett, J. A. Sauer, and M. S. Chapman, Phys. Rev. Lett. **87**, 010404 (2001).

[7] R. Dumke, M. Johanning, E. Gomez, J. D. Weinstein, K. M. Jones, and P. D. Lett, New J. Phys. **8**, 64 (2006).

[8] T. Weber, J. Herbig, M. Mark, H.-C. Nägerl, and R. Grimm, Science **299**, 232 (2003).

[9] C. S. Adams, H. J. Lee, N. Davidson, M. Kasevich, and S. Chu, Phys. Rev. Lett. **74**, 3577 (1995).

[10] K. J. Arnold and M. D. Barrett, Opt. Commun. **284**, 3288 (2011).

[11] T. Kinoshita, T. Wenger, and D. S. Weiss, Phys. Rev. A **71**, 011602 (2005).

[12] J.-F. Clément, J.-P. Brantut, M. Robert-de-Saint-Vincent, R. A. Nyman, A. Aspect, T. Bourdel, and P. Bouyer, Phys. Rev. A **79**, 061406 (2009).

[13] Y. Takasu, K. Maki, K. Komori, T. Takano, K. Honda, M. Kumakura, T. Yabuzaki, and Y. Takahashi, Phys. Rev. Lett. **91**, 040404 (2003).

[14] A. J. Olson, R. J. Niffenegger, and Y. P. Chen, Phys. Rev. A **87**, 053613 (2013).

[15] S. R. Granade, M. E. Gehm, K. M. O'Hara, and J. E. Thomas, Phys. Rev. Lett. **88**, 120405 (2002).

[16] J. Stenger, S. Inouye, D. M. Stamper-Kurn, H.-J. Miesner, A. P. Chikkatur, and W. Ketterle, Nature (London) **396**, 345 (1998).

[17] D. M. Stamper-Kurn and M. Ueda, Rev. Mod. Phys. **85**, 1191 (2013).

[18] C.-L. Hung, X. Zhang, N. Gemelke, and C. Chin, Phys. Rev. A **78**, 011604 (2008).

[19] The intermediate chamber allows us to refill alkali metals and get UHV pressures back to the 10^{-12} Torr range within 24 h. The first polarization gradient cooling step compresses the MOT for 20 ms by increasing the power of each cooling beam to 12 mW while changing δ_{cooling} to -15 MHz. In this step, the power of each MOT repumping beam is also drastically reduced to 45 μW. Then during a 5-ms premolasses step, every cooling beam is further red detuned in addition to its power being increased to 16 mW. This is followed by a 18-ms optical molasses, in which a cooling beam is detuned to $\delta_{\text{cooling}} = -45$ MHz and its power linearly drops to 8 mW. The magnetic-field gradient is also reduced to 3 G/cm over the 18 ms.

[20] The crossed ODT trap potential energy is $P = P_1 + P_2 + P_g$, where P_1 and P_2 are trap potentials of the two single-beam ODTs and P_g is due to the influence of gravity.

[21] L. Zhao, J. Jiang, J. Austin, M. Webb, Y. Pu, and Y. Liu (unpublished).

[22] We determined the value of the ODT's beam waist by measuring its trap frequency with two methods. First, we recorded the number of atoms in the ODT after sinusoidally modulating U at various modulation frequencies f_{m}. The number of atoms exhibits parametric resonances at $f_{\text{m}} = l f_{\text{ODT}}$, where f_{ODT} is the ODT's radial frequency and l is a positive integer number. In the second method, we kicked atoms in the single-beam ODT with a magnetic-field gradient and then recorded the position of atoms after holding the atoms in the ODT for a variable length of time. It appeared that atoms experienced a harmonic oscillation with a frequency equal to the ODT's axial frequency. We ensured the two ODT beams were well intersected at their focal points with high-resolution imaging in three orthogonal directions. The values of the ODT's beam waist and its trap depth provided by these two methods are very close to each other and also agree with those derived from Fig. 5(b). In this paper, the uncertainty of η is found to be $\sim 4\%$ based on the measurements with the above three methods.

[23] S. J. M. Kuppens, K. L. Corwin, K. W. Miller, T. E. Chupp, and C. E. Wieman, Phys. Rev. A **62**, 013406 (2000).

[24] T. Takekoshi and R. J. Knize, Opt. Lett. **21**, 77 (1996).

[25] K. M. O'Hara, M. E. Gehm, S. R. Granade, and J. E. Thomas, Phys. Rev. A **64**, 051403 (2001).

[26] O. J. Luiten, M. W. Reynolds, and J. T. M. Walraven, Phys. Rev. A **53**, 381 (1996).

[27] M. Yan, R. Chakraborty, A. Mazurenko, P. G. Mickelson, Y. N. Martinez de Escobar, B. J. DeSalvo, and T. C. Killian, Phys. Rev. A **83**, 032705 (2011).

[28] Y. Liu, S. Jung, S. E. Maxwell, L. D. Turner, E. Tiesinga, and P. D. Lett, Phys. Rev. Lett. **102**, 125301 (2009).

[29] Upon completion of this work, we recently become aware of Ref. [30] and its ODT ramp sequence, which linearly ramps ODTs from $U_{\max}/3$ to $U_{\max}$ in $t_{\text{ramp}} = 2$ s. We find that the number of atoms in a pure BEC exponentially decreases with t_{ramp} when $t_{\text{ramp}} > 0.01$ s in our system. The optimal sequence explained in our paper yields a pure BEC of at least twice the number of atoms as that from a sequence with $t_{\text{ramp}} = 2$ s for our apparatus.

[30] D. Jacob, E. Mimoun, L. D. Sarlo, M. Weitz, J. Dalibard, and F. Gerbier, New J. Phys. **13**, 065022 (2011).

VITA

LICHAO ZHAO

Candidate for the Degree of

Doctor of Philosophy

Thesis: ANTIFERROMAGNETIC SPINOR CONDENSATES IN MICROWAVE DRESSING FIELDS AND OPTICAL LATTICES

Major Field: Physics

Biographical:

Education:

Completed the requirements for the Doctor of Philosophy in physics at Oklahoma State University, Stillwater, Oklahoma in December, 2015.

Completed the requirements for the Bachelor of Science in physics at University of Science and Technology of China, Hefei, China in 2006.

Professional Memberships:

American Physical Society